



저작자표시-비영리-변경금지 2.0 대한민국

이용자는 아래의 조건을 따르는 경우에 한하여 자유롭게

- 이 저작물을 복제, 배포, 전송, 전시, 공연 및 방송할 수 있습니다.

다음과 같은 조건을 따라야 합니다:



저작자표시. 귀하는 원저작자를 표시하여야 합니다.



비영리. 귀하는 이 저작물을 영리 목적으로 이용할 수 없습니다.



변경금지. 귀하는 이 저작물을 개작, 변형 또는 가공할 수 없습니다.

- 귀하는, 이 저작물의 재이용이나 배포의 경우, 이 저작물에 적용된 이용허락조건을 명확하게 나타내어야 합니다.
- 저작권자로부터 별도의 허가를 받으면 이러한 조건들은 적용되지 않습니다.

저작권법에 따른 이용자의 권리는 위의 내용에 의하여 영향을 받지 않습니다.

이것은 [이용허락규약\(Legal Code\)](#)을 이해하기 쉽게 요약한 것입니다.

[Disclaimer](#)

공학박사 학위논문

**A Numerical Study on Berthing
Problem between Two Floating
Bodies in Waves**

수치해석을 이용한 두 부유체의 파랑 중
접안문제에 관한 연구

2015년 2월

서울대학교 대학원

조선해양공학과

남 보 우

Abstract

**A Numerical Study on Berthing
Problem between Two Floating
Bodies in Waves**

Bo Woo Nam

Department of Naval Architecture and Ocean Engineering
Seoul National University

This thesis considers the berthing problem between two floating bodies in waves. A numerical method is developed for solving the berthing problem in the time domain based on the potential flow. The wave-induced motion and force responses during the berthing process are investigated by the developed method.

Berthing involves a moving vessel closely approaching a fixed or moored offshore structure from a far distance. The theoretical formulation for the berthing problem is suggested with respect to the earth-fixed coordinate system because the relative positions of the two vessels continuously change. The linearized boundary value problems are derived by applying perturbation series expansion method. Acceleration potential method is introduced to evaluate the hydrodynamic forces that act on the bodies during berthing.

The finite element method is used to solve the Laplace equation in the fluid domain with appropriate boundary conditions. The weak formulation of the governing equation is obtained by introducing the test functions and applying integration by parts. The fluid domain is discretized using a finite number of elements, and the linearized free-surface boundary conditions are integrated in time by applying 4th-order Adams-Bashforth-Moulton method. To satisfy the

radiation conditions numerically, damping zone technique is utilized. A new re-mesh algorithm is developed for efficient updating of the mesh considering the horizontal movement of the vessel. The concept of local and global meshing is employed in the algorithm, and the re-mesh process is replaced by a simple connection operation.

The developed numerical method is used to investigate the berthing problem, with particular consideration of two benchmark berthing problems. The first is berthing between two rectangular barges, which are assumed to comprise a transportation barge and an installation barge. Under various regular wave conditions, a series of berthing simulations are conducted by the developed numerical method, with focus on the hydrodynamic forces that act on the barges during the berthing process. The effects of the wave frequency and heading on the hydrodynamic force are discussed in this thesis. To validate present numerical results, model tests were conducted in the Ocean Engineering Basin of KRISO. The berthing tests were performed using two barge models under the head and beam sea conditions. Fairly good agreement is observed between the numerical simulation and experimental results. The effects of the barge size and berthing path are also briefly discussed based on the numerical results.

The second berthing problem considered in this study is that between a floating production, storage, and offloading (FPSO) unit and a shuttle tanker. The focus in this case is on the wave-induced motion response during the berthing process. The characteristics of the wave-induced motion response in a head sea are examined with various wave frequencies and berthing speeds. The proposed numerical method is also used to investigate the berthing process in quartering and beam seas, with particular interest in the sheltering effect and the strong modulation of the motion response. This thesis further discusses the berthing problem in irregular seas as well as the effects of the wave period, height, and random seed on the motion response.

Keywords: Berthing, Floating body, Hydrodynamic force, Wave-induced motion, finite element method
Student Number: 2006-30808

Contents

Chapter 1. Introduction	1
1.1 Berthing problem	1
1.2 State of the art	4
1.3 Objective & Work scope	11
1.4 Outline of the thesis	12
Chapter 2. Theoretical Formulation.....	14
2.1 Exact boundary value problem	14
2.2 Linearized boundary value problem	16
2.3 Hydrodynamic Force	20
Chapter 3. Numerical Method	23
3.1 Finite element method	23
3.2 Free-surface integration	24
3.3 Algorithm for mesh generation	25
3.4 Solution Procedure.....	29
3.4 Validation of the numerical method.....	32
Chapter 4. Berthing Problem between Two Barges.....	38
4.1 Problem definition	38
4.2 Wave field and force response in berthing.....	41
4.3 Effect of wave frequency	47
4.4 Effect of wave heading	60
4.5 Comparison with experiments	72
4.5 Effect of barge size	82
4.6 Effect of berthing path	88

Chapter 5. Berthing Problem between FPSO and Shuttle Tanker	92
5.1 Problem definition	92
5.2 Berthing in regular wave (I): Head sea	95
5.3 Berthing in regular wave (2): Quartering and beam sea	122
5.4 Berthing in irregular wave	136
Chapter 6. Conclusions	150
Appendix A. Gap resonance between two barges	153
Appendix B. Gap resonance between FPSO and shuttle tanker	161
Appendix C. Sheltering zone in regular waves	164
Bibliography	165
Abstract	171

List of Tables

Table 1.1 Recent papers for multiple floating body problems.....	5
Table 1.2 Recent papers for numerical study on berthing problem ..	7
Table 1.3 Papers about finite element method for floating body problem	10
Table 3.1 Summary of numerical method.....	31
Table 4.1 Dimensions of the transportation barge	40
Table 5.1 Principle dimensions of FPSO and shuttle tanker.....	94

List of Figures

Fig. 2.1 Coordinate system for the berthing problem	14
Fig. 2.2 Exact boundary value problem for the berthing problem between two floating bodies	16
Fig. 2.3 First-order boundary value problem for the berthing problem between two floating bodies	17
Fig. 3.1 Local and global mesh for single floating body	27
Fig. 3.2 Connection operation for merging meshes	28
Fig. 3.3 Mesh generation algorithm for two floating bodies	28
Fig. 3.4 Schematic diagram for solution interpolation	29
Fig. 3.5 Flow chart for the present solution procedure	30
Fig. 4.1 Schematic diagram for berthing problem between two barges	38
Fig. 4.2 Dimensions for floating crane installation vessel in operation	39

Fig. 4.3 Wave fields around the barges during the berthing operation (Heading 180°, $\lambda/L=1.667$, $H=1.0$ m, $V=2.0$ kts).....	43
Fig. 4.4 First-order wave forces acting on the barges during the berthing operation (Heading 180°, $\lambda/L=1.667$, $H=1.0$ m, $V=2.0$ kts).....	44
Fig. 4.5 Second-order wave forces acting on the barges during the berthing operation (Heading 180°, $\lambda/L=1.667$, $H=1.0$ m, $V=2.0$ kts).....	46
Fig. 4.6 Wave fields around the barges during the berthing operation under various wave frequencies (Heading 180°, $H=1.0$ m, $V=2.0$ knots)	49
Fig. 4.7 Gap resonant frequency based on the side-by-side calculations by higher-order boundary element method in frequency domain.....	50
Fig. 4.8 First-order sway wave excitation forces acting on the transportation barge during the berthing operation under various regular wave conditions (Heading 180°, $H=1.0$ m, $V=2.0$ kts)	51
Fig. 4.9 First-order heave wave excitation forces acting on the transportation barge during the berthing operation under various regular wave conditions (Heading 180°, $H=1.0$ m, $V=2.0$ kts)	52
Fig. 4.10 Amplitude contours of first-order wave excitation forces acting on the transportation barge during the berthing operation (Heading 180°, $H=1.0$ m, $V=2.0$ kts).....	54
Fig. 4.11 Amplitude contours of first-order wave excitation moments acting on the transportation barge during the berthing operation (Heading 180°, $H=1.0$ m, $V=2.0$ kts).....	55
Fig. 4.12 Second-order surge wave forces acting on the transportation barge during the berthing operation under various	

regular wave conditions (Heading 180°, H=1.0m, V=2.0 knots) ...	57
Fig. 4.13 Second-order sway wave forces acting on the transportation barge during the berthing operation under various regular wave conditions (Heading 180°, H=1.0m, V=2.0 knots) ...	58
Fig. 4.14 Second-order drift force contours of the transportation barge during the berthing operation under various regular wave conditions (Heading 180°, H=1.0m, V=2.0 knots).....	59
Fig. 4.15 Wave fields around the barges during the berthing operation in beam sea (Heading 90°, $\lambda/L=1.0$, H=1.0 m, V=2.0 kts)	61
Fig. 4.16 Wave fields around the barges during the berthing operation in beam sea (Heading 270°, $\lambda/L=1.0$, H=1.0 m, V=2.0 kts)	62
Fig. 4.17 Comparison of first-order wave excitation forces acting on the barges in beam sea ($\lambda/L=1.0$, H=1.0 m, V=2.0 kts).....	63
Fig. 4.18 Shielding zone around single barge in beam sea based on the frequency-domain solutions (Heading 90°).....	64
Fig. 4.19 Encounter frequencies of the transportation barge in beam sea (Heading 270°, $\lambda/L=1.0$, H=1.0 m, V=2.0 knots).....	66
Fig. 4.20 FFT results of sway wave excitation force acting on the transportation barge (Heading 270°, H=1.0 m, V=2.0 knots).....	66
Fig. 4.21 Comparison of second-order sway wave excitation forces acting on the barges in beam sea ($\lambda/L=1.0$, H=1.0m, V=2.0 knots)	67
Fig. 4.22 Wave fields around the barges during the berthing operation in quartering sea (Heading 135°, $\lambda/L=1.0$, H=1.0 m, V=2.0 kts)	68
Fig. 4.23 Wave fields around the barges during the berthing	

operation in quartering sea (Heading 225°, $\lambda/L=1.0$, $H=1.0$ m, $V=2.0$ kts)	69
Fig. 4.24 Comparison of the first-order wave excitation forces acting on the barges in quartering sea ($\lambda/L=1.0$, $H=1.0$ m, $V=2.0$ kts)	70
Fig. 4.25 Second-order sway forces acting on the transportation barge during the berthing operation in quartering sea ($\lambda/L=1.0$, $H=1.0$ m, $V=2.0$ kts)	71
Fig. 4.26 Model test set-up for berthing experiment between two barges	72
Fig. 4.27 Snapshots of berthing model test in regular waves (Heading 180 °, $\lambda/L=1.667$, $H=1.0$ m, $V=2.0$ kts).....	74
Fig. 4.28 Snapshots of gap flow during berthing model test in head sea ($\lambda/L=1.667$, $H=1.0$ m, $V=2.0$ kts).....	75
Fig. 4.29 Comparison of sway wave forces acting on the transportation barge during the berthing model test in head sea ($H=1.0$ m, $V=2.0$ kts).....	76
Fig. 4.30 Comparison of yawing moments acting on the transportation barge during the berthing model test in head sea ($H=1.0$ m, $V=2.0$ kts).....	77
Fig. 4.31 Snapshots of berthing model test in regular waves (Heading 90 °, $\lambda/L=1.667$, $H=1.0$ m, $V=2.0$ kts).....	78
Fig. 4.32 Snapshots of gap flow during berthing model test in beam sea ($\lambda/L=1.667$, $H=1.0$ m, $V=2.0$ kts).....	79
Fig. 4.33 Comparison of sway wave forces acting on the transportation barge between experiments and calculations in beam	

sea ($H=1.0$ m, $V=2.0$ kts).....	80
Fig. 4.34 Wave fields during the berthing operation with various barge dimensions in head sea ($\lambda/L=1.667$, $H=1.0$ m, $V=2.0$ kts) ...	83
Fig. 4.35 First-order sway wave excitation forces acting on the barges during the berthing operation with various barge dimensions in head sea ($\lambda/L=1.667$, $H=1.0$ m, $V=2.0$ kts).....	84
Fig. 4.36 Second-order sway wave forces acting on the barges during the berthing operation with various barge dimensions in head sea ($\lambda/L=1.667$, $H=1.0$ m, $V=2.0$ kts)	85
Fig. 4.37 Comparison of sway maximum wave excitation force acting on the transportation barge during the berthing operation with various barge dimensions ($H=1.0$ m, $V=2.0$ kts).....	86
Fig. 4.38 Wave field around the barges during the berthing operation with various berthing paths (Heading 135° , $H=1.0$ m, $V=2.0$ kts)	89
Fig. 4.39 Sway excitation forces acting on the transportation barge during the berthing operation with various berthing paths (Heading 135° , $H=1.0$ m, $V=2.0$ kts).....	90
Fig. 4.40 Sway excitation forces acting on the transportation barge during the berthing operation with various berthing paths (Heading 135° , $H=1.0$ m, $V=2.0$ kts).....	91
Fig. 5.1 Berthing problem for FPSO and shuttle tanker	93
Fig. 5.2 Wave fields around the FPSO and shuttle tanker during the berthing operation in regular wave (Heading 180° , $\lambda=150$ m, $H=1.0$ m, $V=2.0$ kts)	97
Fig. 5.3 Motion responses of the FPSO during the berthing	

operation in regular wave (Heading 180°, $\lambda=150$ m, H=1.0 m, V=2.0 kts)	98
Fig. 5.4 Motion responses of the shuttle tanker during the berthing operation in regular wave (Heading 180°, $\lambda=150$ m, H=1.0 m, V=2.0 kts)	99
Fig. 5.5 Wave fields at roll amplification points during the berthing operation in regular wave (Heading 180°, $\lambda=150$ m, H=1.0 m, V=2.0 kts)	100
Fig. 5.6 Wave fields during the berthing operation under various regular wave conditions (Heading 180°, H=1.0 m, V=2.0 kts)	102
Fig. 5.7 Heave time series of the shuttle tanker during the berthing operation under various regular wave conditions (Heading 180°, V=2.0 kts)	103
Fig. 5.8 Roll time series of the shuttle tanker during the berthing operation under various regular wave conditions (Heading 180°, V=2.0 kts)	104
Fig. 5.9 Pitch time series of the shuttle tanker during the berthing operation under various regular wave conditions (Heading 180°, V=2.0 kts)	105
Fig. 5.10 Motion amplitude contours of the shuttle tanker during the berthing operation (Heading 180°, V=2.0 kts).....	107
Fig. 5.11 Second-order surge wave forces acting on the shuttle tanker under various regular wave conditions (Heading 180°, V=2.0 kts)	110
Fig. 5.12 Second-order sway wave forces acting on the shuttle tanker under various regular wave conditions (Heading 180°,	

V=2.0 kts)	111
Fig. 5.13 Wave drift force contours of the shuttle tanker under various regular wave conditions (Heading 180°, V=2.0 kts).....	112
Fig. 5.14 Heave time series of the shuttle tanker during the berthing operation with four different berthing speeds (Heading 180°, $\lambda=150$ m)	114
Fig. 5.15 Roll time series of the shuttle tanker during the berthing operation with four different berthing speeds (Heading 180°, $\lambda=150$ m)	115
Fig. 5.16 Heave amplitude contours of the shuttle tanker during the berthing operation with four different berthing speeds (Heading 180°)	116
Fig. 5.17 Roll amplitude contours of the shuttle tanker during the berthing operation with four different berthing speeds (Heading 180°)	117
Fig. 5.18 Second-order sway force acting on the shuttle tanker during the berthing operation with four berthing speeds (Heading 180°, $\lambda=150$ m)	118
Fig. 5.19 Sway drift force contours of the shuttle tanker during the berthing operation with four berthing speeds (Heading 180°)	119
Fig. 5.20 Comparison of dynamic and quasi-steady motion response (Heading 180°, $\lambda=100$ m)	120
Fig. 5.21 Comparison of dynamic and quasi-steady motion response (Heading 180°, $\lambda=150$ m)	121
Fig. 5.22 Wave fields during berthing between the FPSO and shuttle tanker in quartering sea ($\beta=225^\circ$, $\lambda=150$ m, $H=1.0$ m, $V=2.0$	

kts)	123
Fig. 5.23 Motion responses of the FPSO and shuttle tanker during the berthing operation in quartering sea ($\beta=225^\circ$, $\lambda=150$ m, $V=2.0$ kts)	124
Fig. 5.24 Sheltering zones around the FPSO w/o and w/ shuttle tanker in quartering sea based on frequency-domain solutions ($\beta=225^\circ$, $\lambda=150$ m)	125
Fig. 5.25 Motion amplitude contours of the shuttle tanker during berthing in quartering sea ($\beta=225^\circ$, $V=2.0$ kts)	126
Fig. 5.26 Wave fields around FPSO and shuttle tanker during the berthing operation ($\beta=135^\circ$, $\lambda=150$ m, $H=1.0$ m, $V=2.0$ kts)	127
Fig. 5.27 Motion time series of the FPSO and shuttle tanker during the berthing operation ($\beta=135^\circ$, $\lambda=150$ m, $H=1.0$ m, $V=2.0$ kts)	129
Fig. 5.28 Motion time series(left) and wave field(right) at heave amplification points during the berthing operation ($\beta=135^\circ$, $\lambda=150$ m, $H=1.0$ m, $V=2.0$ kts)	130
Fig. 5.29 Motion amplitude contours of the shuttle tanker during berthing in quartering sea ($\beta=135^\circ$, $V=2.0$ kts)	131
Fig. 5.30 Wave fields during the berthing operation in beam sea ($\beta=270^\circ$ (left) & 90° (right), $\lambda=150$ m, $H=1.0$ m, $V=2.0$ kts)	132
Fig. 5.31 Motion time series of the FPSO and shuttle tanker during the berthing operation ($\beta=270^\circ$ (left) & 90° (right), $\lambda=150$ m, $V=2.0$ kts)	133
Fig. 5.32 Sheltering zone around the FPSO w/o and w/ shuttle tanker in beam sea based on frequency-domain solutions ($\beta=270^\circ$,	

$\lambda=150\text{m}$).....	134
Fig. 5.33 Motion amplitude contours of the shuttle tanker during the berthing operation in beam sea ($\beta=270^\circ$ (left) & 90° (right), $V=2.0$ kts)	135
Fig. 5.34 Motion responses of the shuttle tanker during the berthing operation in irregular sea (Heading 180° , $V=2.0$ knots).....	137
Fig. 5.35 Wave field around FPSO and shuttle tanker during the berthing operation in irregular sea (Gap=104 m(left), Gap=50 m(right)).....	138
Fig. 5.36 Wave fields around FPSO and shuttle tanker during the berthing operation in irregular sea with different headings ($H_s=1.0$ m, $T_p=10.0$ s).....	140
Fig. 5.37 Heave time series of the shuttle tanker during the berthing operation in irregular sea with different headings ($H_s=1.0$ m, $T_p=10.0$ s).....	141
Fig. 5.38 Roll time series of the shuttle tanker during the berthing operation in irregular sea with different headings ($H_s=1.0$ m, $T_p=10.0$ s).....	142
Fig. 5.39 Wave fields around FPSO and shuttle tanker during the berthing operation with different random seed (Heading 180° , $H_s=1.0\text{m}$, $T_p=8.0$ s)	144
Fig. 5.40 Heave time series of the shuttle tanker during the berthing operation in irregular sea with different random seeds ($H_s=1.0\text{m}$, $T_p=8.0\text{m}$)	145
Fig. 5.41 Roll time series of the shuttle tanker during the berthing operation in irregular sea with different random seeds ($H_s=1.0\text{m}$,	

Tp=8.0m)	146
Fig. 5.42 Motion responses of the shuttle tanker during the berthing operation in irregular sea (Heading 180 deg., V=2.0 knots).....	148
Fig. 5.43 Maximum motion responses of the shuttle tanker during the berthing operation in irregular sea with different wave heights	149

Chapter 1. Introduction

1.1 Berthing problem

Berthing is a very common marine operation both in harbors and at open sea. It involves a moving vessel closely approaching a fixed or moored offshore structure from a far distance. During berthing, the distance between the stationary structure and berthing vessel decreases continuously, resulting in increasing hydrodynamic interaction. At certain distances and frequencies, the gap resonant wave between the two vessels produces strong repulsive forces, and this makes the berthing operation more difficult. Sometimes, the berthing vessel is assisted by tugs or dynamic positioning system (DPS). In the former case, the tugs control both the berthing speed and vessel heading in the push and pull mode (Buchner *et al.*, 2005). The berthing speed is thus limited by the capacity of the assistive system. As the berthing vessel gets close to the pier or moored structure, the speed should be reduced to avoid a “collision” course (Wilde *et al.*, 2009).

Berthing can be categorized into three types. The first type is berthing in harbors, in which a ship approaches a pier. The second type is berthing between two moving ships. This is occasionally referred to as “lightering operation” because one ship is made lighter by transferring its cargo to another ship. During a lightering operation, both ships usually have forward speed. The third type is berthing to a moored offshore structure (or vessel) on the open sea. In the case of berthing on the open sea, the wave loads and

motion responses are significant factors, unlike in berthing in a harbor.

In harbors, many kinds of ships berth to a pier for different purposes. For example, container ships berth to a pier to load or unload cargo, whereas ferries do so for passengers to embark or disembark. In the harbor, the pilot selects the appropriate berthing path, and in special cases, ferries may berth using twin skegs and rudders. The motion during this operation is sometimes called as “crabbing motion.”

Lightering operation involves the transfer of cargo, in particular oil or liquefied gases, from a large vessel to a smaller vessel which can deliver the cargo ashore. The operation takes place with the ship to be lightered (STBL) and the service ship advancing. Typically, STBL is a VLCC of about 300, 000 DWT and the service ship is an Aframax type tanker of about 100,000 DWT. The service ship initially sails abreast of the STBL with approximately the same heading and forward speed at a lateral distance of about 200m from the STBL. Then, the ship makes a slow lateral approach towards the STBL with a minimal difference in heading. (Lataire *et al.*, 2012)

Berthing at offshore installations is of the third type. For example, a transportation barge may approach a crane vessel to deliver heavy loads or subsea equipment. In this case, the crane vessel is temporarily moored at the installation site. Since the lifting operation is usually performed on the portside or around the stern area of the crane vessel, the berthing path of the transportation barge should be selected accordingly. During the berthing operation, the two vessels may be exposed to various environmental conditions including waves, wind, and currents. Waves from different

headings particularly induce motion response of the vessels, and this may limit the operability of the berthing process. Additional thrust power would be required owing to the wave drift forces acting on the transportation barge. It is well-known that strong repulsive force act on the two vessels in side-by-side configuration. The captain of the transportation barge should be careful to take the wave headings into consideration in selecting the berthing path because the hydrodynamic force is significantly affected by the berthing path. After completion of the berthing operation, a fender or mooring line can be used to fasten the transportation barge and crane vessel together. Float-over installation also requires berthing to an offshore installation. In this case, both the berthing and de-berthing operations between the offshore structure and the transportation barge are essential to the success of the mating process.

With the rapid progress of offshore technology in recent years, new floating offshore structure such as floating production, storage, and offloading (FPSO) units; floating, storage, and regasification units (FSRUs); and floating liquefied natural gas (FLNG) platforms have been proposed for oil and gas exploration and exploitation. Generally, these structures are maintained stationary by a spread or turret mooring system. Some use a DPS to control the heading of the structure. A shuttle tanker or liquefied natural gas carrier (LNGC) periodically approaches the offshore structure to load oil or gas, and the berthing path of the vessel would depend on the type of loading operation. For side-by-side loading, the berthing vessel approaches the offshore structure along a side path, whereas the berthing path is toward the rear or front of the structure in tandem loading.

1.2 State of the art

1.2.1 Multiple floating body problem

The multiple floating body problem has received lots of attentions in recent times. A typical example of the problem is a transfer operation between an FPSO unit or an FSRU and a shuttle tanker in side-by-side or tandem configuration. The connection of a tender vessel to a tension leg platform (TLP) is another example of a multiple floating body problem. In the study of ship motion, the problem of ship-to-ship interaction still remains a very attractive topic.

Several experimental studies have been conducted on the multiple floating body problem. For example, Buchner *et al.* (2001) conducted model tests on an LNG FPSO unit and a shuttle tanker in a side-by-side configuration. Hong *et al.* (2002) also carried out a series of model tests on an LNG FPSO unit and a shuttle tanker in single, side-by-side, and tandem configurations. They focused on the coupled effect of the motion response of the vessels and the repulsive wave drift forces. Hong *et al.* (2005) investigated three-body problems of FPSO, LNGC, and Shuttle tanker by model tests. They discussed the characteristics of wave-induced motion response and wave drift force in three-body problems. Kashiwagi *et al.* (2005) measured wave forces acting on the restrained barge and wigley models in side-by-side configuration, and provided the wave excitation and mean drift force data for numerical code validation. Recently, Cho *et al.* (2011) performed complex model tests on the side-by-side two body problem including sloshing effect.

Table 1.1 Recent papers for multiple floating body problems

Year	Author	Configuration	Model	Experiment	Calculation
2001	Buchner <i>et al.</i>	Side-by-side	FPSO & Shuttle tanker	O	Freq. & Time
2001	Huijsmans <i>et al.</i>	Side-by-Side	FPSO & Shuttle tanker	X	Freq.
2002	Hong <i>et al.</i>	Side-by-side Tandem	FPSO & Shuttle tanker	O	Freq.
2003	Kim <i>et al.</i>	Side-by-side	FPSO & LNGC	X	Freq.
2003	Inoue & Ali	Side-by-side Tandem	Two Vertical Cylinder FPSO & Shuttle tanker	X	Freq.
2005	Hong <i>et al.</i>	Side-by-side	LNG FPSO, LNGC, Shuttle tanker(3bodies)	O	Freq.
2005	Kashiwagi <i>et al.</i>	Side-by-side	Barge & wigley	O	Freq.
2005	Ye <i>et al.</i>	Side-by-side	FSRU & LNGC	X	Freq. & Time
2005	Koo & Kim	Side-by-side	FPSO & LNGC	X	Freq. & Time
2006	Fournier <i>et al.</i>	Side-by-side	FSRU & LNGC	O	Freq.
2006	Teigen&Nizwecki	Side-by-side	FPSO & Shuttle tanker	X	Freq.
2007	Naciri <i>et al.</i>	Side-by-side	FSRU & LNGC	O	Time
2009	Hansen <i>et al.</i>	Side-by-side	Two LNG tanker	O	Time
2011	Cho <i>et al.</i>	Side-by-side	FSRU & LNGC	O (sloshing)	X
2012	Kim <i>et al.</i>	Side-by-side	FLNG & LNGC	O	X
2012	Zhang <i>et al.</i>	Side-by-side	FPSO, Tanker, Buoy	X	Time
2012	Kim <i>et al.</i>	Side-by-side	FLNG & LNGC	O	Freq.
2013	Park <i>et al.</i>	Side-by-side	FLNG & LNGC	X	Freq. & Time (Sloshing)

Numerical methods for solving the multiple floating body problem have been proposed by several researchers. To name a few, Huijima *et al.*(2001) proposed the “lid approach” for a side-by-side two-body problem, noting that

it can be used to relax the gap flow and correct the unrealistic drift force. Hong *et al.* (2002) applied higher-order boundary element method (HOBEM) to solve the side-by-side and tandem two-body problems in the frequency domain. They observed that potential flow calculations overestimate the wave drift force owing to the gap resonance that occurs for a gap of 4 m. Ye *et al.* (2005) and Koo & Kim (2005) presented time-domain simulations of an FPSO unit and a shuttle tanker for mooring analysis. Park *et al.* (2013) used a numerical method to investigate the side-by-side problem, and particularly used computational fluid dynamics (CFD) to examine the sloshing effect. Some recent works on the multiple floating body problem with the employed models and research methodologies are given in Table 1.1.

1.2.2 Berthing problem

Recent numerical studies on the berthing problem can be divided into two groups. The first group comprises works that focused on the development of practical numerical simulation tools. Such studies solved the equation of motion of the floating bodies, with most of them using maneuvering or seakeeping equations. For example, Yoo (2000) showed numerical simulation of berthing operation of a twin-screw ferry based on maneuvering equation. Doorn and Hove (2002) investigated berthing problem between FPSO and tanker using fast-time simulation method based on maneuvering equation. Meanwhile, Sakakibara *et al.* (2005) developed a simulation program for lightering operation between two ships using seakeeping equation based on

impulse response function. Sasa *et al* (2010) also applied seakeeping model to solve the berthing problem between a ship and pontoon. Recently, Wilde *et al.*(2009) and Skejic & Berg (2010) used both seakeeping and maneuvering equation for berthing problem. Wilde *et al.*(2009) presented a direct time-domain downtime assessment system for LNG transfer operations. They performed downtime analysis of berthing and transfer operations between an FSRU and LNGC on waves. Skejic & Berg(2010) showed numerical simulations of lightering operation based on seakeeping and maneuvering equation. Table 1.2 shows the recent papers for numerical study on the berthing problem.

Table 1.2 Recent papers for numerical study on berthing problem

Year	Author	Berthing Problem	Numerical Method	Environment
2000	Yoo	Berthing of a Twin-screw ferry	Maneuvering eq.	Calm sea
2002	Doom & Hove	Berthing btw FPSO and tanker	Maneuvering eq.	Calm sea
2003	Huang & Chen	Berthing btw ship and floating pier	CFD	Calm sea
2004	Kong <i>et al.</i>	Berthing ship	CFD	Calm sea
2005	Sakakibara <i>et al.</i>	Lightering operation	Seakeeping eq.(IRF)	Wave
2009	Wilde <i>et al.</i>	Berthing btw FPSO and LNGC	Seakeeping(IRF) & Maneuvering eq.	Wave, Wind, Current
2010	Sasa <i>et al.</i>	Berthing btw ship and pontoon	Seakeeping eq.(IRF)	Wave, Wind, Current
2010	Skejic & Berg	Lightering operation	Seakeeping(IRF) & Maneuvering eq.	Wave
2011	Wang <i>et al.</i>	Berthing tanker	CFD	Calm sea

Another numerical approach to the berthing problem involves the use of CFD(Computational Fluid Dynamics) to compute the hydrodynamic force during the operation. Since the relative positions of the vessels continuously change during berthing operation, it is very difficult to solve the fluid around the bething vessels numerically. An efficient re-meshing technique or overset grid method is required to tackle the berthing problem. A few studies on the solution of the fluid around a berthing vessel have been attempted to analyze the hydrodynamic force acting on the vessel. Huang and Chen (2003) presented some CFD results for berthing between a floating pier and ship on a calm sea. They solved the Reynolds-averaged Navier–Stokes (RANS) equations using the Chimera grid technique. Kong *et al.*(2004) and Wang *et al.*(2011) calculated the hydrodynamic force acting on a berthing ship using CFD method.

In recent times, some researchers experimentally investigated the berthing problem. Buchner(2005) conducted an experimental study to evaluate the behavior of a tug used to assist the berthing of an LNGC in the presence of waves. He used scaled models of the LNGC and the tug. Push and pull modes are implemented in the experiment. He reported the wave-induced motion of the tug and the fender/towline load between the LNGC and the tug for various wave angles. Teresa(2008) also carried out an experimental study on the hydrodynamic forces induced by a twin-propeller ferry during berthing. Lataire *et al.*(2011) performed a series of captive model test to investigate ship-to-ship interaction forces during lightering operation.

Numerical simulation for berthing problem using the equation of motion

normally assumed that that hydrodynamic characteristics on the berthing path is same as the quasi-steady responses. Thus, dynamic effect is not considered properly in these simulations. A few CFD studies, in which the fluid around berthing vessels is directly solved, mainly focused on the berthing problem in calm sea. These previous studies suggest that more systematic studies are required for the wave-induced motion response and hydrodynamic force during berthing operation in wave.

1.2.3 Application of Finite element method in floating body problem

Although finite element method has been applied widely used in various engineering fields such as structural analysis, its application to the floating body problem is quite limited rather than the use of boundary element techniques. This is because the finite element method requires a volume grid and longer computation time compared to the boundary element method for linear problems. However, the stability and efficiency of the finite element method makes it preferable for nonlinear free-surface or moving boundary problems.

The pioneering work of solving free-surface flow problems by the finite element method was done by Bai and Yeung (1974). They proposed a modified variational method based on eigenfunction expansion for solving the forced motion and diffraction problem of a floating body. Bai (1975, 1977) proposed a finite element technique for solving the diffraction and radiation

waves around a cylindrical body. Bai (1981) also presented a localized finite element method for solving three-dimensional ship motion problems. Bai *et al.*(1989) extended the classical finite element method for solving nonlinear free surface flow problems around a floating body.

Table 1.3 Papers about finite element method for floating body problem

Year	Author	Problem	Model	Domain	Order
1974	Bai & Yeung	Diffraction & Radiation	Cylinder in 2D	Freq.	Linear
1975	Bai	Diffraction	Cylinder in 2D	Freq.	Linear.
1977	Bai	Radiation	Cylinder in 2D	Freq	Linear
1981	Bai	Diffraction & Radiation	Ship in 3D	Freq.	Linear
1989	Bai <i>et al.</i>	Diffraction	Wedge shape in 3D	Time	Nonlinear
2003	Kyoung <i>et al.</i>	Diffraction	Wedge shape in 3D	Time	Nonlinear
2007	Turnbull <i>et al.</i>	Diffraction	Circle in 2D	Time	Nonlinear
2007	Yan & Ma	Diffraction & Radiation	Cylinder in 2D	Time	Nonlinear
2008	Wang & Wu	Diffraction & Radiation	Rectangular in 2D	Time	Second
2009	Nam <i>et al.</i>	Diffraction & Radiation	Ship in 3D	Time	Linear
2011	Hong & Nam	Diffraction	Offshore structure in 3D	Time	Second

In recent times, Kyoung *et al.*(2003) studied the nonlinear free-surface flows around a three-dimensional transom stern using the finite element method with fully nonlinear free-surface boundary conditions. Recently, Turnbull *et al.* (2007) and Yan & Ma (2007) solved the floating body problem in two dimensions using nonlinear boundary conditions. Wang & Wu (2008) also solved the second-order problem of floating bodies on waves in two dimensions. Recently, Nam *et al.*(2009) showed the application of the finite

element method to the linear ship motion problem in the time domain. Hong and Nam (2011) developed the finite element method in the time domain to solve the second-order wave forces acting on single and multiple floating bodies. Table 1.3 shows some selected papers about the application of finite element method for floating body problem.

1.3 Objective & Work scope

The main objectives of this study include the development of a new numerical method for solving the berthing problem between two floating bodies, and investigation of the berthing responses, especially the wave-induced motion and force responses.

Because the berthing problem is inherently a transient problem involving large planar motions of vessels, conventional numerical methods for solving the floating body problem are not applicable. It is thus necessary to develop a new numerical method for investigating the berthing responses of vessels. In this study, which was based on the potential flow theory, a mathematical formulation of the berthing problem is derived with respect to the earth-fixed coordinate system. The finite element method is used to solve the Laplace equation of the moving boundary problem efficiently. Because a berthing operation is usually performed in a moderate sea state, linearized free-surface and body boundary conditions are adopted. One of the difficulties of solving a fluid domain is the handling of the mesh around a vessel moving on a horizontal plane. In this study, a new algorithm for generating the mesh

is developed using the concept of local and global mesh. The local mesh refers to the body-fixed grid attached to the moving vessel, and the global meshing is the earth-fixed Cartesian mesh. In the new algorithm, the re-mesh process is replaced by a simple connection operation between the local and global meshes.

Using the developed numerical method, two berthing problems are numerically investigated. In the first problem, the focus is on the hydrodynamic forces acting on the two barges during berthing under various wave conditions. The effects of the wave frequency, heading, barge size, and berthing path are examined through a series of numerical computations. Some of the simulation results are compared with experimental data to validate the proposed numerical method. The second considered berthing problem concerned berthing between an FPSO unit and a shuttle tanker in waves. In this case, the focus is on the wave-induced motion responses during berthing operation. The characteristics of the wave-induced motion response are investigated under various wave and berthing conditions. The sheltering effect and amplitude modulation during the operation are examined by simulation based on the proposed numerical method. The berthing problem on irregular sea is also considered.

1.4 Outline of the thesis

The berthing problem and the state of the related art have been introduced and discussed in the present chapter. The main objectives and the scope of the

present study are also expressed. In Chapter 2, the theoretical background of the study is presented. The exact and linearized boundary value problem for the berthing problem are described with respect to earth-fixed coordinate system. The mathematical formulations for the first and second hydrodynamic forces are also explained. In Chapter 3, the proposed numerical method is explained in detail. The finite element method with weak formulation and time-integration method for the free-surface boundary conditions is described. The new mesh generation algorithm for solving the moving boundary problem is also presented based on the concept of local and global mesh system. The complete procedure for solving the berthing problem is finally presented in this chapter.

Chapters 4 and 5, which may be considered as constituting the main part of this thesis, present the computational results on two berthing problems. In chapter 4, the berthing operation between two rectangular barges is considered under various regular wave conditions. The effect of the wave frequency and heading on hydrodynamic forces are examined. The calculation results are also validated by comparison with experimental data. Chapter 5 examines the berthing problem between FPSO and a shuttle tanker. Berthing in a head sea is initially considered, with a Focus on the wave-induced motion response during the operation. Berthing in quartering and beam seas are thereafter examined. The numerical simulation results for an irregular sea are also presented.

Finally, in Chapter 6, all the issues addressed in the study are discussed and some conclusions are drawn.

Chapter 2. Theoretical Formulation

2.1 Exact boundary value problem

The boundary value problem for the berthing operation could be formulated with respect to earth-fixed coordinate system because the relative positions of the two vessels continuously change during the berthing operation. Fig. 2.1 shows the coordinate system for the berthing problem in this study. It is assumed that the berthing ship moves at a given speed and simultaneously undergoes wave-induced motion with six degree-of-freedom (DOF). The stationary vessel (i.e. offshore structure or crane vessel) is assumed to exhibit only wave-induced motion. Low-frequency slow drift motions induced by the mooring system are not considered.

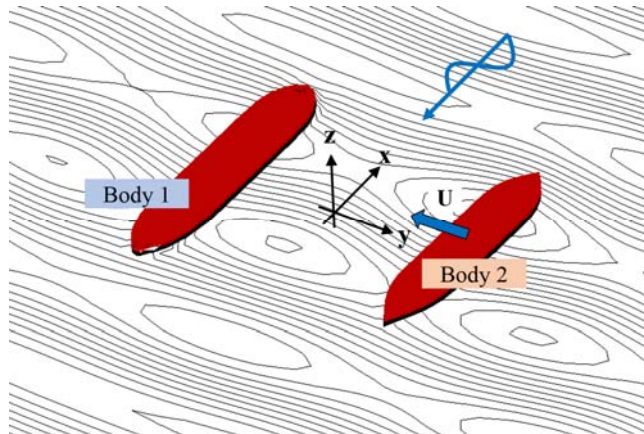


Fig. 2.1 Coordinate system for the berthing problem

The potential flow theory is used to solve the berthing problem in the present study by assuming an inviscid, incompressible fluid and irrotational flow. The velocity potential function could be defined inside the fluid domain surrounding the floating bodies. The exact boundary value problem for a given berthing problem is obtained as follows:

$$\nabla^2\Phi = 0 \quad \text{in } \Omega \quad (2.1)$$

$$\frac{\partial\Phi}{\partial t} = -g\zeta - \frac{1}{2}\nabla\Phi \cdot \nabla\Phi \quad \text{on } z = \zeta \quad (2.2)$$

$$\frac{\partial\zeta}{\partial t} = \frac{\partial\Phi}{\partial z} - \nabla\Phi \cdot \nabla\zeta \quad \text{on } z = \zeta \quad (2.3)$$

$$\frac{\partial\Phi}{\partial n} = \overline{N_1} \cdot \overline{V_{B1}} \quad \text{on } S_{B1} \quad (2.4)$$

$$\frac{\partial\Phi}{\partial n} = \overline{N_2} \cdot \overline{V_{B2}} \quad \text{on } S_{B2} \quad (2.5)$$

The governing equation of the potential flow is the Laplace equation presented as Eq. (2.1), where Φ is velocity potential defined in the entire fluid domain Ω . The nonlinear free surface boundary condition is presented in Eqs. (2.2) and (2.3). Here, ζ is the wave elevation on the free-surface. g is the gravitational constant. Eq. (2.2) expresses the dynamic free-surface boundary condition, which means that the pressure on the free surface is equal to the atmospheric pressure. Eq. (2.3) expresses the kinematic free-surface boundary condition, which is derived from the material derivative of free-surface boundary. Eqs. (2.4) and (2.5) give the body boundary conditions for

the first and second floating bodies, respectively. Here, \overline{N}_1 and \overline{N}_2 are the unit normal vectors from the boundaries of the first and second floating bodies, respectively. The normal vector is defined as pointing out of the fluid domain. \overline{V}_{B1} and \overline{V}_{B2} are the velocity vectors of the first and second body boundaries, respectively. Fig. 2.2 is a schematic of the exact boundary value problem for the berthing problem between two floating bodies.

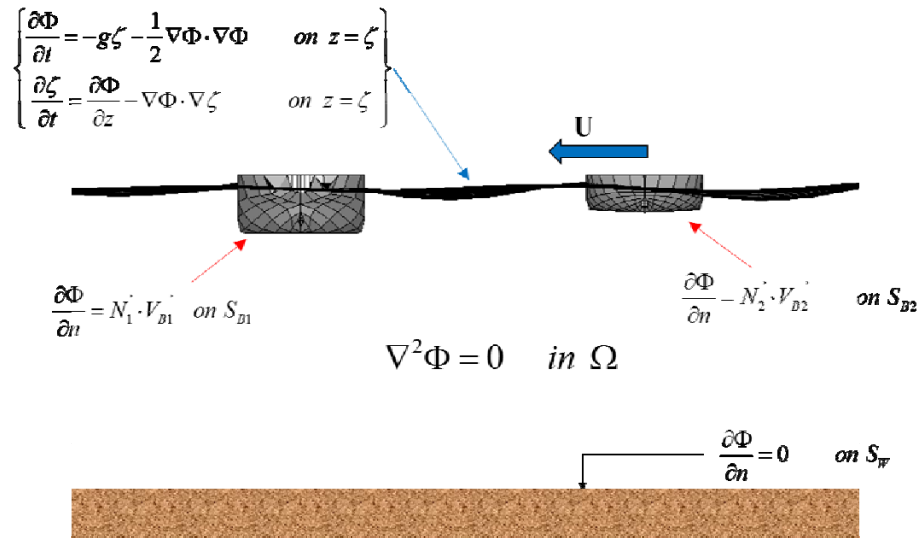


Fig. 2.2 Exact boundary value problem for the berthing problem between two floating bodies

2.2 Linearized boundary value problem

To obtain the linearized boundary value problem, the following perturbation series expansion is applied to the velocity potential and wave elevation.

$$\Phi = \phi^{(1)} + \phi^{(2)} + \dots \quad (2.6)$$

$$\zeta = \zeta^{(1)} + \zeta^{(2)} + \dots \quad (2.7)$$

Where $\phi^{(1)}$ and $\phi^{(2)}$ are the first- and second-order velocity potentials, respectively. $\zeta^{(1)}$ and $\zeta^{(2)}$ are the first- and second-order free-surface elevations, respectively.

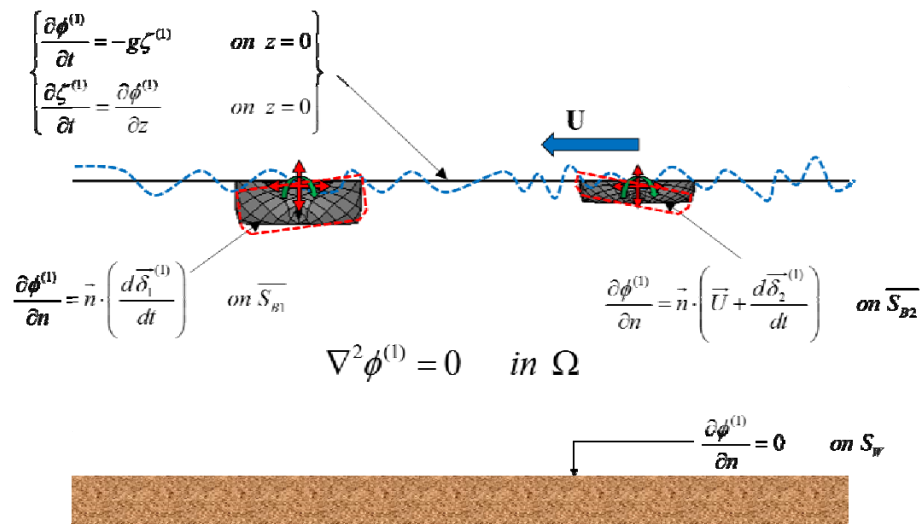


Fig. 2.3 First-order boundary value problem for the berthing problem between two floating bodies

The first-order boundary value problem for the berthing problem is obtained as follows:

$$\nabla^2 \phi^{(1)} = 0 \quad \text{in } \Omega \quad (2.8)$$

$$\frac{\partial \phi^{(1)}}{\partial t} = -g \zeta^{(1)} \quad \text{on } z = 0 \quad (2.9)$$

$$\frac{\partial \zeta^{(1)}}{\partial t} = \frac{\partial \phi^{(1)}}{\partial z} \quad \text{on } z = 0 \quad (2.10)$$

$$\frac{\partial \phi^{(1)}}{\partial n} = \vec{n} \cdot \left(\frac{d \vec{\delta}_1^{(1)}}{dt} \right) \quad \text{on } \overline{S_{B1}} \quad (2.11)$$

$$\frac{\partial \phi^{(1)}}{\partial n} = \vec{n} \cdot \left(\vec{U} + \frac{d \vec{\delta}_2^{(1)}}{dt} \right) \quad \text{on } \overline{S_{B2}} \quad (2.12)$$

where $\vec{\delta}_1^{(1)}$ and $\vec{\delta}_2^{(1)}$ are the 6-dof displacement vectors of the two vessels. \vec{U} is a berthing velocity vector. $\overline{S_{B1}}$ and $\overline{S_{B2}}$ are the mean wetted-surface area of the vessels. \vec{n} is the unit normal vector defined on mean wetted-surface of the vessels. The superscripts indicate the order of the problem, and the subscripts the vessel number. The displacement vectors ($\vec{\delta}^{(1)}$) are composed of 3-dof translation vector ($\vec{\xi}^{(1)}$) and 3-dof rotation vector ($\vec{\alpha}^{(1)}$) like follows:

$$\vec{\delta}_1^{(1)} = \vec{\xi}_1^{(1)} + \vec{\alpha}_1^{(1)} \times \vec{x} \quad (2.13)$$

$$\vec{\delta}_2^{(1)} = \vec{\xi}_2^{(1)} + \vec{\alpha}_2^{(1)} \times \vec{x} \quad (2.14)$$

The second-order boundary value problem for the berthing problem is

obtained as follows:

$$\nabla^2 \phi^{(2)} = 0 \quad \text{in } \Omega \quad (2.15)$$

$$\frac{\partial \phi^{(2)}}{\partial t} = -g \zeta^{(2)} - \frac{1}{2} \nabla \phi^{(1)} \cdot \nabla \phi^{(1)} - \zeta^{(1)} \frac{\partial}{\partial z} \left(\frac{\partial \phi^{(1)}}{\partial t} \right) \quad \text{on } z=0 \quad (2.16)$$

$$\frac{\partial \zeta^{(2)}}{\partial t} = \frac{\partial \phi^{(2)}}{\partial z} - \nabla \phi^{(1)} \cdot \nabla \zeta^{(1)} + \zeta^{(1)} \frac{\partial}{\partial z} \left(\frac{\partial \phi^{(1)}}{\partial z} \right) \quad \text{on } z=0 \quad (2.17)$$

$$\frac{\partial \phi^{(2)}}{\partial n} = \vec{n} \cdot \left(\frac{d\bar{\delta}_1^{(2)}}{dt} \right) + \vec{n}^{(1)} \cdot \left(\frac{d\bar{\delta}_1^{(1)}}{dt} \right) - \vec{n}^{(1)} \cdot \nabla \phi^{(1)} + \vec{n} \cdot \left(\bar{\delta}_1^{(1)} \cdot \nabla \right) (\nabla \phi^{(1)}) \quad \text{on } \overline{S_{B1}} \quad (2.18)$$

$$\frac{\partial \phi^{(2)}}{\partial n} = \vec{n} \cdot \left(\frac{d\bar{\delta}_2^{(2)}}{dt} \right) + \vec{n}^{(1)} \cdot \left(\bar{U} + \frac{d\bar{\delta}_2^{(1)}}{dt} \right) - \vec{n}^{(1)} \cdot \nabla \phi^{(1)} + \vec{n} \cdot \left(\bar{\delta}_2^{(1)} \cdot \nabla \right) (\nabla \phi^{(1)} - \bar{U}) \quad \text{on } \overline{S_{B2}} \quad (2.19)$$

The second-order free surface boundary conditions in Eqs. (2.16) and (2.17) contain additional forcing terms, which are product of the first-order potential and elevation. Similarly, there are additional terms on the right hand side of body boundary conditions expressed by Eqs. (2.18) and (2.19). In this study, only the first-order boundary value problem is used to investigate the given berthing problem.

To decompose the boundary value problem, the conventional decomposition method is used to distinguish incident and disturbed wave potential shown in Eqs. (2.20). In this case, the disturbed wave potential

includes the scatted and radiation potential. The last terms are the velocity potential due to berthing on a calm sea, which is beyond the scope of this study. Similar decomposition can be applied to wave elevation like Eq. (2.21)

$$\phi^{(1)} = \phi_I^{(1)} + \phi_D^{(1)} + \phi_C^{(1)} \quad (2.20)$$

$$\zeta^{(1)} = \zeta_I^{(1)} + \zeta_D^{(1)} + \zeta_C^{(1)} \quad (2.21)$$

The first-order boundary value problem for the disturbed wave potential is obtained as follows:

$$\nabla^2 \phi_D^{(1)} = 0 \quad \text{in } \Omega \quad (2.22)$$

$$\frac{\partial \phi_D^{(1)}}{\partial t} = -g \zeta_D^{(1)} \quad \text{on } z=0 \quad (2.23)$$

$$\frac{\partial \zeta_D^{(1)}}{\partial t} = \frac{\partial \phi_D^{(1)}}{\partial z} \quad \text{on } z=0 \quad (2.24)$$

$$\frac{\partial \phi_D^{(1)}}{\partial n} = -\frac{\partial \phi_I^{(1)}}{\partial n} + \vec{n} \cdot \frac{d\vec{\delta}_1^{(1)}}{dt} \quad \text{on } \overline{S_{B1}} \quad (2.25)$$

$$\frac{\partial \phi_D^{(1)}}{\partial n} = -\frac{\partial \phi_I^{(1)}}{\partial n} + \vec{n} \cdot \frac{d\vec{\delta}_2^{(1)}}{dt} \quad \text{on } \overline{S_{B2}} \quad (2.26)$$

2.3 Hydrodynamic Force

The hydrodynamic forces acting on the body are determined by integrating the pressure on the wetted body surfaces. The first-order hydrodynamic forces acting on the floating bodies are as follows:

$$\vec{F}^{(1)} = \iint_{\overline{S_B}} p^{(1)} \vec{n} dS = -\rho \iint_{\overline{S_B}} \frac{\partial \phi^{(1)}}{\partial t} \vec{n} dS \quad (2.27)$$

where, $p^{(1)}$ indicates the linear hydrodynamic pressure. ρ is the fluid density.

In this study, the acceleration potential method is used for a more accurate evaluation of the time derivative of the velocity potential. It is well known that a convergence issue arises when the finite difference formula is used to solve a moving boundary problem. The boundary value problem for the acceleration potential is expressed as follows:

$$\nabla^2 \phi_{D,t}^{(1)} = 0 \quad \text{in } \Omega \quad (2.28)$$

$$\phi_{D,t}^{(1)} = -g \zeta_D^{(1)} \quad \text{on } z = 0 \quad (2.29)$$

$$\frac{\partial \phi_{D,t}^{(1)}}{\partial n} = -\frac{\partial \phi_{1,t}^{(1)}}{\partial n} + \vec{n} \cdot \frac{d^2 \vec{\delta}_1^{(1)}}{dt^2} \quad \text{on } \overline{S_{B1}} \quad (2.30)$$

$$\frac{\partial \phi_{D,t}^{(1)}}{\partial n} = -\frac{\partial \phi_{1,t}^{(1)}}{\partial n} + \vec{n} \cdot \frac{d^2 \vec{\delta}_2^{(1)}}{dt^2} \quad \text{on } \overline{S_{B2}} \quad (2.31)$$

The second-order hydrodynamic force can be determined using the following equations:

$$\begin{aligned}
\vec{F}^{(2)} = & \frac{1}{2} \rho g \oint_{WL} [\eta^{(1)} - \delta_V^{(1)}]^2 \vec{n} dl \\
& - \rho \iint_{\bar{S}_B} \left[\frac{1}{2} \nabla \phi^{(1)} \cdot \nabla \phi^{(1)} + (\vec{\xi}^{(1)} + \vec{\alpha}^{(1)} \times \vec{x}) \cdot \nabla \phi_i^{(1)} \right] \vec{n} dS \\
& + \vec{\alpha}^{(1)} \times \vec{F}^{(1)} - \rho \iint_{\bar{S}_B} \phi_i^{(2)} \vec{n} dS
\end{aligned} \tag{2.32}$$

where, $\delta_V^{(1)}$ is the vertical body displacement at the waterline. Because only the first-order boundary value problem is solved in the present study, the second-order velocity potential is not determined. Thus, the second-order hydrodynamic force is computed without considering the effect of the second-order potential. With regard to the second-order drift force, the contribution of the second-order potential is insignificant. In general, the first and second terms in the expression of a second-order hydrodynamic force are dominant in the solution of a general floating body problem.

Chapter 3. Numerical Method

3.1 Finite element method

The weak formulation of the governing equation for the potential flow could be obtained by introducing the test functions:

$$\iiint_{\Omega} \nabla \phi \cdot \nabla \psi dV - \iint_{\partial\Omega} \frac{\partial \phi}{\partial n} \psi dS = 0 \quad (3.1)$$

The fluid domain is discretized using a finite number of elements, and the velocity potential function is approximated as a linear summation of the continuous and differentiable test functions. The velocity potential and wave elevation can be expressed as Eqs. (3.2) and (3.3), respectively.

$$\phi(x, y, z, t) = \sum_i \phi_i(t) N_i(x, y, z) \quad (3.2)$$

$$\zeta(x, y, t) = \sum_k \zeta_k(t) M_k(x, y) \quad (3.3)$$

where N_i is a three-dimensional basis function defined in the entire fluid domain, and M_k is a two-dimensional basis function on the free surface. Eight-node hexahedral elements and four-node quadrilateral elements are used in this study. The boundary value problem is finally transformed into linear algebraic equations as follows:

$$K_{ij}\phi_j = F_i \quad (3.4)$$

$$T_{ik}\dot{\zeta}_k = P_{ik}(\phi_{n,k} + f_{\zeta,k}) \quad (3.5)$$

$$T_{ik}\dot{\phi}_k = P_{ik}(-g\zeta_k + f_{\phi,k}) \quad (3.6)$$

where,

$$K_{ij} = \iiint_{\Omega} \nabla N_i \cdot \nabla N_j dV \quad (3.7)$$

$$F_i = \iint_{S_B} \frac{\partial \phi}{\partial n} N_i dS \quad (3.8)$$

$$T_{ik} = P_{ik} = \iint_{S_F} M_i M_k dS \quad (3.9)$$

The solution of the Laplace equation is obtained from Eq. (3.4). The free-surface velocity potential and elevation are integrated in time by Eqs. (3.5) and (3.6). In the present study, the conjugate gradient method is employed for solving Eqs. (3.4)-(3.6). $f_{\zeta,k}$ and $f_{\phi,k}$ are the forcing terms attributed to the velocity potential and wave elevation on the free surface, respectively.

3.2 Free-surface integration

The wave elevation and velocity potential on the free-surface boundary can be integrated in time by applying free-surface boundary conditions such as those expressed by Eqs. (3.10) and (3.11). In this study, an artificial wave damping zone is introduced to satisfy the radiation condition numerically. An artificial damping term is added to the velocity potential in the dynamic free-surface

condition, and the wave elevation is forced to damp out in the kinematic free-surface condition. The region of about 2~3 times of the wavelength is taken as the wave damping zone. The final free-surface boundary conditions including the artificial damping term are expressed as follows:

$$\frac{\partial \phi_D^{(1)}}{\partial t} = -g \zeta_D^{(1)} - \mu \phi_D^{(1)} \quad \text{on } z=0 \quad (3.10)$$

$$\frac{\partial \zeta_D^{(1)}}{\partial t} = \frac{\partial \phi_D^{(1)}}{\partial z} - \mu \zeta_D^{(1)} \quad \text{on } z=0 \quad (3.11)$$

The fourth-order Adams-Bashforth-Moulton method is applied for time integration of the free-surface condition. When convergence criteria is set to be 10^{-4} times of the wave elevation, a converged solution is obtained after 4-6 iterations.

$$y_{j+1}^{(0)} = y_j + \frac{\Delta t}{24} (55f_j - 59f_{j-1} + 37f_{j-2} - 9f_{j-3}) \quad (3.12)$$

$$y_{j+1}^{(k+1)} = y_j + \frac{\Delta t}{24} (9f_{j+1}^{(k)} + 19f_j - 5f_{j-1} + f_{j-2}) \quad (3.13)$$

3.3 Algorithm for mesh generation

Since the berthing problem is inherently a moving boundary problem, a technique for re-meshing at each time step is required for time-domain simulation. Simple and robust algorithm for mesh generation is required for efficient numerical scheme of the berthing problem. In this study, the concept

of local and global meshing is employed in the algorithm, and the re-mesh process is replaced by a simple connection operation. A local mesh refers to the body-fixed mesh surrounding a floating body, and a global mesh is the earth-fixed mesh extracted from the Cartesian grid system. It is assumed that the berthing vessel could undergo a large horizontal motion in only the translation direction. This means that the local mesh without modification may be located anywhere within the global mesh during the simulation.

The procedure for the new mesh generation algorithm consists of the following eight steps:

- 1) Generation of the background mesh of the Cartesian grid.
- 2) Generation of the local meshes surrounding the floating bodies.
- 3) Positioning of the local mesh at a given point (X, Y).
- 4) Extraction of the global mesh from the background mesh by eliminating overlapping elements.
- 5) Combination of the local and global meshes (as shown in Fig. 3.1).
- 6) Merging of the local and global meshes by a connection operation (as shown in Fig. 3.2).
- 7) Identification of the body boundary and free-surface boundary.
- 8) Obtaining the updated new mesh.

Fig. 3.1 shows example for proposed mesh generation algorithm for single body problem. Fig. 3.3 depicts present mesh generation of berthing problem

between two floating bodies. In this algorithm, the mesh on body surface is not changed during the simulation, which makes it possible the accurate integration of hydrodynamic force. Another advantage of the present re-mesh algorithm is that solution interpolation between old and updated meshes become quite simple. Fig. 3.2 shows typical connection operation for merging local and global meshes.

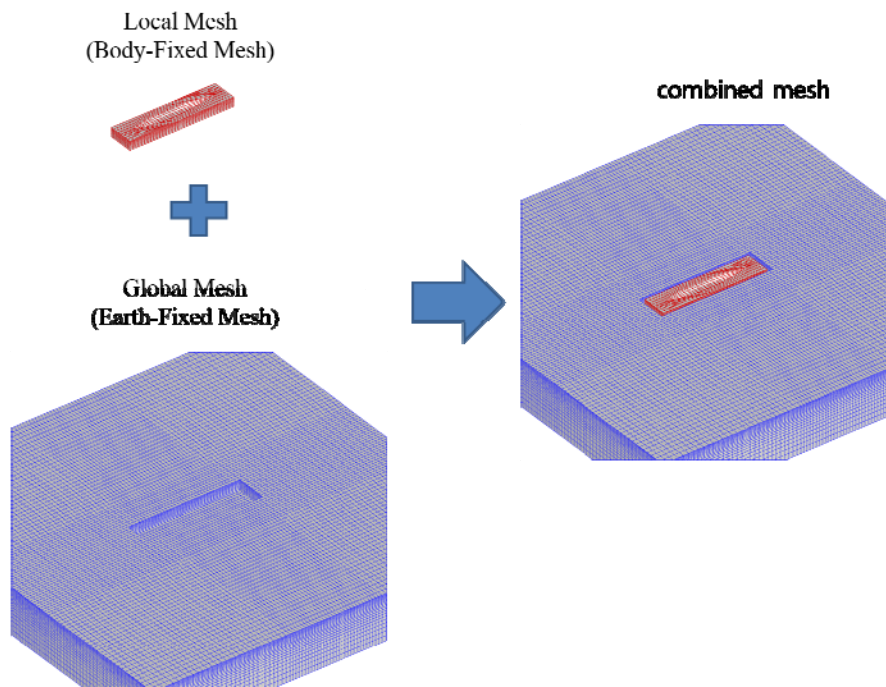


Fig. 3.1 Local and global mesh for single floating body

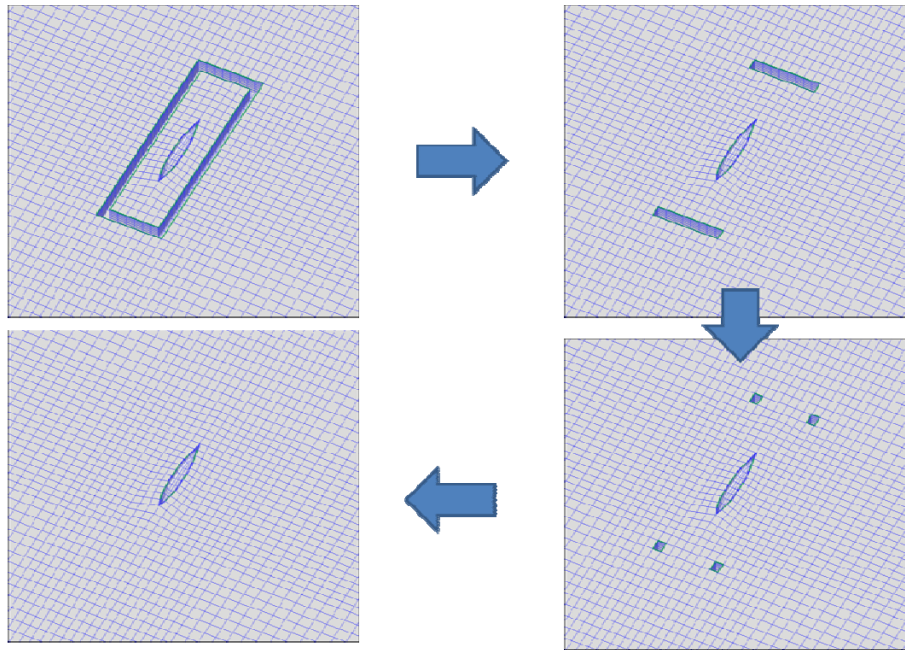


Fig. 3.2 Connection operation for merging meshes

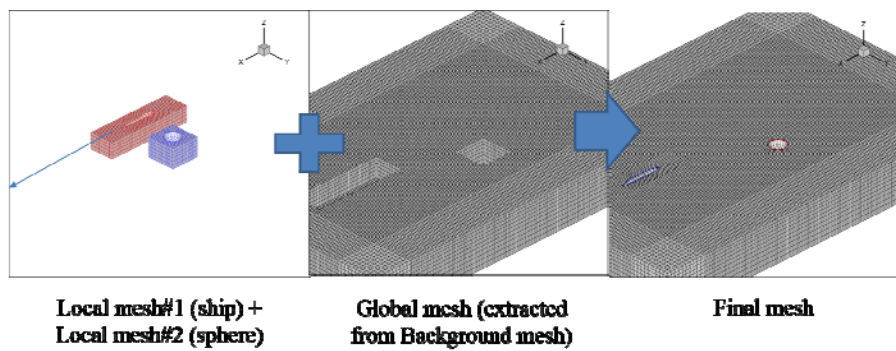


Fig. 3.3 Mesh generation algorithm for two floating bodies

3.4 Solution Procedure

The solution procedure of the present study consisted of the following five steps:

- 1) The Laplace equation with the boundary conditions is solved using the finite element method.
- 2) The time integrations of the free-surface elevation and velocity potential are performed using the free-surface boundary conditions.
- 3) The first and second steps are iterated until the solution converged.
- 4) A new mesh is generated using the re-mesh algorithm.
- 5) The solution is updated for the new mesh by interpolation (Fig. 3.4)

The flow chart for the above solution procedure can be found in Fig. 3.5.

The summary of the present numerical method is presented in Table 3.1.

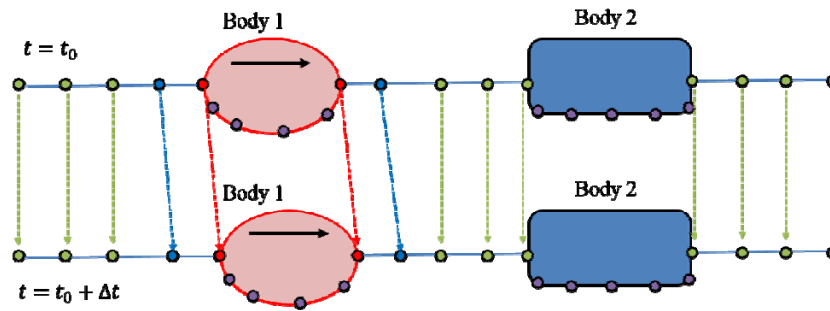


Fig. 3.4 Schematic diagram for solution interpolation

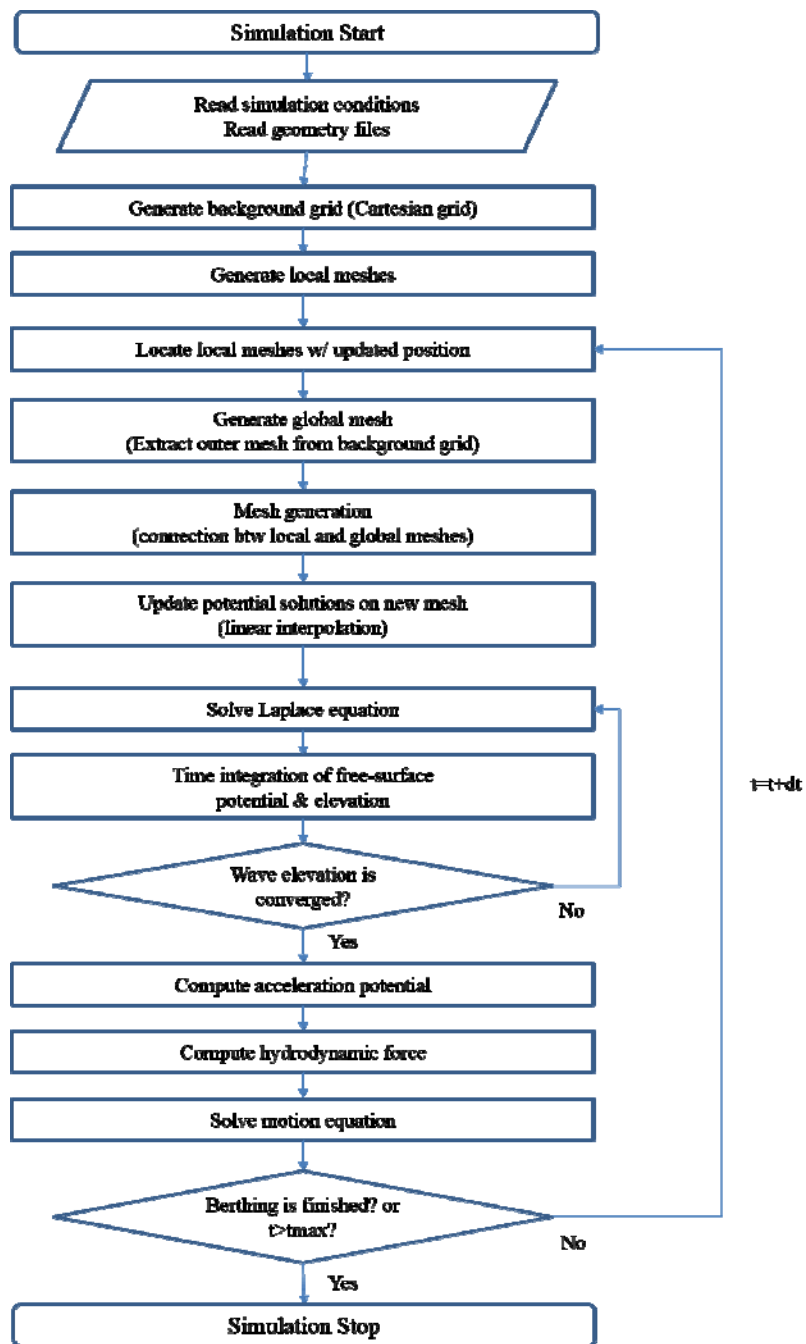


Fig. 3.5 Flow chart for the present solution procedure

Table 3.1 Summary of numerical method

No	Item	Numerical Method
1	Laplace equation	Finite element method (8-node hexahedral element)
2	Matrix Solver	Conjugate gradient method
3	Free-surface Integration	4 th -order Adams-Bashforth-Moulton method w/ weight residual method
4	Radiation Condition	Numerical damping zone
5	Force Computation	Acceleration potential method
6	Motion Time-integration	Newmark-Beta method
7	Mesh generation algorithm	New re-mesh technique w/ global & local mesh concept
8	Solution interpolation	Linear interpolation (using transportation eq.)

3.4 Validation of the numerical method

3.4.1 Wave-induced motion response of hemisphere

To validate the present numerical scheme, it is used to solve the motion of a hemisphere in waves. Fig. 3.6 compares the wave-induced motions of the hemisphere determined by the present numerical method (“FEM”) and the higher-order boundary element method (“HOBEM”), respectively.

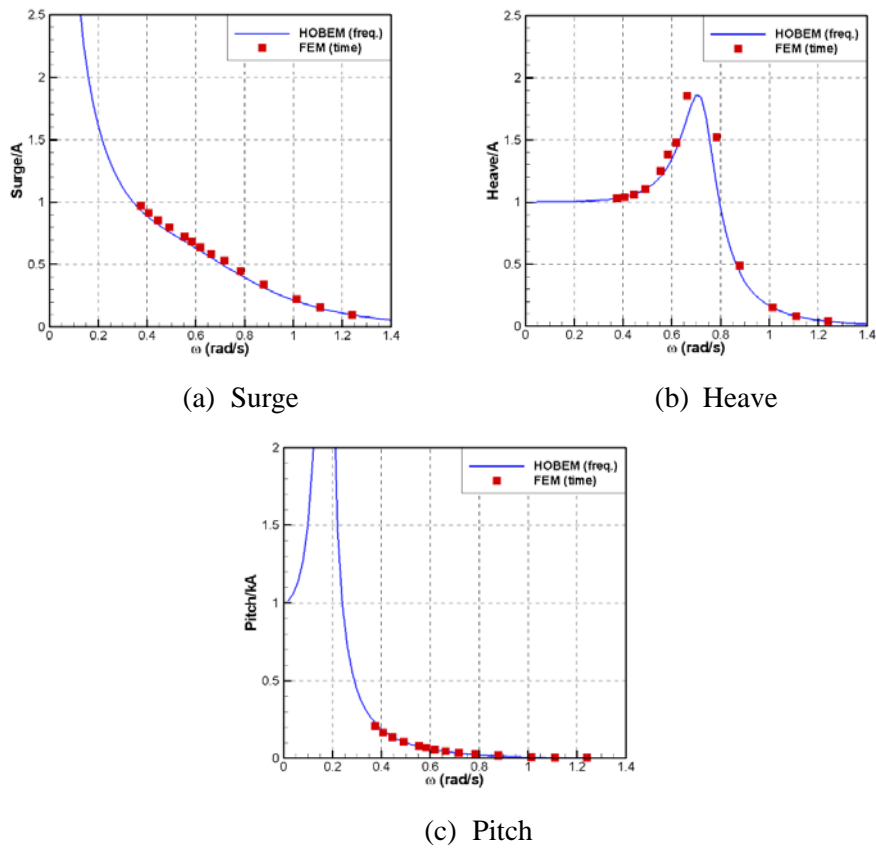


Fig. 3.6 Comparison of motion response of hemisphere in waves

While the present method is applied in the time domain, the higher-order boundary element method is applied in the frequency domain using the Green function of the wave. Good agreement can be observed between the two results.

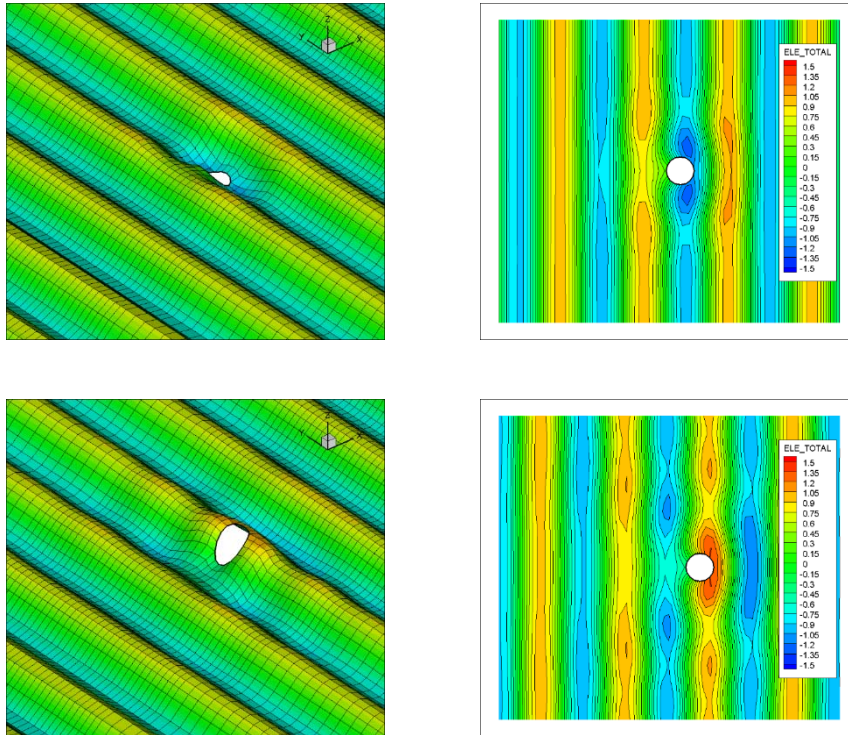


Fig. 3.7 Wave field around hemi-sphere with forward seed in waves

Fig. 3.7 shows the wave field around the hemisphere, which has a forward speed in the regular wave. Fig. 3.8 compares the wave drift forces acting on the sphere determined by the present numerical method and the frequency-domain method by Grue et al.(1992). As can be seen, the present numerical method produced quite accurate solutions for a single floating body.

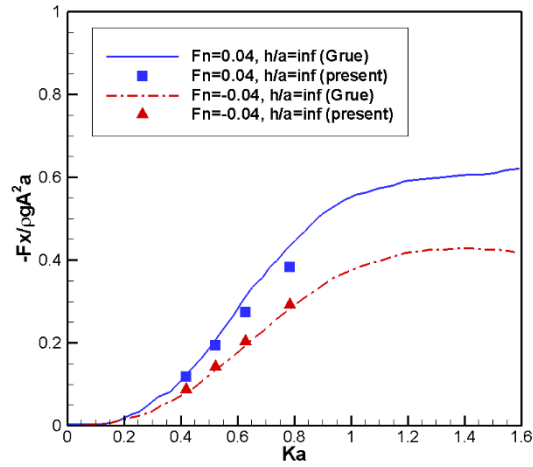
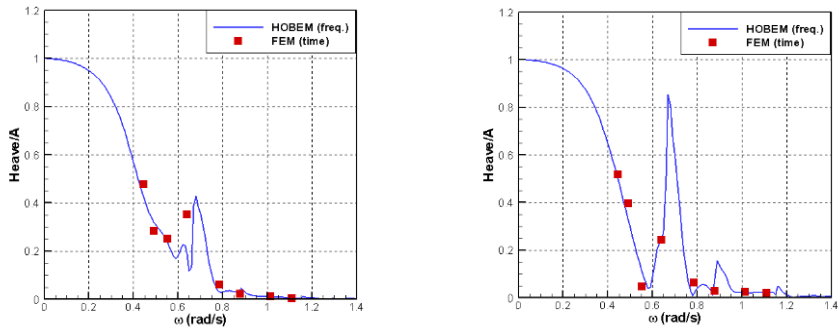


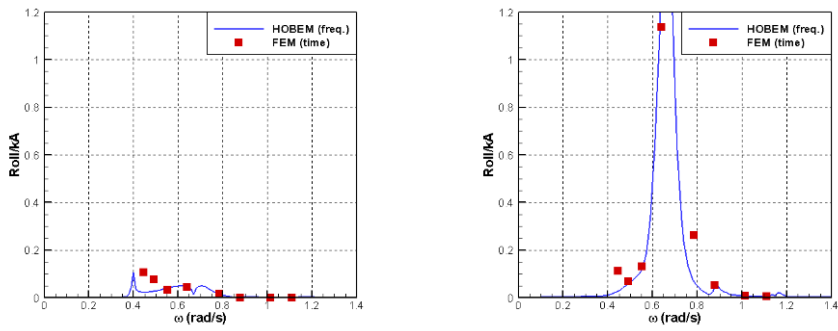
Fig. 3.8 Comparison of wave drift forces acting on the hemi-sphere with forward speed in waves

3.4.2 Side-by-side problem between FPSO & Shuttle tanker

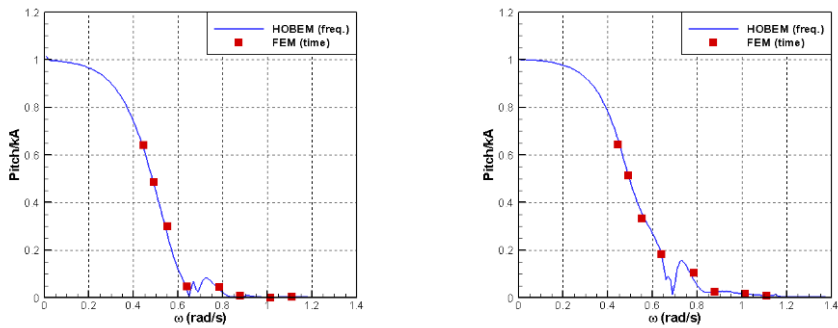
The motion responses of FPSO and shuttle tanker in side-by-side configuration with a separation distance of 50 m are shown in Fig. 3.9. Unlike the response of a single body, the motion response of the shuttle tanker is significantly affected by the presence of the FPSO unit. Likewise, the motion response of the FPSO is changed by the presence of the shuttle tanker. These coupled effects were clearly observed in the roll motions of the two vessels. In particular, the shuttle tanker exhibited resonant roll-and-heave response at about 0.65 rad/s, even in a head sea. These results are in good agreement with the frequency-domain solutions, confirming that the proposed method effectively predicts multi-body coupled motions.



(a) Heave



(b) Roll



(c) Pitch

Fig. 3.9 Comparison of motion response of side-by-side configuration of FPSO(left) and shuttle tanker(right) in head sea (Gap distance=50m)

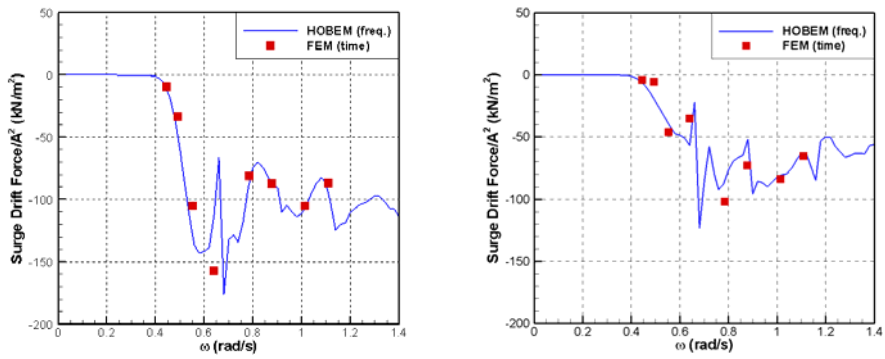
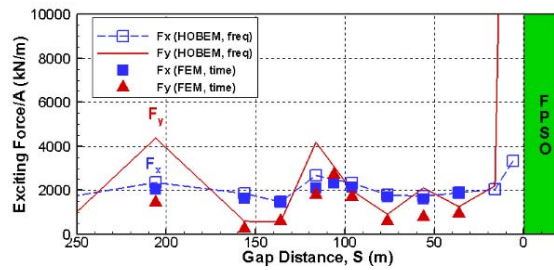
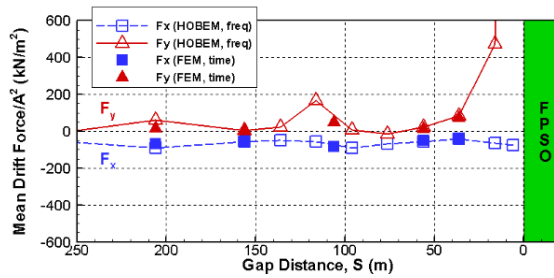


Fig. 3.10 Comparison of surge mean drift fore acting on FPSO and shuttle tanker in waves (Heading 180 deg., Gap distance = 50 m)



(a) Wave excitation force



(b) Wave mean drift force

Fig. 3.11 Comparison of wave excitation and drift forces acting on the shuttle tanker in side-by-side configuration (Heading 180 deg.)

Fig. 3.10 compares the mean wave drift forces acting on the FPSO unit and the shuttle tanker for side-by-side configuration. It is well known that during side-by-side operations, vessels may experience repulsive wave drift forces under head sea conditions. Here again, the present numerical results are generally in good agreement with the frequency-domain solutions.

Fig. 3.11 shows the wave exciting force and moment for various gap distances and wave lengths are compared between the present results and frequency-domain solutions. These results are obtained under a fixed gap distance condition between the FPSO and the shuttle tanker. When the gap distance is less than 50m, it can be seen the Helmholtz resonance (piston mode) produces a large wave excitation force. The agreement between two numerical results is fairly good.

Chapter 4. Berthing Problem between Two Barges

4.1 Problem definition

The developed numerical method is applied to investigate the berthing problem between two rectangular barges, with particular focus on the hydrodynamic forces acting on the barges during the berthing process. It is assumed that the two barges correspond to installation and transportation barges. The initial separation distance between the two barges is 400 m. The berthing speed is constant, and the berthing path is straight. Fig. 4.1 shows the schematic diagram for the present berthing problem between two barges.

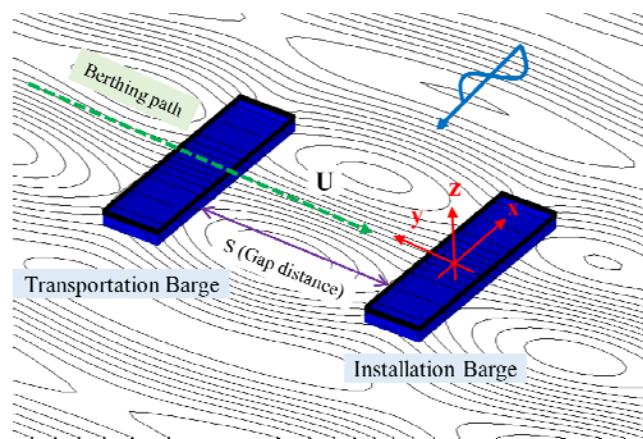


Fig. 4.1 Schematic diagram for berthing problem between two barges

To select the simulation models, the dimensions of the floating crane vessels currently in operation are plotted in Fig. 4.2. The length of the crane barge ranges from 50 to 250 m, whereas the breadth of the barge ranges from 20 to 60 m. The depth of the barge ranges from 5 to 20 m. In this figure, the depth over the 30 m correspond to the semi-submersible crane vessel. In this study, the dimension of the installation barge is selected as 150 m (L) \times 40 m (B) \times 10 m (D). Four different transportation barges are considered to investigate the effect of the barge size on hydrodynamic interaction. The lengths of the barges range from 50m to 150m, whereas the breadths range from 20m to 40m. The drafts of the barges are 5m or 10m. The barges are simply named as barge 1, barge2, barge3 and barge4. Basic model (barge 1) of the transportation barge has the same dimension with the installation barge. Table 4.1 shows the dimensions of transportation barges.

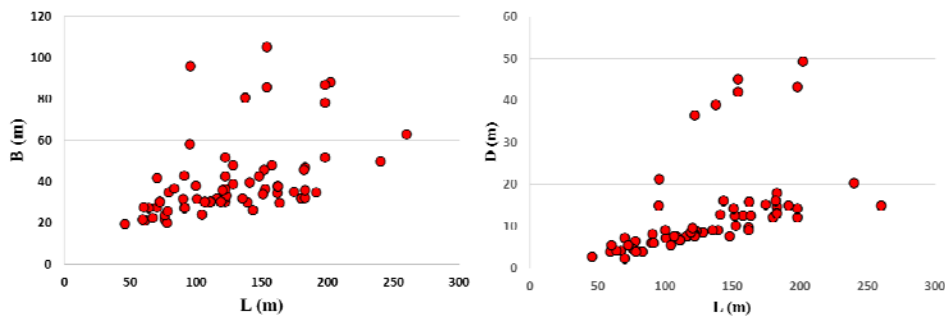


Fig. 4.2 Dimensions for floating crane installation vessel in operation

Table 4.1 Dimensions of the transportation barge

Item	Barge 1	Barge 2	Barge 3	Barge 4
L	150 m	100 m	75 m	50 m
B	40 m	30 m	25 m	20 m
T	10m	10 m	5 m	5 m

There are lots of factors to influence the hydrodynamic problem of the berthing operation. In this chapter, focus is made on several important factors like follows:

- Wave frequency
- Wave heading
- Barge size
- Berthing path

4.2 Wave field and force response in berthing

Numerical simulations are conducted on berthing problem between two rectangular barges. The two barges each have dimensions of 150 m (L) \times 40 m (B) \times 10 m (D). Fig. 4.3 shows the snapshots of the wave fields during the berthing operation when the wavelength is about 1.667 times of the barge length. The transportation barge approaches the port side of the installation barge. As the separation distance between the barges decreases, the scattered waves from each barge meet together in the gap area between the two barges. The initial gap distance is about 350 m, and the final gap distance is about 30 m. It can be seen that the wave elevation in the gap area increases as the separation distance decreases. In particular, a strong wave field clearly develops after 200 s. At this point, the gap distance is less than 50 m, and the wave pattern between the two barges shows gap resonance. The wave fields show that the two barges interact each other via the gap flow.

Fig. 4.4 shows the time series of the first-order wave excitation forces acting on the barges during the berthing operation. The installation and transportation barges experiences almost the same wave excitation forces because the two barges are identical. Not only the amplitude but also the phase angle is the same for the surge, heave, and pitch wave excitation forces. Thus these time series are almost overlapped. In the case of the transverse wave excitation forces (i.e., sway, roll, yaw), however, the phase difference is about 180° with the almost same amplitudes. This means that the transportation barge experiences an out-of-phase transverse force compared to

the installation barge during berthing. This is because strong gap waves between the barges produce a repulsive force acting on the barges in the outward direction from the gap. Another interesting feature is that the force amplitudes constantly changes even under regular wave conditions because the relative positions of the barges continuously decrease during the berthing. For example, the heave wave excitation force shows a local maximum at about 210 s and local minima at around 140 and 280 s. After 300 s, the heave wave force rapidly increases. Similarly, the surge and pitch force time series show a slight increase and decrease. For the transverse wave forces, the force amplitude steadily increases as the transportation barge approaches the installation barge. The two barges are affected by the repulsive wave forces in the outward direction from each other. These amplitude changes are closely related to the reflection characteristics of the gap flow between the two barges. As the barges approach each other, the reflection of the incident wave increases, and the surge force increases. At a certain gap distance, the transmission coefficient is close to unity, and the gap flow becomes stronger. The transverse wave forces increase because of the high wave elevation between the barges. In particular, the sharp increases in the sway, roll, and yaw wave forces are caused by the approximate resonant wave in the gap.

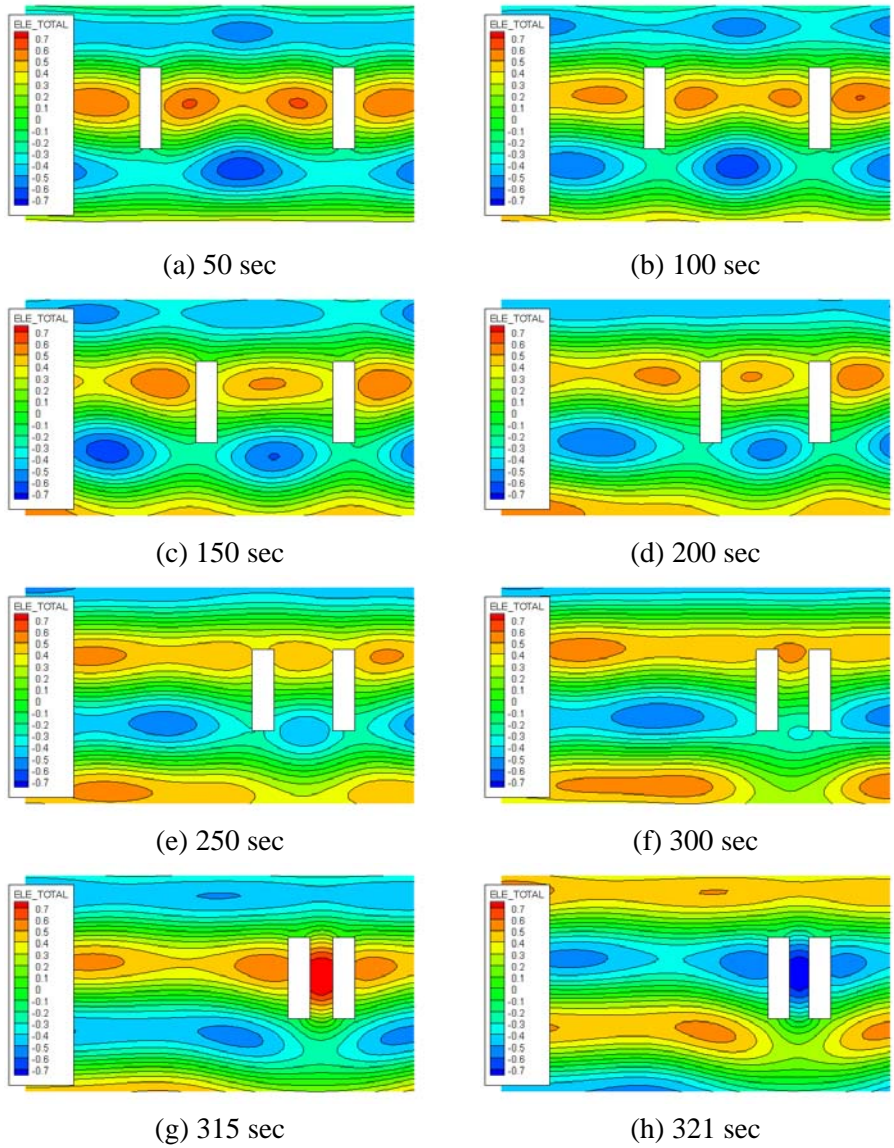
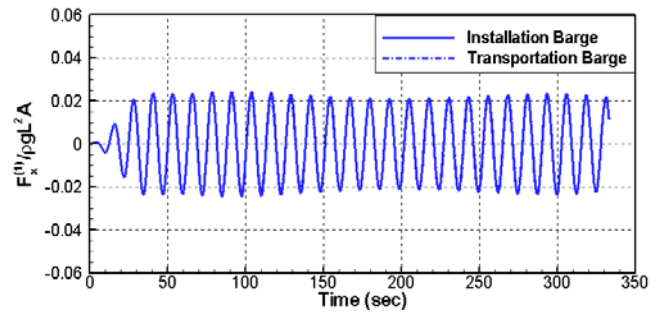
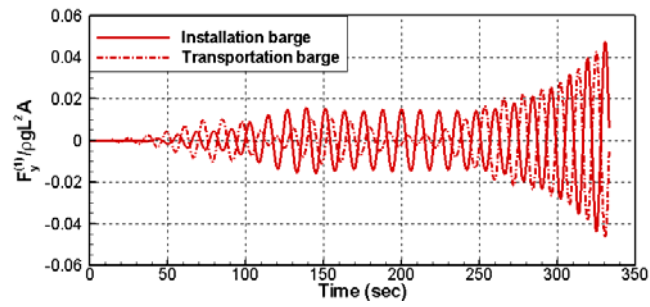


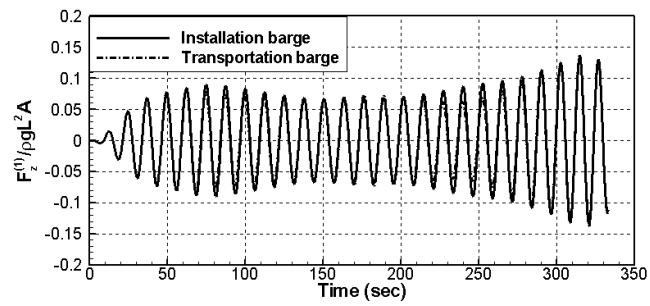
Fig. 4.3 Wave fields around the barges during the berthing operation
(Heading 180°, $\lambda/L=1.667$, $H=1.0$ m, $V=2.0$ kts)



(a) F_x

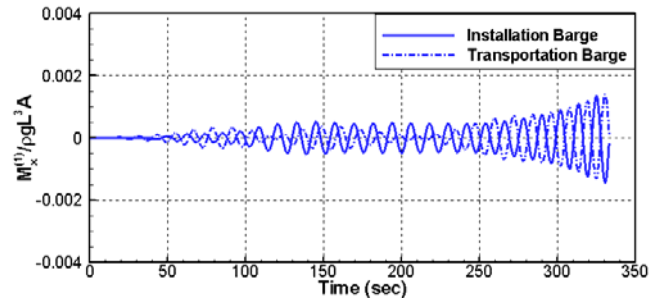


(b) F_y

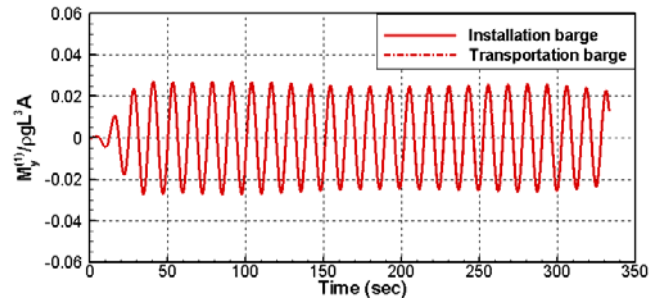


(c) F_z

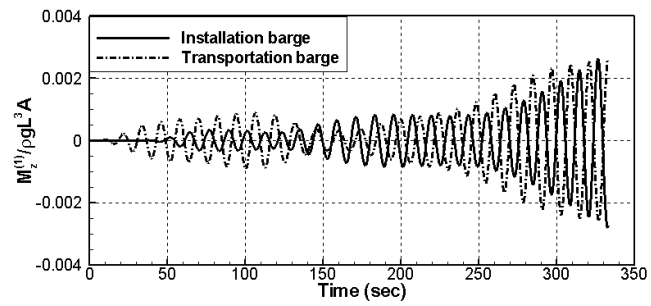
Fig. 4.4 First-order wave forces acting on the barges during the berthing operation (Heading 180° , $\lambda/L=1.667$, $H=1.0$ m, $V=2.0$ kts)



(d) M_x

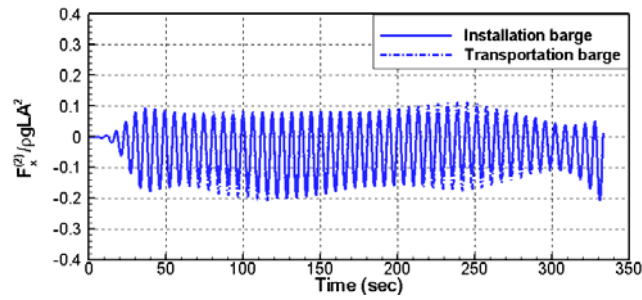


(e) M_y

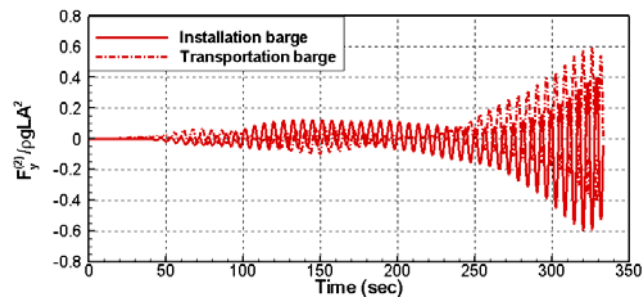


(f) M_z

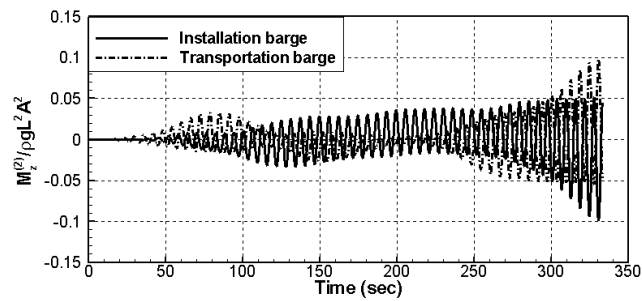
Fig. 4.4 continued



(a) F_x



(b) F_y



(c) M_z

Fig. 4.5 Second-order wave forces acting on the barges during the berthing operation (Heading 180° , $\lambda/L=1.667$, $H=1.0$ m, $V=2.0$ kts)

Fig. 4.5 shows the second-order horizontal wave forces acting on the barges during the berthing operation in regular wave. In this case, the second-order wave force is evaluated from the summation of two quadratic terms in Eq. (2.30). The first term is proportional to the square of the wave elevation and the second term is a function of velocity square. The contribution of second-order potential is not taken into account in this study. Second-order surge wave force shows relatively small variation during the berthing operation. However, second-order sway force shows sharp increase after the 270 second similar to the first-order sway excitation force. In addition, the averaged values of the second-order sway force are opposite between the FPSO and the shuttle tanker. It means the strong repulsive lateral drift force is acting on the barges after the gap distance is below 50m. These rapid increase of second-order wave force is caused by the high wave elevation in the gap due to the approximate resonant condition.

4.3 Effect of wave frequency

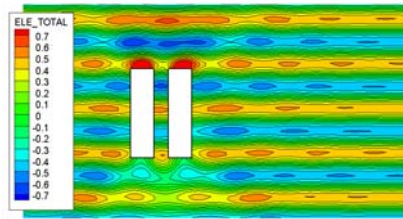
Numerical simulations are performed to investigate the effect of wave frequency on the hydrodynamic forces during the berthing operation. Fig. 4.6 shows the wave fields during the berthing operation under various wave conditions. It is clearly observed that the wave patterns between the two barges are changed according to the wave length. When the wave length is smaller than half of the barge length, the reflection due to the barges is dominant. Meanwhile, when the wave length is same as the barge length, the

high wave elevation can be observed in the gap due to the resonant wave condition of one wave length. These wave pattern corresponds to the second longitudinal gap resonance in side-by-side configuration. If the wave length is 1.333 or 1.667 times of barge length, the wave elevation in the gap becomes very high due to the gap resonance. If the wave length is bigger than the twice of the barge length, most wave turns around the barges rather than go through the gap. This results in the low wave elevation between the barges.

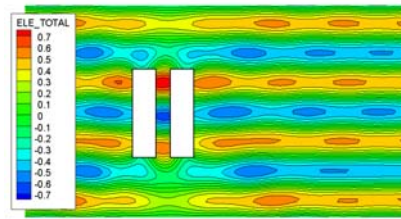
The gap resonance in this problem is similar to the pumping mode resonance in the moonpool. Molin(2001) derived simple analytical formulations for resonant frequency for pumping and sloshing mode in the moonpool problem based on the potential flow theory. Eq. (4.1) is the resonant frequency for pumping mode in two-dimensional moonpool.

$$\omega_0 \approx \sqrt{\frac{g}{h + \left(\frac{b}{\pi}\right) \left\{ \frac{3}{2} + \ln\left(\frac{H}{2b}\right) \right\}}} \quad (4.1)$$

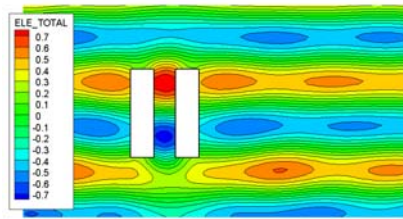
Fig. 4.7 shows the gap resonant frequency based on the side-by-side calculations results by HOBEM. For the comparison, the pumping-mode resonant frequencies by Molin's formulas are plotted together. The gap resonant frequency is depend on the gap distance. In this case, the resonant frequency ranges from 0.45 rad/s to 0.6 rad/s, which is consistent with present berthing simulation results. The shape and frequency of gap resonance in side-by-side configuration can be found in Appendix A.



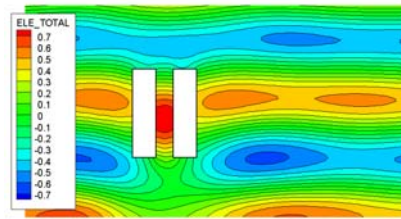
(a) $\lambda/L=0.5$, $\omega = 0.91$ rad/s



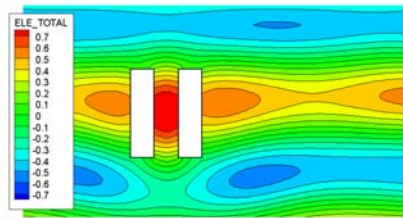
(b) $\lambda/L=0.667$, $\omega = 0.80$ rad/s



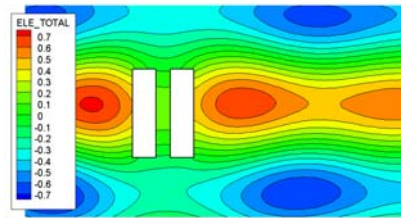
(c) $\lambda/L=1.0$, $\omega = 0.64$ rad/s



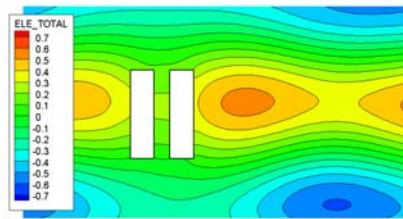
(d) $\lambda/L=1.333$, $\omega = 0.56$ rad/s



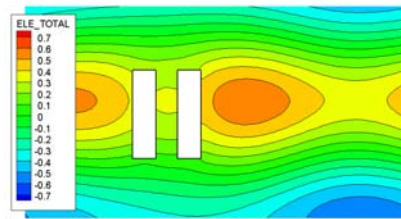
(e) $\lambda/L=1.667$, $\omega = 0.50$ rad/s



(f) $\lambda/L=2.0$, $\omega = 0.45$ rad/s



(g) $\lambda/L=2.333$, $\omega = 0.42$ rad/s



(h) $\lambda/L=2.667$, $\omega = 0.39$ rad/s

Fig. 4.6 Wave fields around the barges during the berthing operation under various wave frequencies (Heading 180°, H=1.0m, V=2.0 knots)

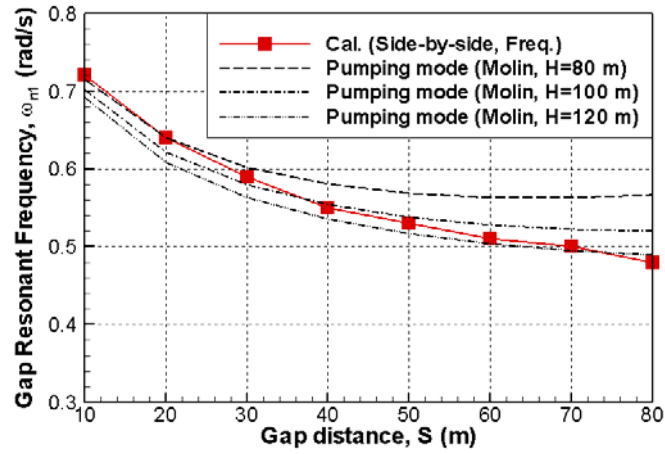
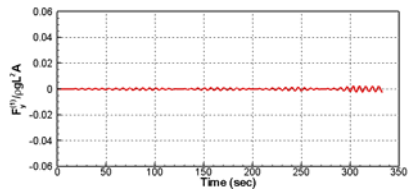


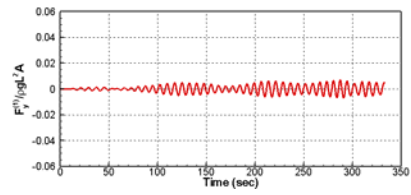
Fig. 4.7 Gap resonant frequency based on the side-by-side calculations by higher-order boundary element method in frequency domain

Fig. 4.8 shows the time series of first-order sway wave excitation force under the various regular wave conditions. As the two barges are approaching each other, the amplitude of sway force steadily increase. When the ratio of wave length and barge length ranges from 1.0 and 2.5, very strong sway excitation force occurs.

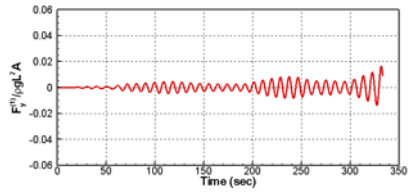
The time series of heave wave excitation forces acting on the transportation barge can be found in Fig. 4.9. As the wave length is getting longer, the heave excitation force tend to increase. When the wave length is twice of barge length, it is clearly observed the amplitude changes of heave excitation force.



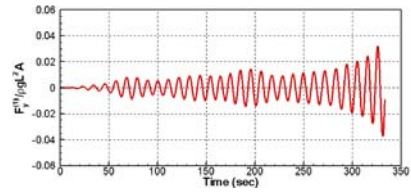
(a) $\lambda/L=0.5$, $\omega = 0.91$ rad/s



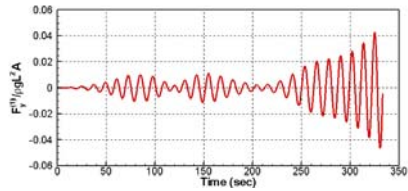
(b) $\lambda/L=0.667$, $\omega = 0.80$ rad/s



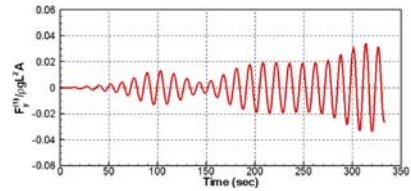
(c) $\lambda/L=1.0$, $\omega = 0.64$ rad/s



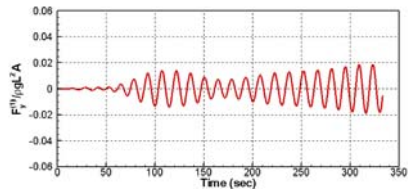
(d) $\lambda/L=1.333$, $\omega = 0.56$ rad/s



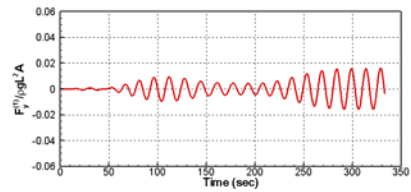
(e) $\lambda/L=1.667$, $\omega = 0.50$ rad/s



(f) $\lambda/L=2.0$, $\omega = 0.45$ rad/s

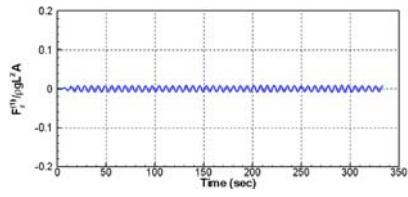


(g) $\lambda/L=2.333$, $\omega = 0.42$ rad/s

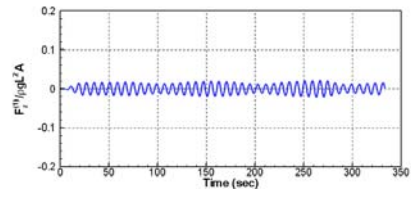


(h) $\lambda/L=2.667$, $\omega = 0.39$ rad/s

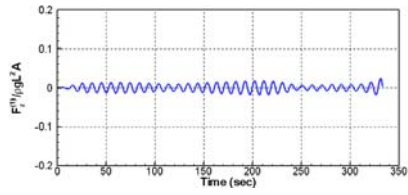
Fig. 4.8 First-order sway wave excitation forces acting on the transportation barge during the berthing operation under various regular wave conditions (Heading 180° , $H=1.0$ m, $V=2.0$ kts)



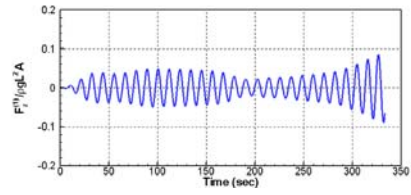
(a) $\lambda/L=0.5$, $\omega = 0.91$ rad/s



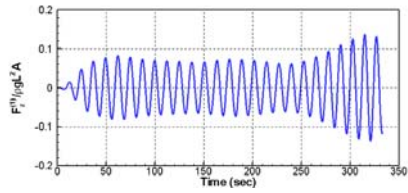
(b) $\lambda/L=0.667$, $\omega = 0.80$ rad/s



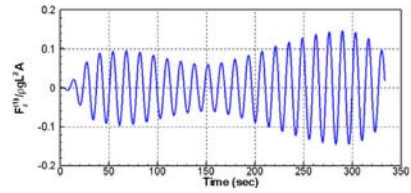
(c) $\lambda/L=1.0$, $\omega = 0.64$ rad/s



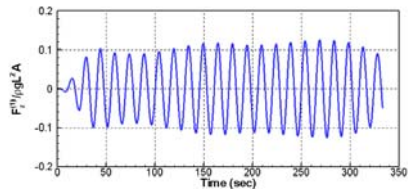
(d) $\lambda/L=1.333$, $\omega = 0.56$ rad/s



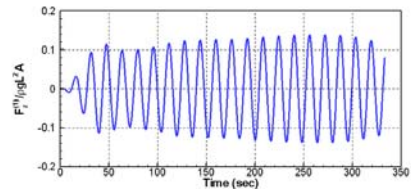
(e) $\lambda/L=1.667$, $\omega = 0.50$ rad/s



(f) $\lambda/L=2.0$, $\omega = 0.45$ rad/s



(g) $\lambda/L=2.333$, $\omega = 0.42$ rad/s

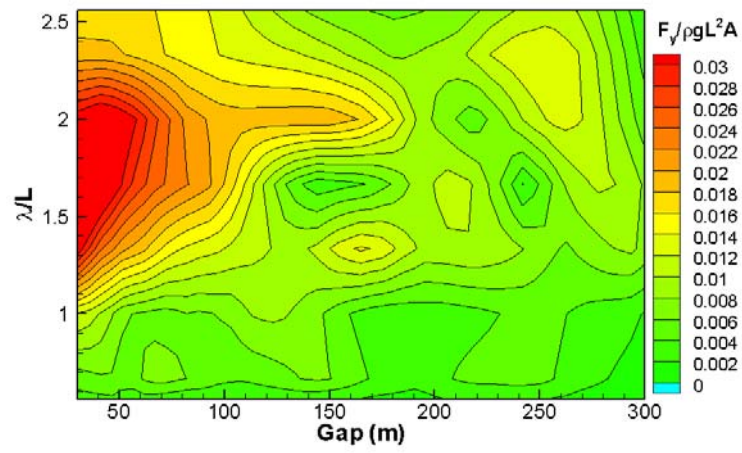


(h) $\lambda/L=2.667$, $\omega = 0.39$ rad/s

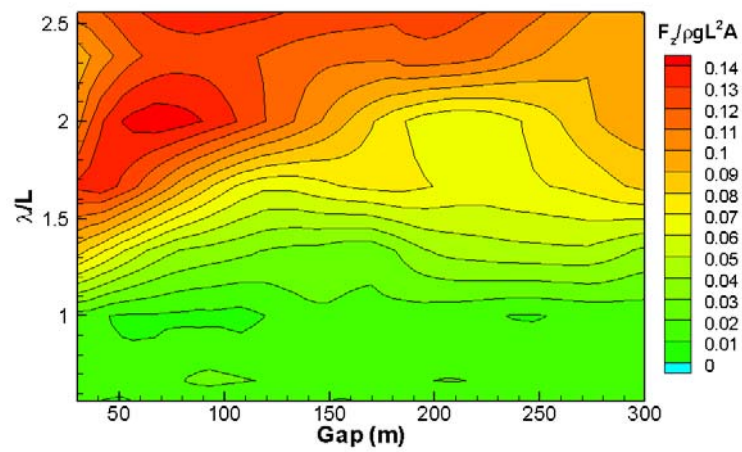
Fig. 4.9 First-order heave wave excitation forces acting on the transportation barge during the berthing operation under various regular wave conditions (Heading 180° , $H=1.0$ m, $V=2.0$ kts)

Fig. 4.10 shows the amplitude contours of the first-order wave excitation forces acting on the transportation barge during the berthing operation. The amplitude is extracted from the force time series by applying zero up-crossing method. From the force contour, it is clearly observed that the sway excitation force is highly localized in space and wave conditions. In other words, a strong sway force occurs only if the gap distance is less than 50 m and wavelengths are 1.5-2.0 times the barge length. These strong sway forces are caused by the gap resonant wave, shown in Fig. 4.6(d) and (e). On the contrary, the heave wave excitation force increases with the wavelength. Meanwhile, local maximum of heave force is observed when the wavelength is twice the barge length and the gap distance is about 80 m.

Fig. 4.11 shows the amplitude contours of the first-order roll and yaw moments acting on the transportation barge during berthing. Both moments also have highly localized characteristics, similar to the sway wave excitation force. While roll moment is maximized under the first longitudinal resonant condition, yawing moment reaches maximum value under the second longitudinal resonant condition, shown in Fig. 4.6(c). These force amplitude contours demonstrate that the lateral forces or moments under the head sea conditions are maximized if the two barges are close to each other and specific wave conditions are met.

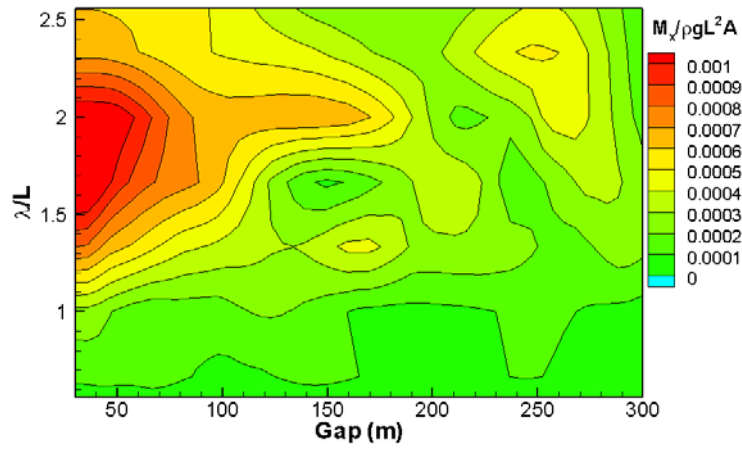


(a) Sway force amplitude contour

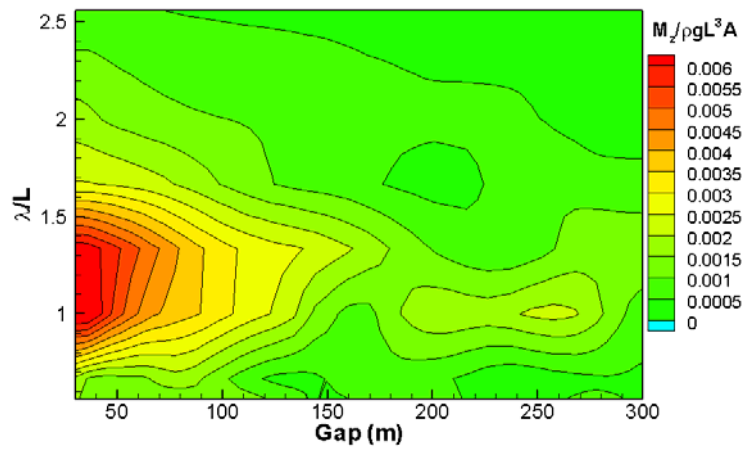


(b) Heave force amplitude contour

Fig. 4.10 Amplitude contours of first-order wave excitation forces acting on the transportation barge during the berthing operation (Heading 180°, H=1.0 m, V=2.0 kts)



(a) Roll moment amplitude contour

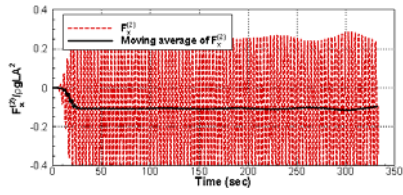


(b) Yaw moment amplitude contour

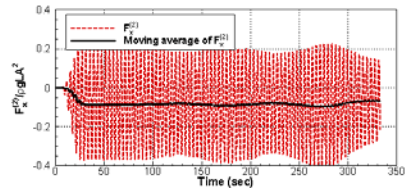
Fig. 4.11 Amplitude contours of first-order wave excitation moments acting on the transportation barge during the berthing operation (Heading 180°, H=1.0 m, V=2.0 kts)

Figs. 4.12 and 4.13 show the second-order surge and sway wave forces acting on the transportation barge during berthing under various wave conditions, respectively. While the second-order surge force increases with the decrease of wave length, the second-order sway force is only significant when the wavelength ratio is 1.0–2.0. The sway drift force increases steadily as the transportation barge approaches the installation barge closely. After 250 s, it can be seen that the sway drift force sharply increases because of the gap resonance.

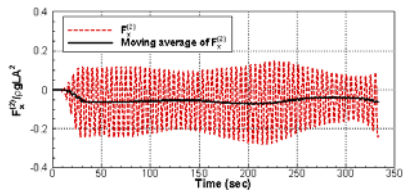
Fig. 4.14 shows the surge and sway drift force contours during berthing. Similar to the lateral wave excitation force, the sway drift force is also highly localized. The maximum sway drift force occurs when the wavelength is about 1.5 times of the barge length and the gap distance is less than 50 m. At this time, a strong repulsive drift force resists the approaching of the transportation barge.



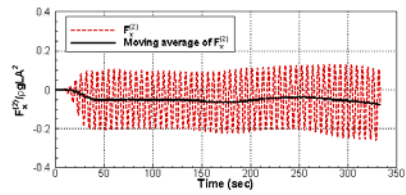
(a) $\lambda/L=0.5$, $\omega = 0.91$ rad/s



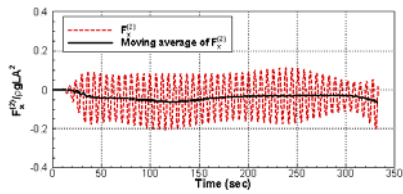
(b) $\lambda/L=0.667$, $\omega = 0.80$ rad/s



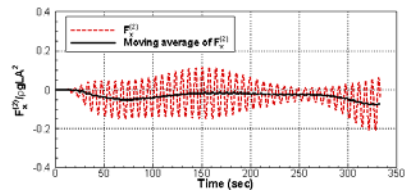
(c) $\lambda/L=1.0$, $\omega = 0.64$ rad/s



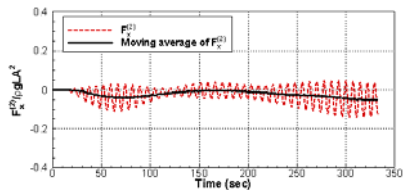
(d) $\lambda/L=1.333$, $\omega = 0.56$ rad/s



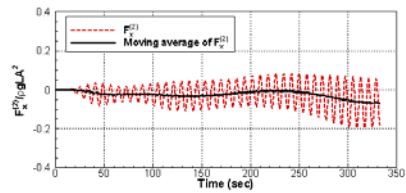
(e) $\lambda/L=1.667$, $\omega = 0.50$ rad/s



(f) $\lambda/L=2.0$, $\omega = 0.45$ rad/s

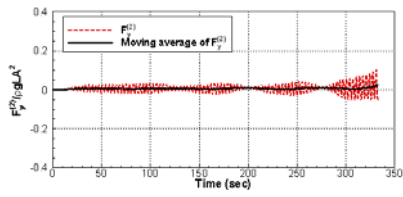


(g) $\lambda/L=2.333$, $\omega = 0.42$ rad/s

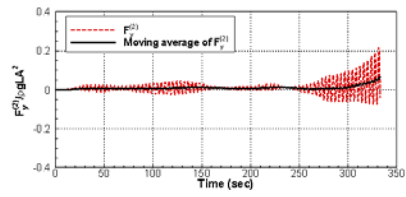


(h) $\lambda/L=2.667$, $\omega = 0.39$ rad/s

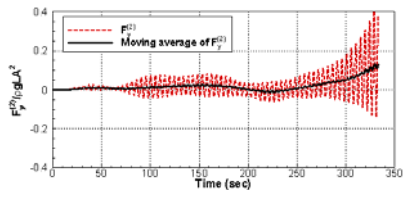
Fig. 4.12 Second-order surge wave forces acting on the transportation barge during the berthing operation under various regular wave conditions (Heading 180° , $H=1.0\text{m}$, $V=2.0$ knots)



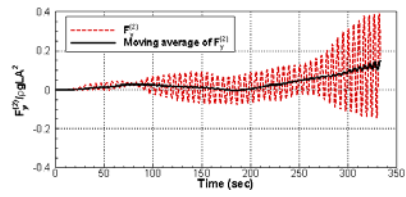
(a) $\lambda/L=0.5$, $\omega = 0.91$ rad/s



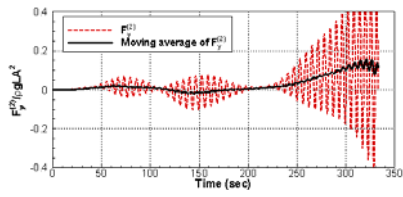
(b) $\lambda/L=0.667$, $\omega = 0.80$ rad/s



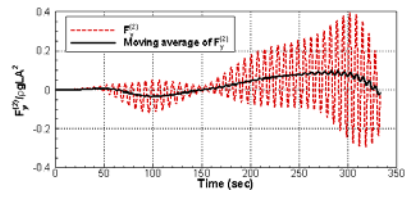
(c) $\lambda/L=1.0$, $\omega = 0.64$ rad/s



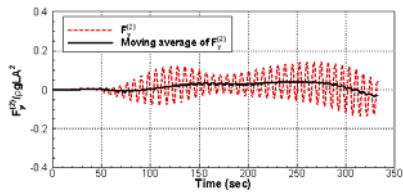
(d) $\lambda/L=1.333$, $\omega = 0.56$ rad/s



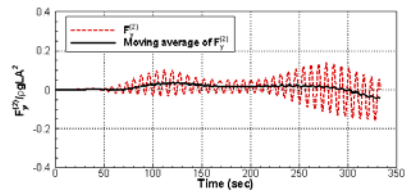
(e) $\lambda/L=1.667$, $\omega = 0.50$ rad/s



(f) $\lambda/L=2.0$, $\omega = 0.45$ rad/s

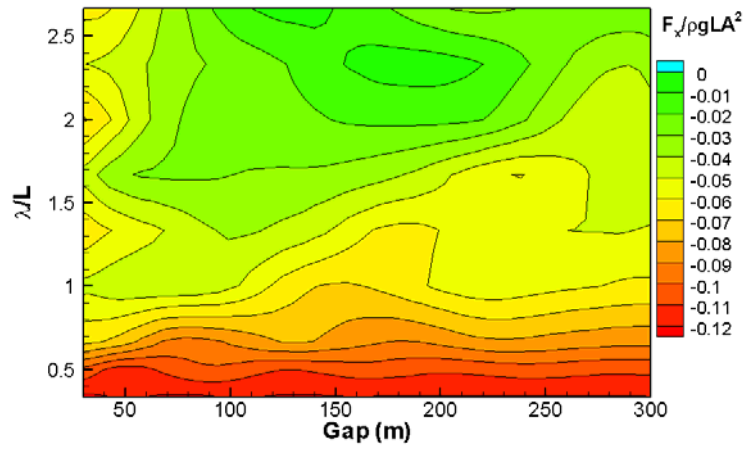


(g) $\lambda/L=2.333$, $\omega = 0.42$ rad/s

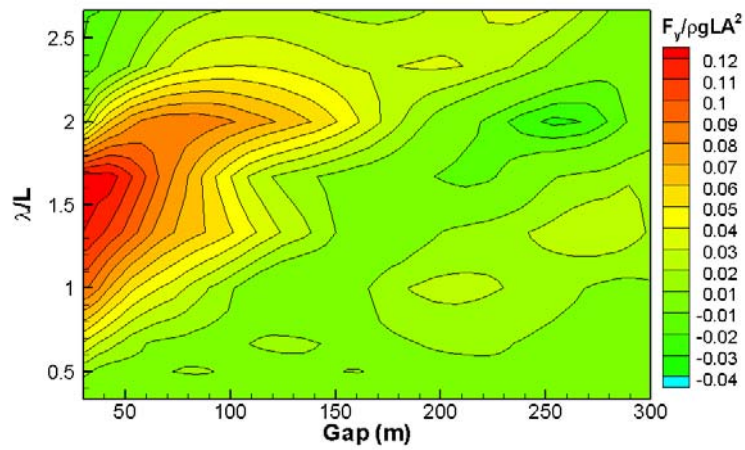


(h) $\lambda/L=2.667$, $\omega = 0.39$ rad/s

Fig. 4.13 Second-order sway wave forces acting on the transportation barge during the berthing operation under various regular wave conditions (Heading 180° , $H=1.0\text{m}$, $V=2.0$ knots)



(a) Surge drift force



(b) Sway drift force

Fig. 4.14 Second-order drift force contours of the transportation barge during the berthing operation under various regular wave conditions (Heading 180° , $H=1.0\text{m}$, $V=2.0$ knots)

4.4 Effect of wave heading

4.4.1 Berthing in beam sea

Fig. 4.15 shows the snapshots of wave fields during berthing when the wave heading is 90° . In this simulation, the wavelength is same as the barge length. Wave height and berthing speed are 1 m and 2 knots, respectively. Since the starboard sides of the two vessels are exactly normal to the incident wave, a strong reflection is observed on the starboard side of the barges. As the transportation barge approaches the installation barge, the former enters the sheltering zone behind the latter. Thus, the wave elevation around the transportation barge becomes quite low after 150 s. This indicates that the transportation barge may experience less wave loads due to the sheltering effect if the wave heading and berthing direction is opposite. Meanwhile, high reflected waves are retained on the starboard side of the installation barge during whole berthing time. Contrary to the head sea case, the gap flow between the two barges is not significant under the beam sea condition.

When the wave heading is 270° , the wave fields are as shown in Fig. 4.16. Simulation condition is same as the previous case. From the figures, it can be seen that the transportation barge is directly exposed to the incident wave during berthing. In this case, high reflected waves are observed on the portside of the transportation barge. As the two barges approach each other, installation barge is located in the sheltering zone by the transportation barge.

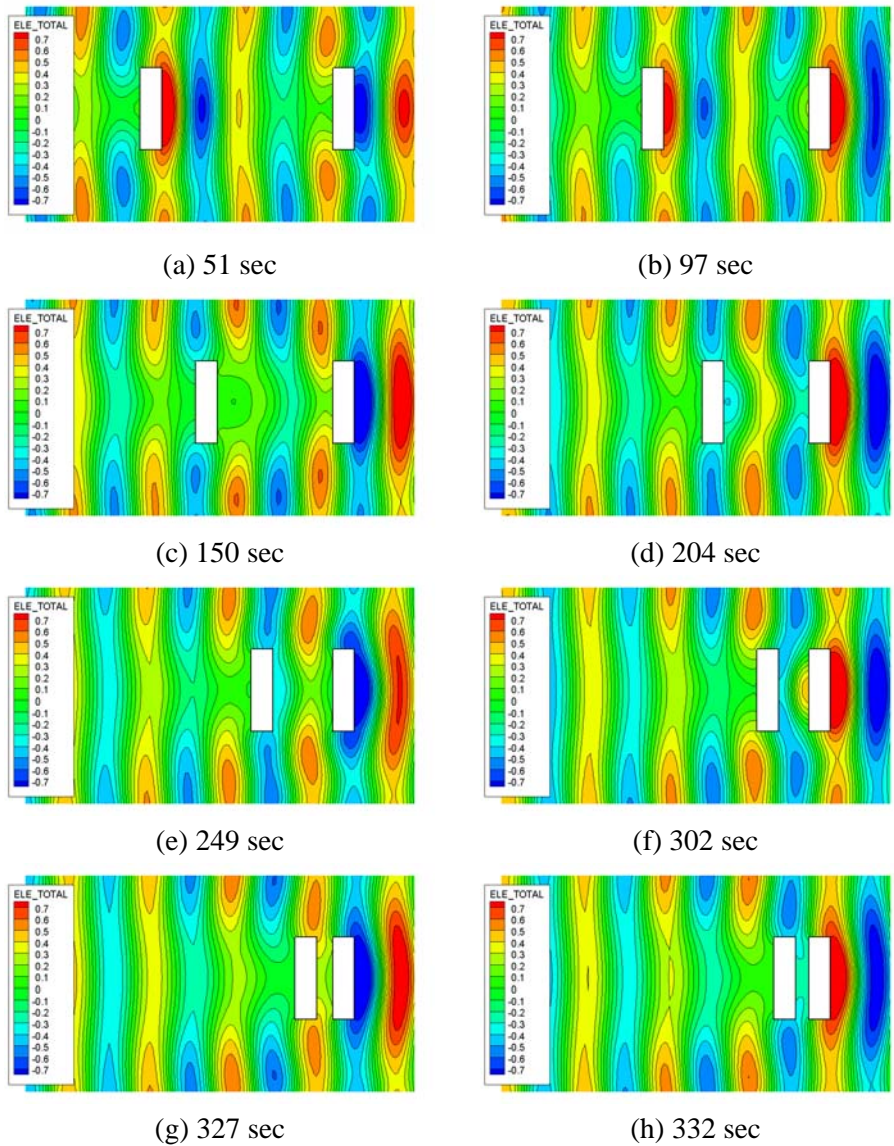


Fig. 4.15 Wave fields around the barges during the berthing operation in beam sea (Heading 90° , $\lambda/L=1.0$, $H=1.0$ m, $V=2.0$ kts)

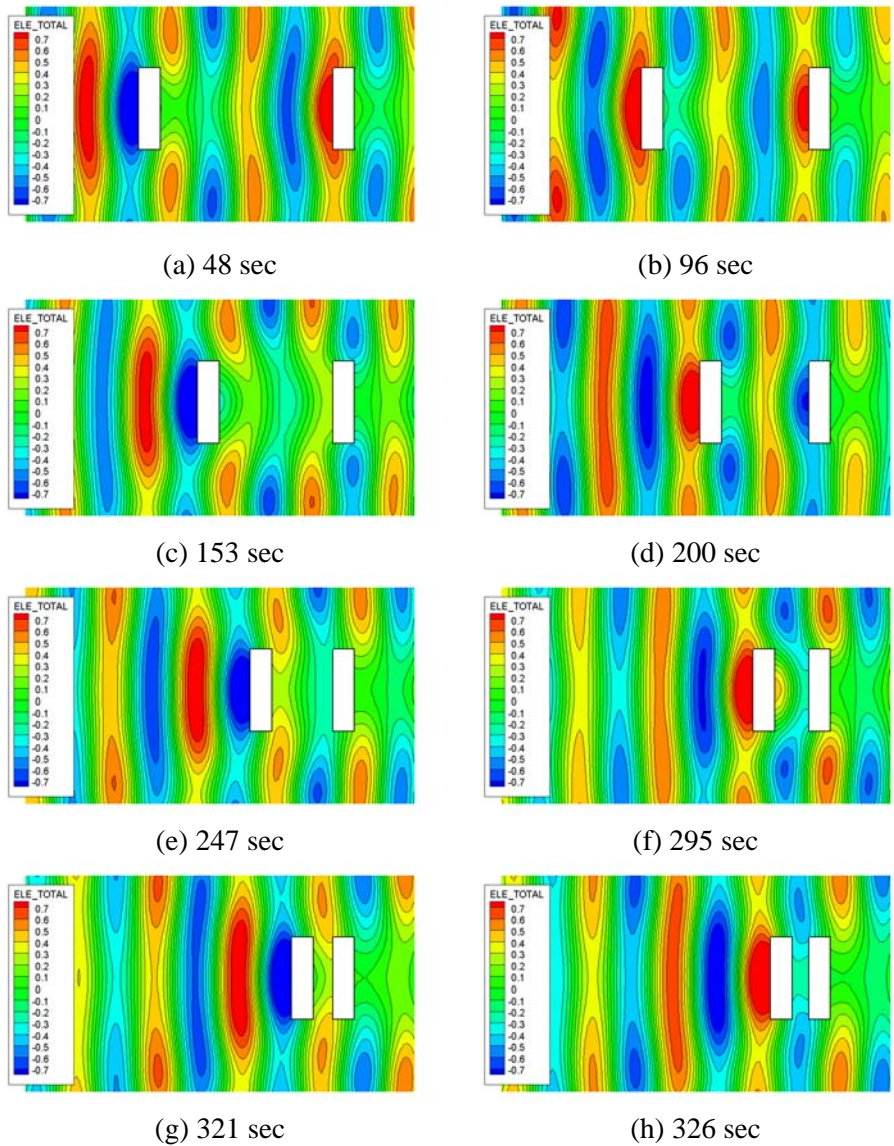
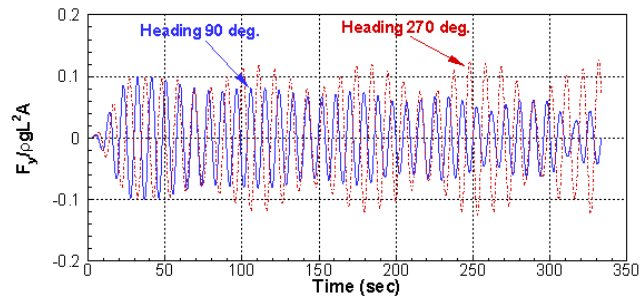
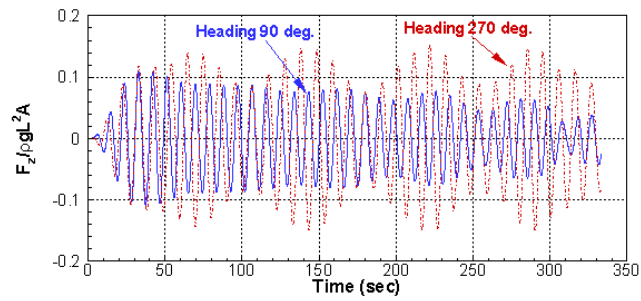


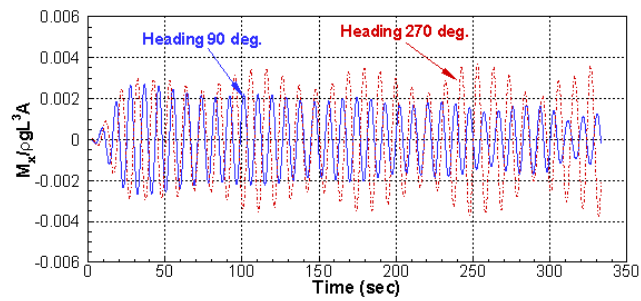
Fig. 4.16 Wave fields around the barges during the berthing operation in beam sea (Heading 270°, $\lambda/L=1.0$, $H=1.0$ m, $V=2.0$ kts)



(a) F_y



(b) F_z



(c) M_x

Fig. 4.17 Comparison of first-order wave excitation forces acting on the barges in beam sea ($\lambda/L=1.0$, $H=1.0$ m, $V=2.0$ kts)

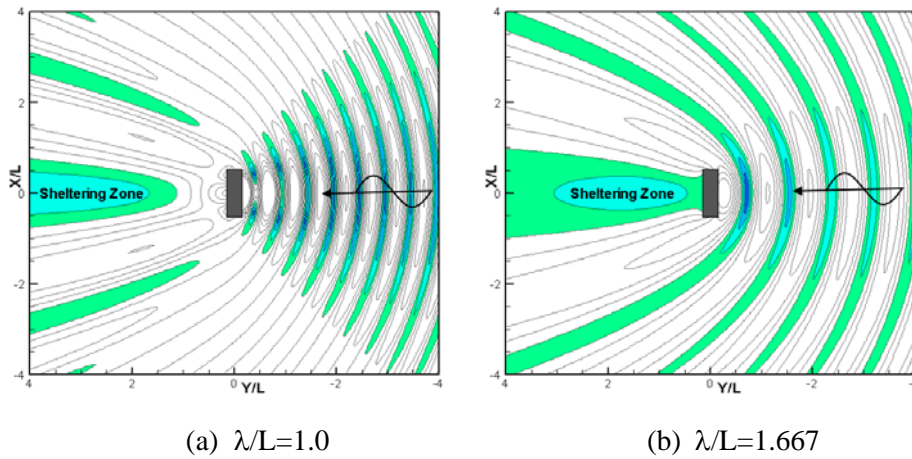


Fig. 4.18 Shielding zone around single barge in beam sea based on the frequency-domain solutions (Heading 90°)

Fig. 4.17 compares the first-order force time series between the headings of 90° and 270° . As the transportation barge approaches the installation barge with a wave heading of 90° , the wave force decreases continuously due to the sheltering effect. A floating body on the weather side of a particular body acts as a breakwater. When a berthing barge approaches through an area behind the lee side of a stationary structure, the barge is subjected to reduced hydrodynamic force owing to the sheltering effect of the stationary structure. Fig. 4.18 shows the sheltering zone around a barge under the beam sea conditions. This figure is based on the frequency-domain solutions by higher-order boundary element method. In this figure, the sheltering zone is defined as the area in which the wave amplitude is less than 80 % of incident wave amplitude. The sheltering zone is mainly located in the leeside of the barge as expected. In addition, it can be seen that the size and location of the sheltering

zone depend on the wave frequency. When the transportation barge is approaching within the sheltering zone, the required thrust power for berthing operation can be reduced because of the decrease of wave force, as shown in Fig. 4.17. It is worthy to note that sheltering zone becomes wider if the two barges are located closely. More details for sheltering zone can be found in Appendix C.

When the wave heading is 270° , high modulated forces are retained during the berthing operation, shown in Fig. 4.17. These amplitude modulation are caused by two different force components of close encounter frequencies, given in Eq. (4.2) and (4.3).

$$\omega_{e1} = \omega - Uk \cos \beta \quad (4.2)$$

$$\omega_{e2} = \omega + Uk \cos \beta \quad (4.3)$$

The first frequency component is produced when the moving transportation barge encounters the incident wave. Since the berthing direction is same as the incident wave direction, this encounter frequency becomes lower than incident wave frequency. The second component is generated when the transportation barge encounters the reflected wave from installation barge. In this case, encounter frequency is slightly higher than incident wave frequency. Fig. 4.19 depicts the two encounter frequencies that the transportation barge experiences under the beam sea conditions. Fig. 4.20 shows Fast Fourier Transform (FFT) results of the sway wave excitation force acting on the transportation barge in beam sea. Two dominant

components of encounter frequencies, ω_{e1} and ω_{e2} , are clearly observed.

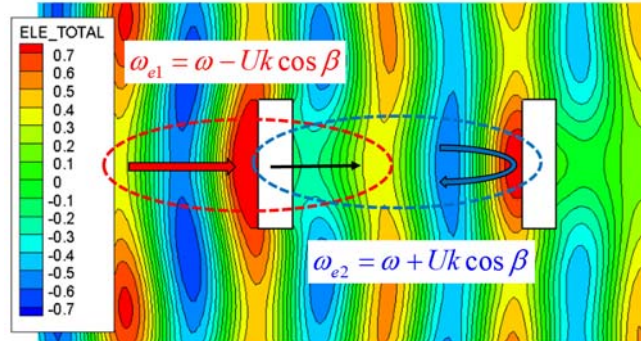
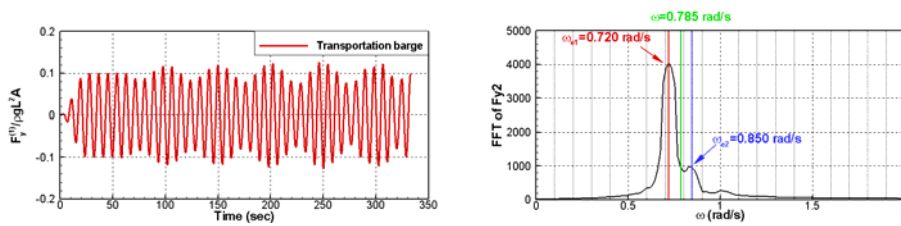
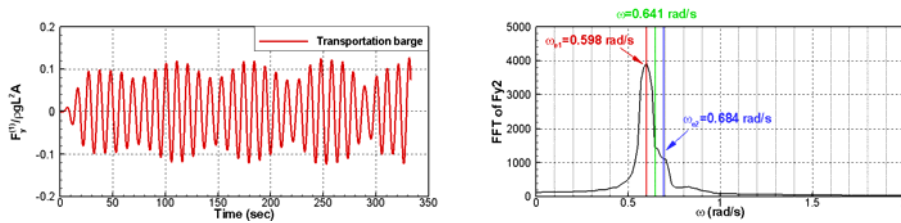


Fig. 4.19 Encounter frequencies of the transportation barge in beam sea
(Heading 270° , $\lambda/L=1.0$, $H=1.0$ m, $V=2.0$ knots)

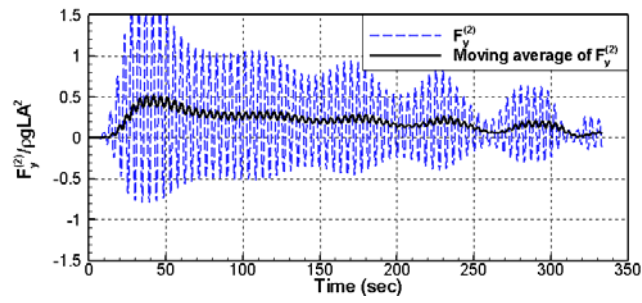


(a) $\lambda/L=0.667$

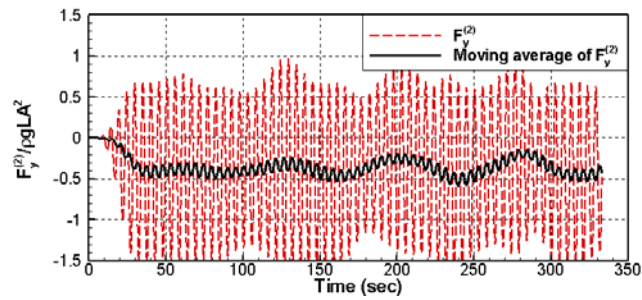


(b) $\lambda/L=1.0$

Fig. 4.20 FFT results of sway wave excitation force acting on the transportation barge (Heading 270° , $H=1.0$ m, $V=2.0$ knots)



(b) Heading 90 deg.



(c) Heading 270 deg.

Fig. 4.21 Comparison of second-order sway wave excitation forces acting on the barges in beam sea ($\lambda/L=1.0$, $H=1.0\text{m}$, $V=2.0$ knots)

The second-order force time series demonstrates the sheltering effect more clearly, as shown in Fig. 4.21. With a heading of 90° , the second-order sway force decreases steadily during the berthing operation. The sway drift force also decreases as the two barges approach each other.

4.4.2 Berthing in quartering sea

In a quartering sea, the incident wave is partially blocked by the vessel on the weather side. When the wave heading is 135° , the transportation barge is approaching near the lee side of the installation vessel, as shown in Fig. 4.22. During berthing, there are strong reflection waves around the starboard sides of the two vessels. After 300 s, the transportation barge is sheltered by the installation vessel, which results in decrease of the lateral force.

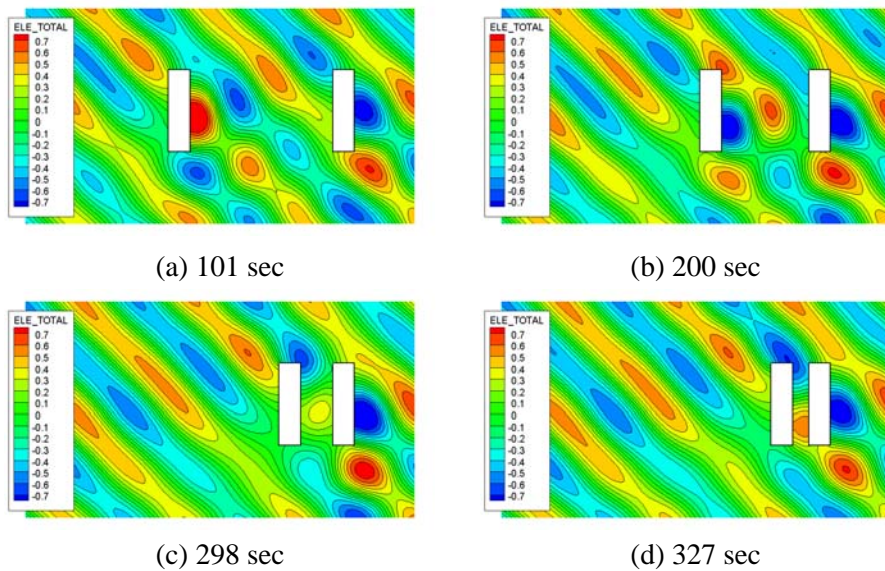


Fig. 4.22 Wave fields around the barges during the berthing operation in quartering sea (Heading 135° , $\lambda/L=1.0$, $H=1.0$ m, $V=2.0$ kts)

Fig. 4.23 shows the wave fields when the wave heading is 225° . In this case, the port sides of the two barges are directly exposed to the incident waves. A

strong reflection occurs on the port sides of the two barges. Compared to the head sea case, the gap flow is not significant.

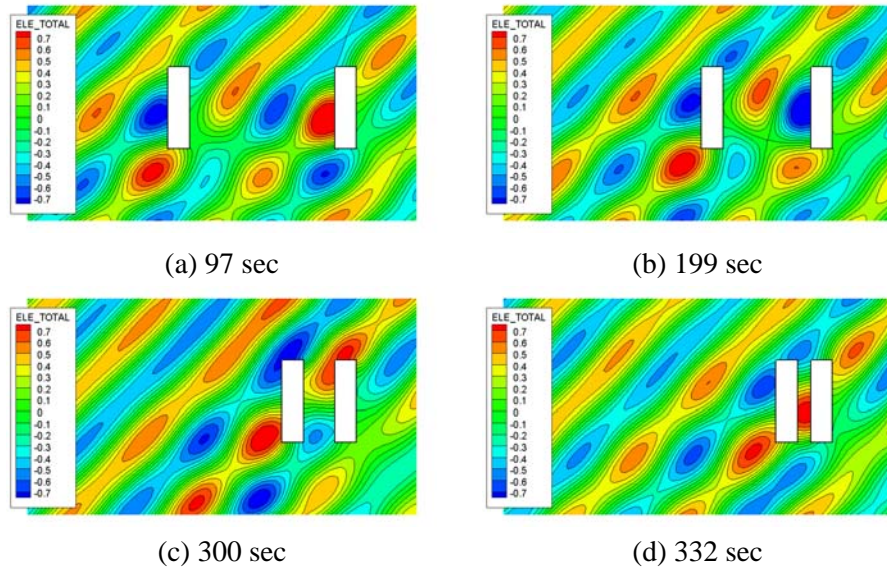


Fig. 4.23 Wave fields around the barges during the berthing operation in quartering sea (Heading 225° , $\lambda/L=1.0$, $H=1.0$ m, $V=2.0$ kts)

Fig. 4.24 compares the force time series during berthing in the bow quartering sea at the two headings. A highly modulated force occurs when the wave heading is 225° . These amplitude modulations are caused by the combination of two wave components with different encounter frequencies. For example, the sway wave excitation force shows a local increase at 150, 230, and 300 s. The roll excitation moment also increases at the same times. Similarly, the heave excitation force shows local maxima at 100, 190, and 180 s. The sway wave excitation force decreases when the heave excitation force increases. This result was closely related to the gap wave characteristics.

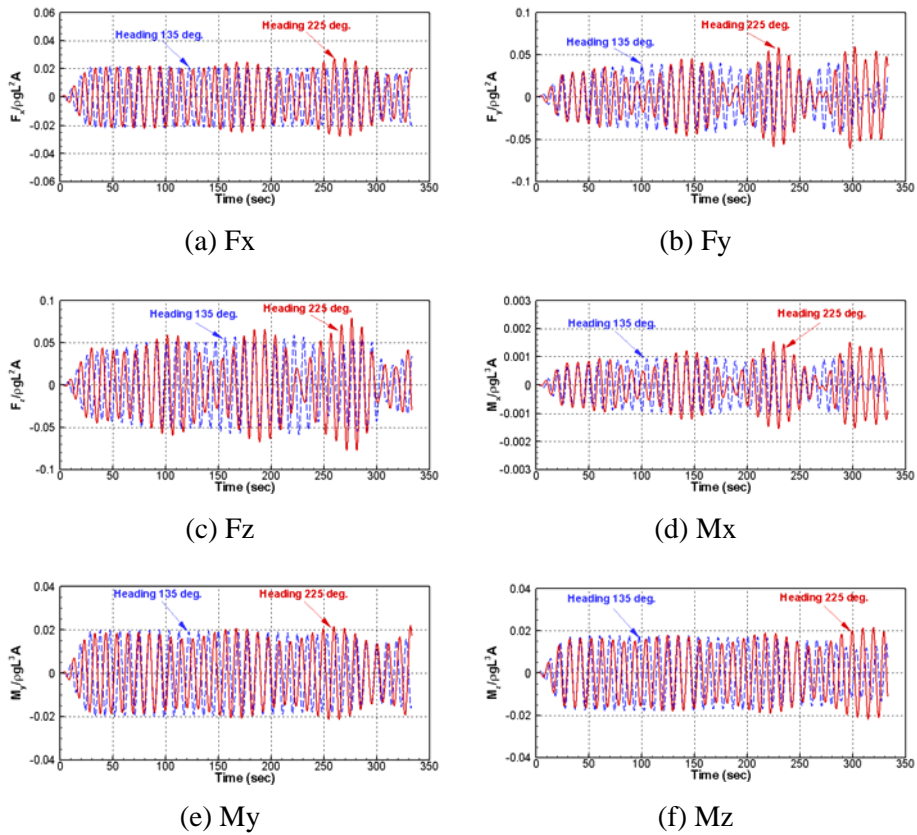
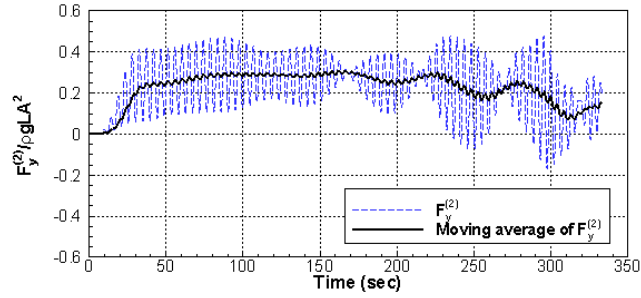


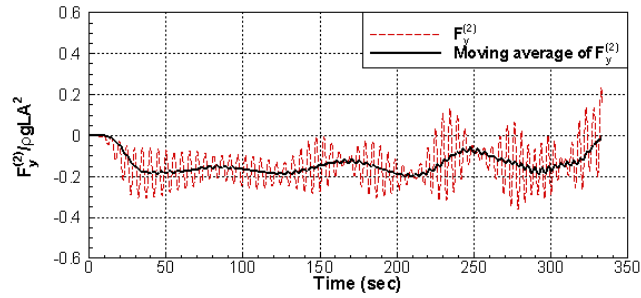
Fig. 4.24 Comparison of the first-order wave excitation forces acting on the barges in quartering sea ($\lambda/L=1.0$, $H=1.0$ m, $V=2.0$ kts)

Fig. 4.25 shows the second-order sway forces acting on the transportation barge. When the wave heading is 135° , a strong sway drift force resists the approach of the transportation barge. In this case, more thrust can be required during berthing. Meanwhile, an assisting drift force is acting on the transportation barge during berthing when the wave heading is 225° . This drift

force pushes the transportation barge in the direction of the berthing. After 300 s, the drift forces in the quartering sea decrease.



(b) Heading 135 deg.



(c) Heading 225 deg.

Fig. 4.25 Second-order sway forces acting on the transportation barge during the berthing operation in quartering sea ($\lambda/L=1.0$, $H=1.0\text{m}$, $V=2.0$ kts)

4.5 Comparison with experiments

4.5.1 Model test

Model tests for berthing problem between two barges were carried out to validate the present calculation results. The experiment was performed in Ocean Engineering Basin (OEB) of KRISO. The experimental models with 1/50 scale ratio were made of wood for the two identical barges of 150 m (L) \times 40 m (B) \times 10 m (D). A load-cell was attached to the transportation barge model to measure the hydrodynamic forces during berthing. Fig. 4.26 shows model test set-up for the present berthing experiment.

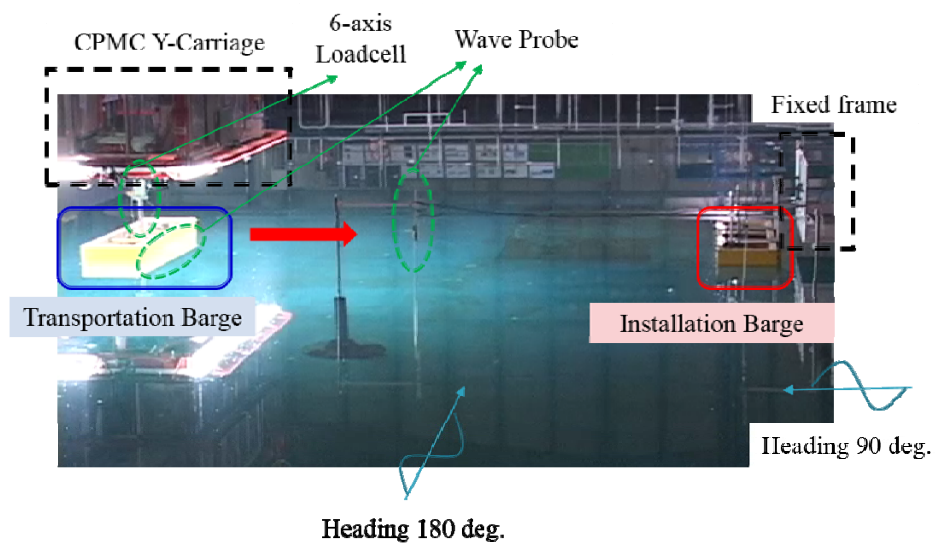


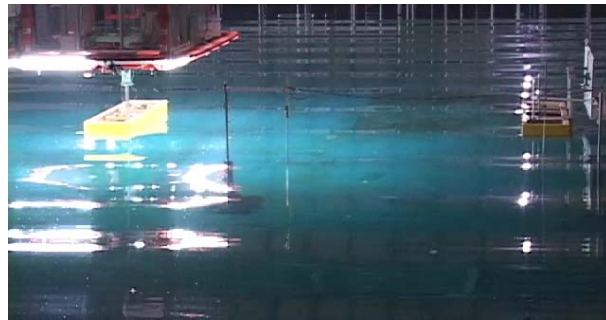
Fig. 4.26 Model test set-up for berthing experiment between two barges

In the berthing test, the transportation barge, which is attached to the Y-carriage of CPMC (Computerized Planar Motion Carriage), approaches the installation barge with constant berthing speed from 400 to 12.5m distance. During the berthing operation, hydrodynamic force and wave elevation were measured.

4.7.2 Berthing in head sea

Fig. 4.27 shows snapshots of berthing test at three different gap distance ('S') when the wave heading is 180 degree and wavelength is 250m. It can be seen that the transportation barge approaches the installation barge under the regular wave condition. Fig. 4.28 shows gap flow when the transportation barge is closely located near the installation barge.

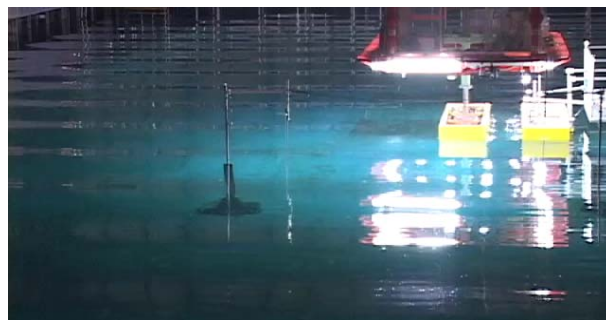
Fig. 4.29 shows the direct comparison of sway force time series between experiments and calculations. X-axis is set to gap distance for the comparison of the spatial characteristics of the wave forces. At $\lambda/L=1.667$ and $\lambda/L=2.0$, the agreements between experiments and calculations are quite good. In particular, sharp increasing trend due to gap resonance is clearly observed both in experimental data and numerical results at the small gap distance less than 50 m. At $\lambda/L=1.333$, experiments shows larger sway force with strong amplitude modulation compared to the calculations. This discrepancy is partially attributed to the wall effect from the limited basin width. The reflected wave from the side wall of the basin may change the sway force acting on the barge.



(a) $S=334$ m



(b) $S=101$ m



(c) $S=21$ m

Fig. 4.27 Snapshots of berthing model test in regular waves
(Heading 180° , $\lambda/L=1.667$, $H=1.0$ m, $V=2.0$ kts)

Fig. 4.30 shows comparison of the time series of yawing moments acting on

the transportation barge between experiments and present calculations. Similar to the sway wave force, discrepancy between experiment and calculations is observed at $\lambda/L=1.333$. It can be understood that the reflected wave from the side wall of the basin increases the yawing moments acting on the transportation barge. At $\lambda/L=1.667$ and $\lambda/L=2.0$, experiment data shows larger moments rather than the calculations. Nevertheless, the overall trend of the moment amplitude from calculation is quite similar to that of experiments.



(a) S=91m



(b) S=54m

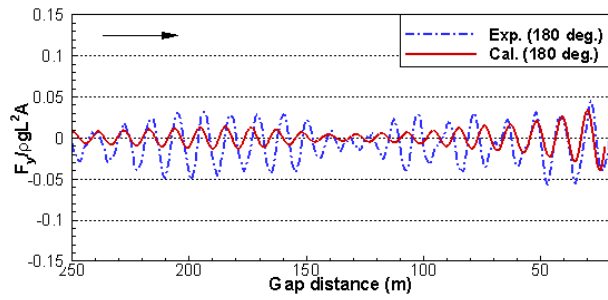


(c) S=25m

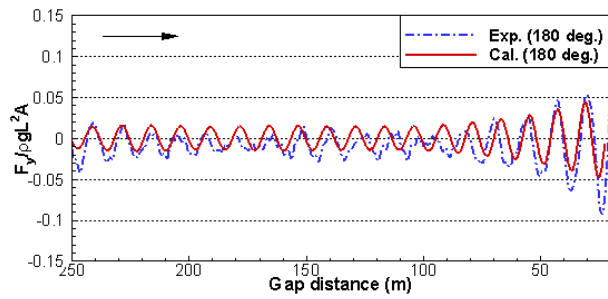


(d) S=12.5m

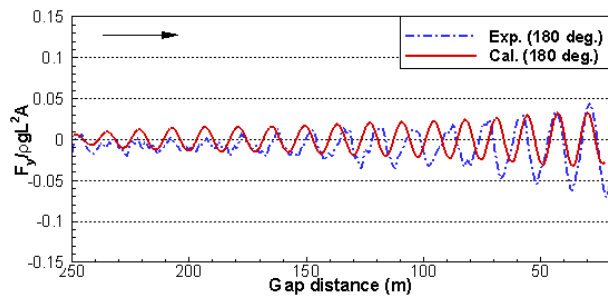
Fig. 4.28 Snapshots of gap flow during berthing model test in head sea ($\lambda/L=1.667$, $H=1.0$ m, $V=2.0$ kts)



(a) $\lambda/L=1.333$

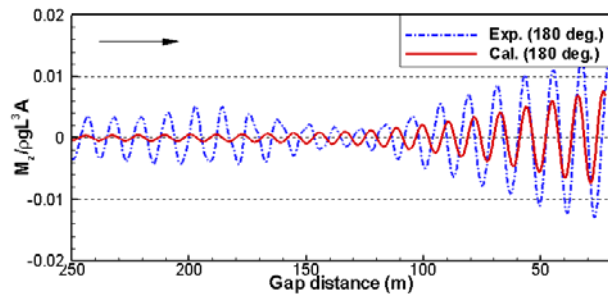


(b) $\lambda/L=1.667$

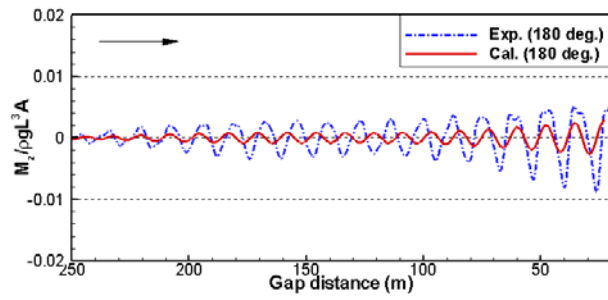


(c) $\lambda/L=2.0$

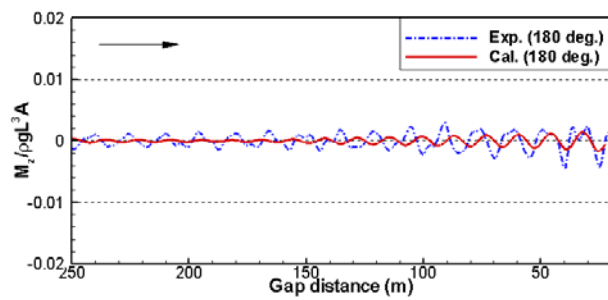
Fig. 4.29 Comparison of sway wave forces acting on the transportation barge during the berthing model test in head sea ($H=1.0$ m, $V=2.0$ kts)



(a) $\lambda/L=1.333$



(b) $\lambda/L=1.667$



(c) $\lambda/L=2.0$

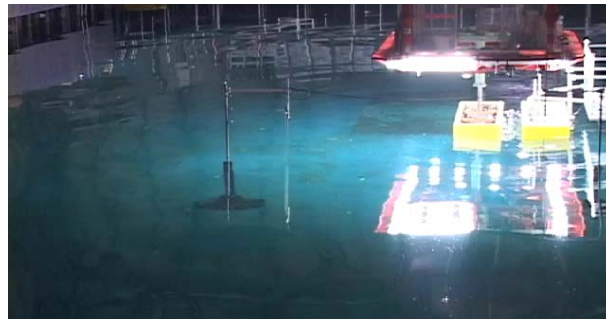
Fig. 4.30 Comparison of yawing moments acting on the transportation barge during the berthing model test in head sea ($H=1.0$ m, $V=2.0$ kts)

4.7.2 Berthing in beam sea

Fig. 4.31 shows the two snapshots of berthing test when the wave heading is 90° and wavelength is 250m. In this case, the transportation barge enters the sheltering zone by the installation barge during berthing. Fig. 4.32 shows gap flow when the transportation barge is closely located near the installation barge. Violent gap waves are observed compared to the head sea case.



(b) $S=160$ m



(c) $S=12.5$ m

Fig. 4.31 Snapshots of berthing model test in regular waves
(Heading 90° , $\lambda/L=1.667$, $H=1.0$ m, $V=2.0$ kts)

Fig. 4.33 shows the comparison of sway wave force acting on the transportation barges between experiments and calculations under 6 different wave frequencies. At $\lambda/L=1.0$ and $\lambda/L=1.333$, agreement between experiments and calculations is fairly good. Increasing and decreasing behavior of sway force with respect to the gap distance is quite similar between experiments and calculations. In this case, strong amplitude modulations are retained for all berthing process. For the other wave frequencies, experiments and calculations agree well.



(a) S=87 m



(b) S=65 m

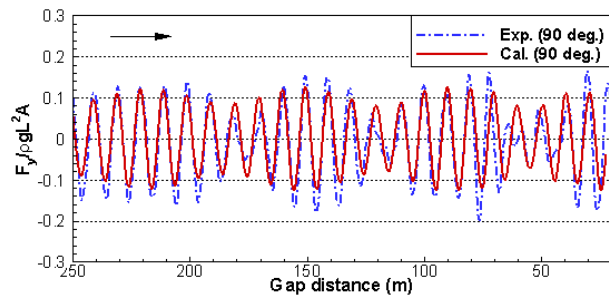


(c) S=51 m

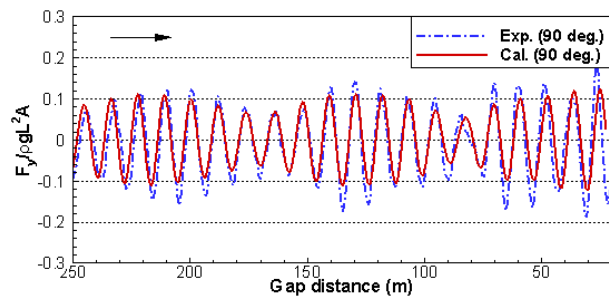


(d) S=36 m

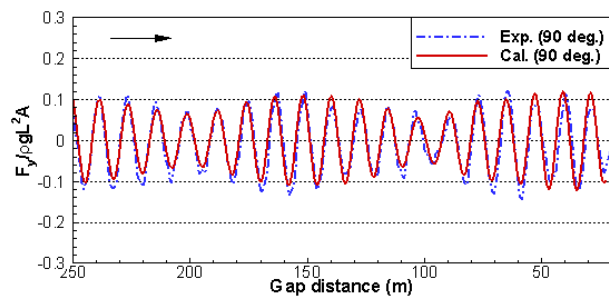
Fig. 4.32 Snapshots of gap flow during berthing model test in beam sea
($\lambda/L=1.667$, $H=1.0\text{m}$, $V=2.0$ kts)



(a) $\lambda/L=1.0$

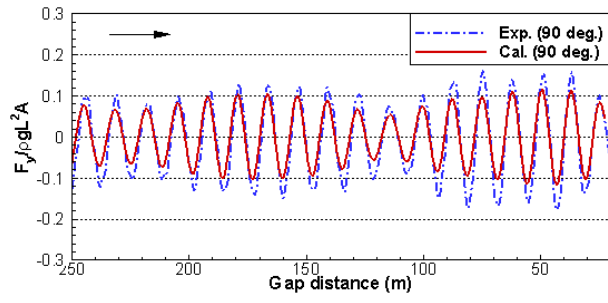


(b) $\lambda/L=1.333$

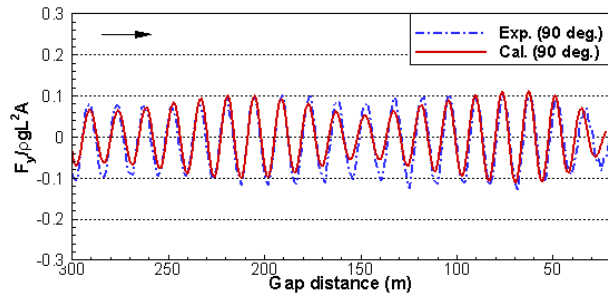


(c) $\lambda/L=1.5$

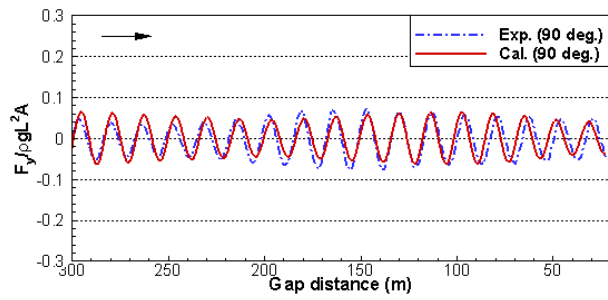
Fig. 4.33 Comparison of sway wave forces acting on the transportation barge between experiments and calculations in beam sea ($H=1.0$ m, $V=2.0$ kts)



(d) $\lambda/L=1.667$



(e) $\lambda/L=2.0$



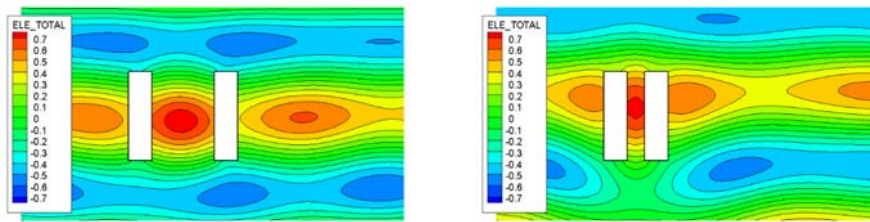
(f) $\lambda/L=2.667$

Fig. 4.33 Continued

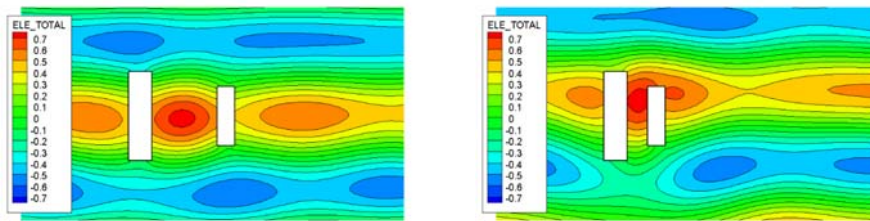
4.5 Effect of barge size

Hydrodynamic force during the berthing operation is greatly affected by the size of barges. In this study, four different transportation barges are considered to investigate the effect of barge size. For all cases, the installation barge is assumed the same. Fig. 4.34 shows the wave fields during the berthing operation with four different transportation barges in head sea. When the transportation barge is of the same size as the installation barge, the highest wave elevation appears in the gap region. As the transportation barge is getting smaller, the disturbed wave from the transportation barge is getting weaker. It can be seen that the gap flow between the barges also reduced.

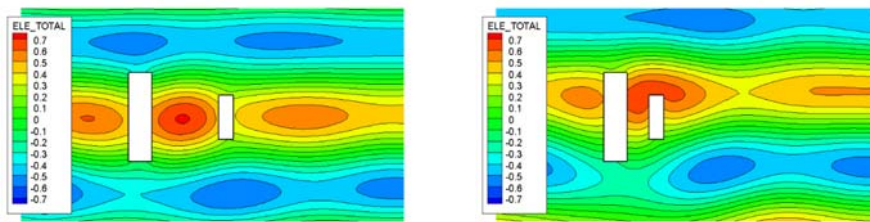
Fig. 4.35 shows the time series of sway wave excitation forces acting on the transportation barge during the berthing operation with four different transportation barges. The force is non-dimensionalized using the length of the installation barge. When the two barges are identical, the strongest sway excitation forces are observed. As the transportation barge is getting smaller, the sway wave excitation forces acting on the two barges also decrease. In particular, significant decrease can be found in the sway force when ‘barge 3’ is used as the transportation barge. This means that the interaction effect between the two barges is strongly affected by the size of the transportation barge. Fig. 4.36 shows the time series of second-order sway wave forces during the berthing operation. Similar to the first-order wave force, the smaller transportation barge results in the smaller second-order sway wave force.



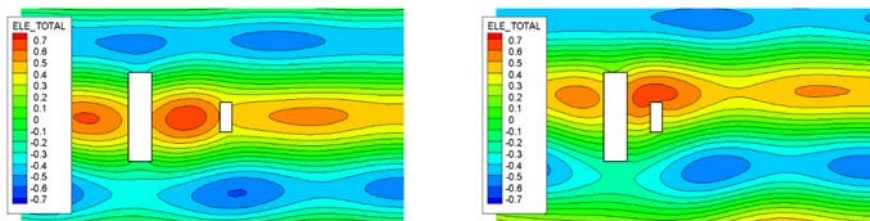
(a) Barge 1 (150 m) and barge 1 (150 m)



(b) Barge 1 (150 m) and barge 2 (100 m)

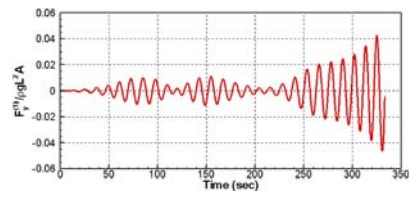
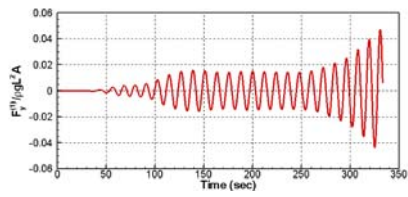


(c) Barge 1 (150 m) and barge 3 (75 m)

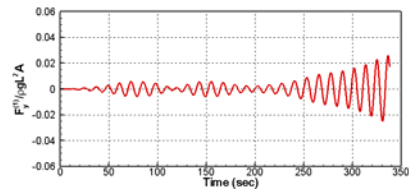
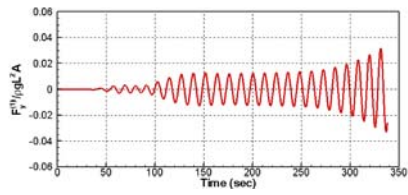


(d) Barge 1 (150 m) and barge 4 (50 m)

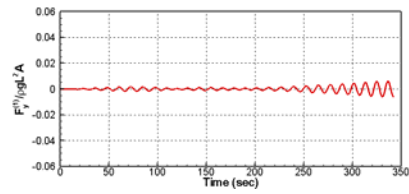
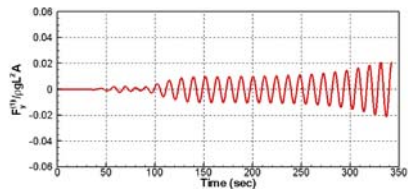
Fig. 4.34 Wave fields during the berthing operation with various barge dimensions in head sea ($\lambda/L=1.667$, $H=1.0$ m, $V=2.0$ kts)



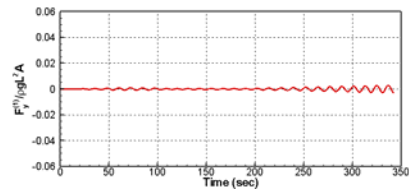
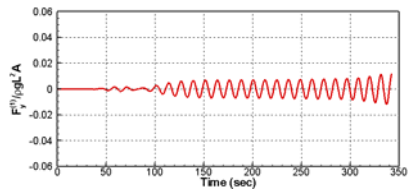
(a) Barge 1 (150 m) and barge 1 (150 m)



(b) Barge 1 (150 m) and barge 2 (100 m)

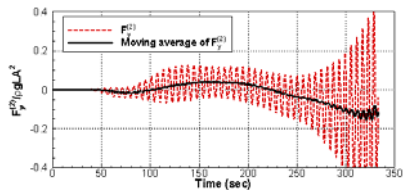


(c) Barge 1 (150 m) and barge 3 (75 m)

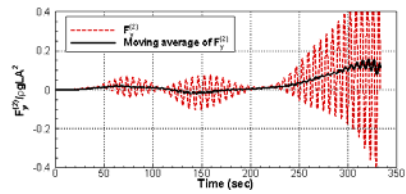


(d) Barge 1 (150 m) and barge 4 (50 m)

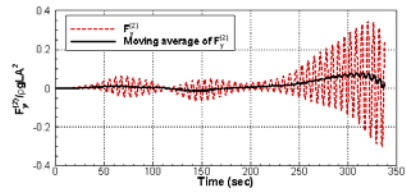
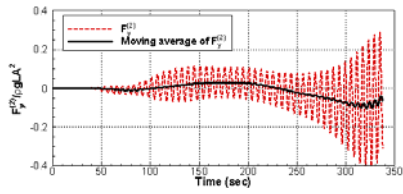
Fig. 4.35 First-order sway wave excitation forces acting on the barges during the berthing operation with various barge dimensions in head sea ($\lambda/L=1.667$, $H=1.0$ m, $V=2.0$ kts)



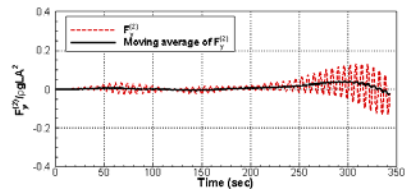
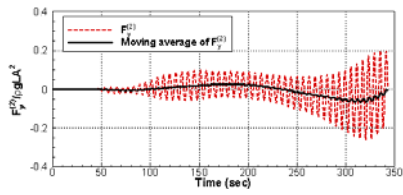
(a) Barge 1 (150 m) and barge 1 (150 m)



(b) Barge 1 (150 m) and barge 2 (100 m)



(c) Barge 1 (150 m) and barge 3 (75 m)



(d) Barge 1 (150 m) and barge 4 (50 m)

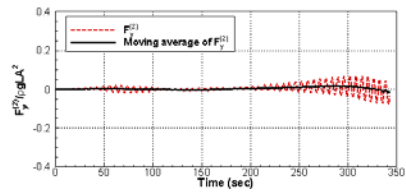
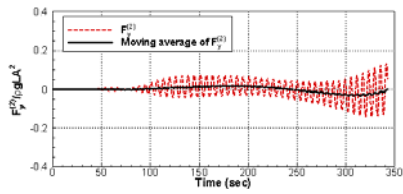
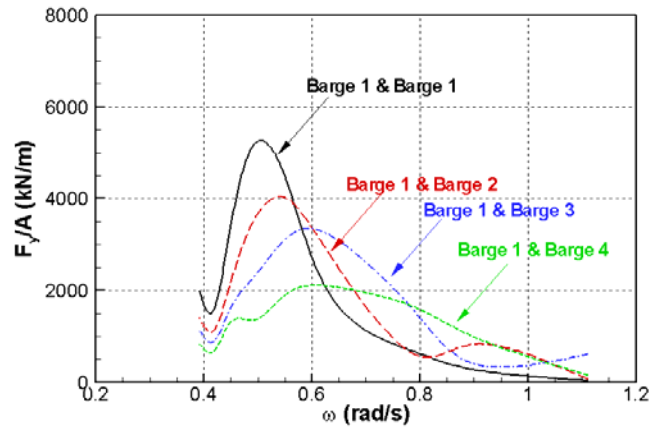
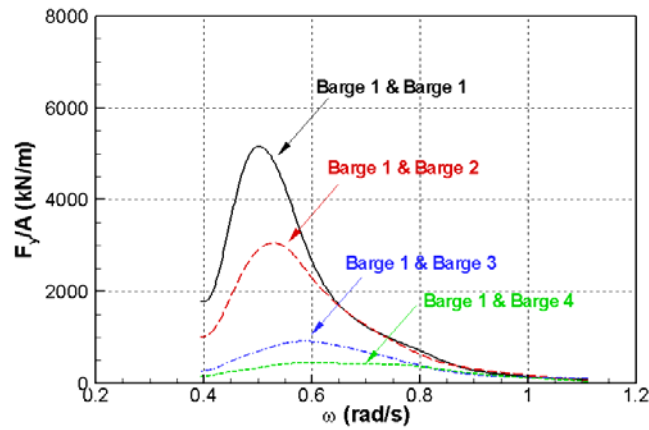


Fig. 4.36 Second-order sway wave forces acting on the barges during the berthing operation with various barge dimensions in head sea ($\lambda/L=1.667$, $H=1.0$ m, $V=2.0$ kts)



(a) Installation Barge



(b) Transportation Barge

Fig. 4.37 Comparison of sway maximum wave excitation force acting on the transportation barge during the berthing operation with various barge dimensions ($H=1.0$ m, $V=2.0$ kts)

Maximum sway wave excitation force with various barge dimensions are suggested in Fig. 4.37. As the transportation barge is getting smaller, the sway

wave excitation force becomes smaller and the peak frequency is shifted to the high frequency range. Interestingly, for certain frequencies, the sway excitation force of smaller barge is bigger than that of barge 1 because of the shift of peak. This fact indicate that the resonance condition is changed according to the lengths of the installation and transportation barge. For the certain frequencies, Barge 2 and Barge 3 caused more severe wave forces rather than Barge 1. For the viewpoint of the transportation barge, smaller transportation barge results in smaller wave excitation force.

4.6 Effect of berthing path

In the marine operation, the transportation barge can select various routes to approach the installation barge. In order to investigate the effect of berthing path on the hydrodynamic force characteristics, five numerical simulations of different berthing paths are carried out. Fig. 4.39 shows the wave fields using the five different berthing paths. In this case, transportation barge is of the same as the installation barge and bow quartering sea condition is considered. Berthing speed is 2.0 knots and berthing path is selected with interval of 45 degree.

Fig. 4.40 shows first-order sway wave excitation force with various berthing paths. Sheltering effect is clearly observed when the angle of berthing path is 315° and 0° . For the berthing paths of 225° and 270° , slight amplitude modulation is shown as the transportation barge is approaching to the installation barge. Maximum sway force happens when the berthing path is 225° . Fig. 4.41 shows second-order sway wave forces with various berthing paths. Second-order sway drift force clearly shows sheltering effect when the angle of berthing path is 315° and 0° . Largest second-order sway drift force happens in the berthing path of 225° .

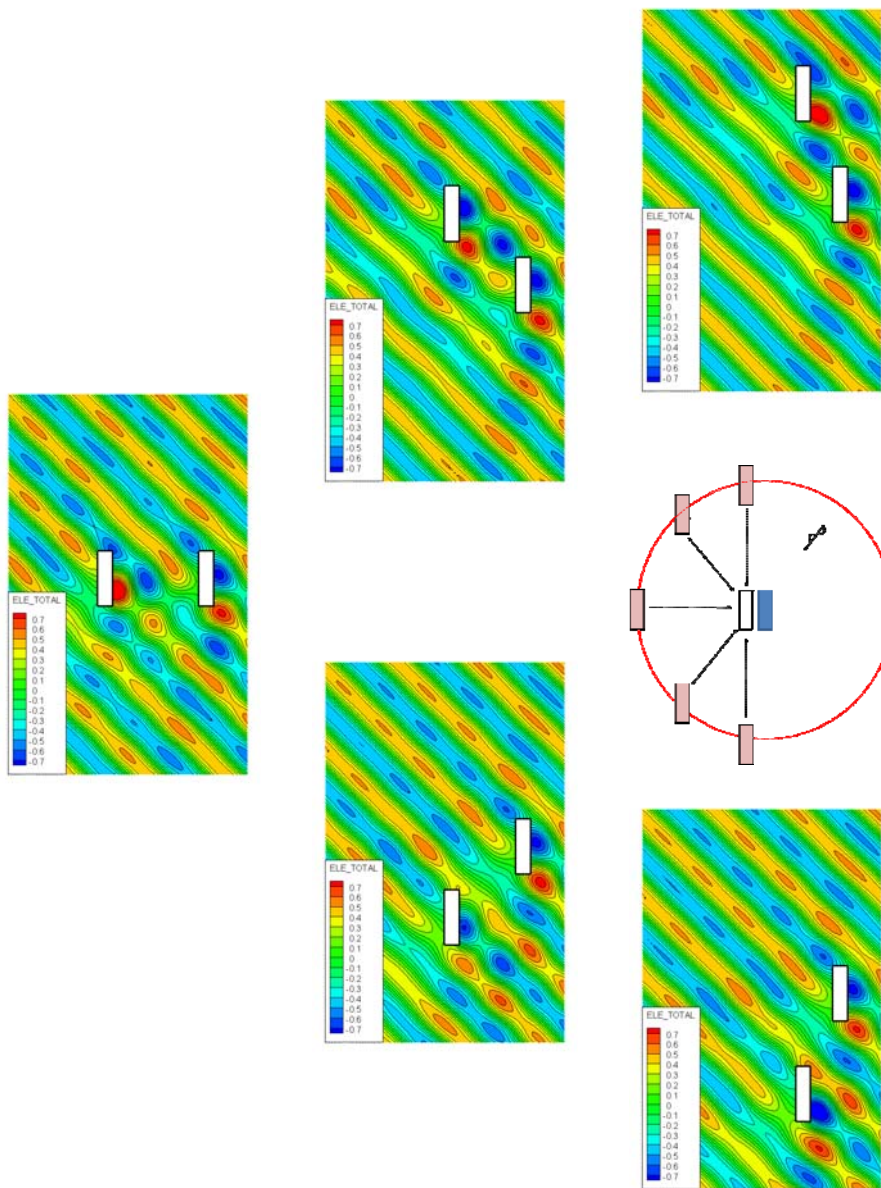


Fig. 4.38 Wave field around the barges during the berthing operation with various berthing paths (Heading 135°, H=1.0m, V=2.0 kts)

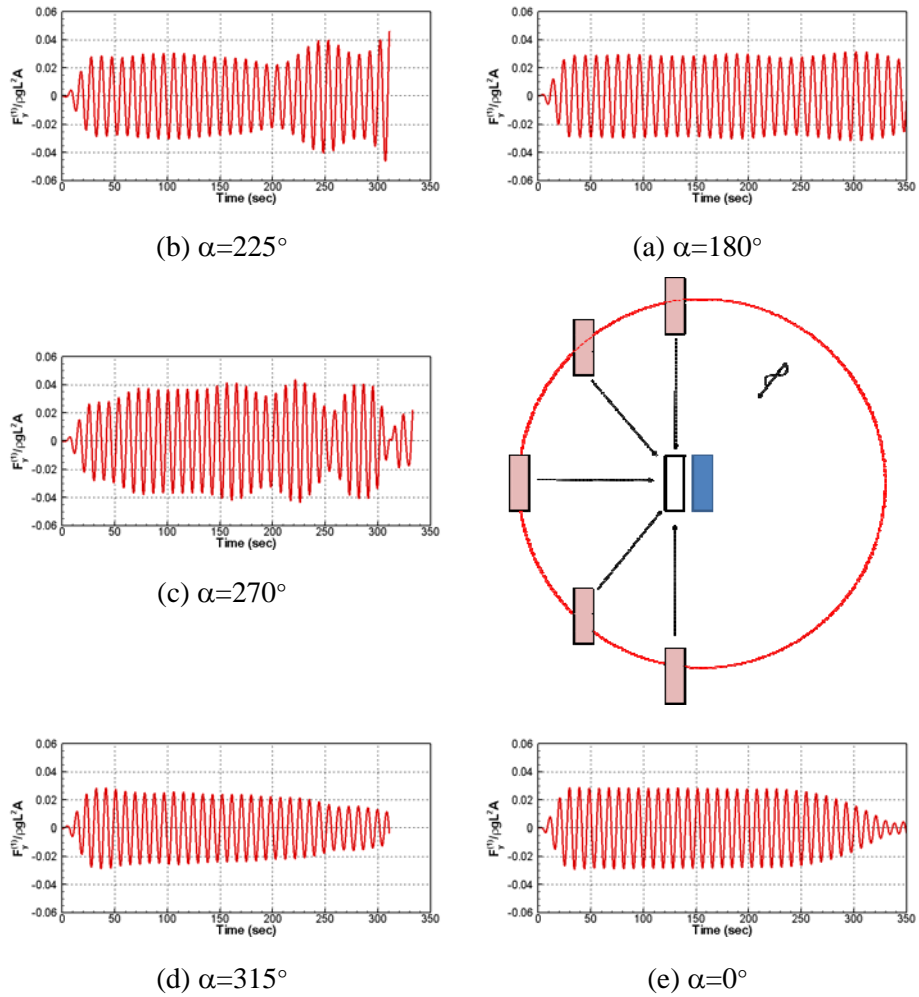
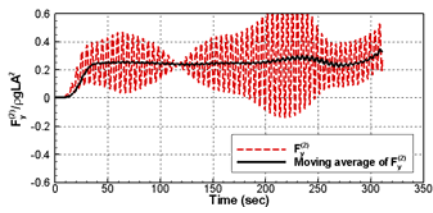
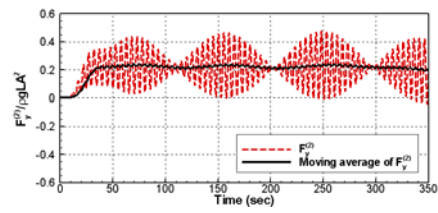


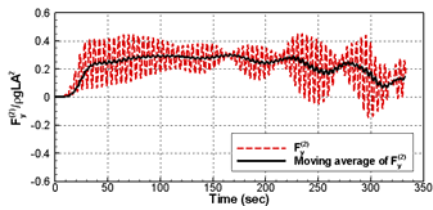
Fig. 4.39 Sway excitation forces acting on the transportation barge during the berthing operation with various berthing paths (Heading 135° , $H=1.0\text{m}$, $V=2.0\text{ kts}$)



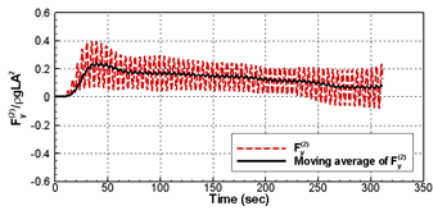
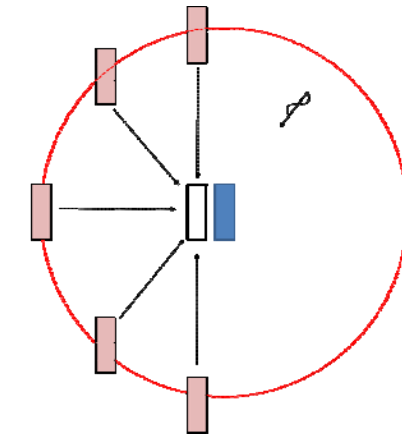
(b) $\alpha=225^\circ$



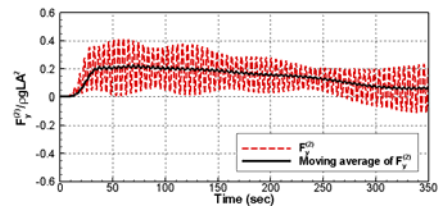
(a) $\alpha=180^\circ$



(c) $\alpha=270^\circ$



(d) $\alpha=315^\circ$



(e) $\alpha=0^\circ$

Fig. 4.40 Sway excitation forces acting on the transportation barge during the berthing operation with various berthing paths (Heading 135° , $H=1.0\text{m}$, $V=2.0\text{ kts}$)

Chapter 5. Berthing Problem between FPSO and Shuttle Tanker

5.1 Problem definition

Among various types of offshore platforms used for oil and gas exploration, FPSOs are used most widely, which is a ship-type offshore structure that has accommodation, numerous storage tanks, offloading facilities, and a mooring system. An FPSO generally remains stationary at the exploration location using spread or turret mooring system. A shuttle tanker or LNG carrier periodically visits the FPSO to transfer oil or gas from it. These transfer operations are a key element of FPSO operation. In this operation, the shuttle tanker is berthed to the moored FPSO, and the transfer operation is performed in the side-by-side or tandem configuration. For the former operation, the shuttle tanker approaches the starboard side of the FPSO, and for the latter operation, the shuttle tanker berths at the front or back of the FPSO. The transfer operation lasts a few hours, after which the shuttle tanker de-berths from the FPSO.

During berthing operations in the open sea, the FPSO and shuttle tanker experience wave-induced motion responses. The horizontal motion of the FPSO is generally limited by the spread or turret mooring system. The shuttle tanker is controlled by the tug or some other type of berthing-assistance system. The two vessels also experience vertical motions including heave, roll

and pitch.

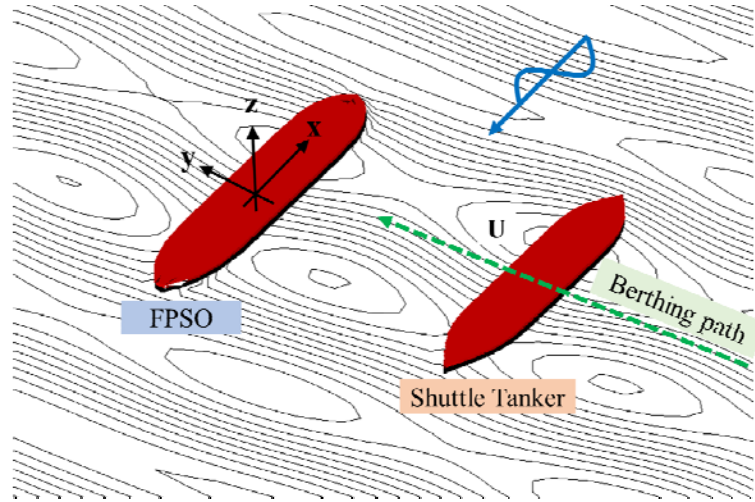


Fig. 5.1 Berthing problem for FPSO and shuttle tanker

In this chapter, the berthing problem between the FPSO and the shuttle tanker is investigated by the present numerical method with a focus on the wave-induced motion response of the vessels during the berthing operation. Fig. 5.1 shows the present berthing problem for FPSO and shuttle tanker. Table 5.1 shows the principle dimensions of FPSO and shuttle tanker. In the simulation, the initial separation distance between the FPSO and the shuttle tanker is 400m, and the berthing speed is 2 knots. The shuttle tanker is assumed to follow the straight berthing path and approach the starboard side of the FPSO for side-by-side transfer operation. Regular and irregular wave simulations are conducted under various wave frequencies and headings.

Table 5.1 Principle dimensions of FPSO and shuttle tanker

Item	FPSO	Shuttle tanker
L	239 m	223 m
B	45.82 m	42.00 m
T	15.80 m	8.37 m
Displ.	139000.0 m ³	534000.0 m ³
GM _T	5.0	13.2
T _{Roll}	15.7	9.8

5.2 Berthing in regular wave (I): Head sea

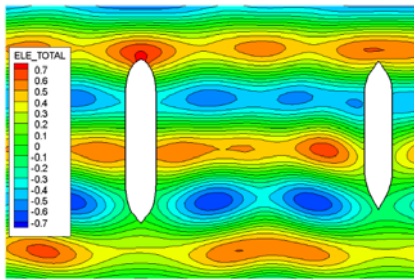
5.2.1 Wave field and motion response

Numerical simulations are conducted to investigate the characteristics of the wave-induced motion response for the berthing problem between the FPSO and the shuttle tanker under regular wave conditions. Fig. 5.2 shows the wave fields around the FPSO and the shuttle tanker during the berthing operation. The wave heading is 180° , which means that the FPSO is aligned with the wave direction. The wave length and height are 150 and 1 m, respectively. It is observed that the disturbed wave fields from each vessel interact with each other as the shuttle tanker berths at the FPSO. After 200 s, the disturbed waves from each vessel meet in the gap region, and the wave between the two vessels becomes higher. In particular, it is clearly observed that strong wave elevation is developed in the gap after 300 s. At this time, the gap distance is lower than 50 m and the wave pattern shows an approximate resonant wave of half the wave length. The wave field shows that the FPSO and shuttle tanker interact with each other via the gap flow.

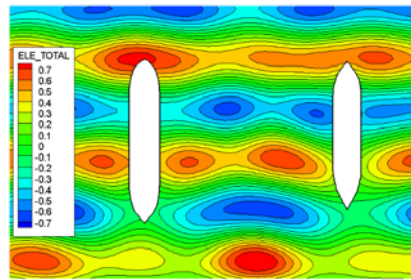
Figs. 5.3 and 5.4 show the motion time series of the FPSO and shuttle tanker during the berthing operation, respectively. The most notable feature of the wave-induced motion response during the berthing operation is the amplitude change despite the regular wave condition. The heave motion of the vessels, for example, shows locally increasing behavior at 150 and 310 s. In addition, the heave response shows a slight decrease at 80 and 220 s. Similar

to heave motion, the roll amplitude of the shuttle tanker increase locally at both 190 s and 330 s. The pitch motion also shows motion amplification and reduction points. These amplitude changes are caused by the change in the wave excitation force with the decrease in the relative distance. During berthing, the relative position of the two vessels continuously changes, and the gap distance decreases steadily.

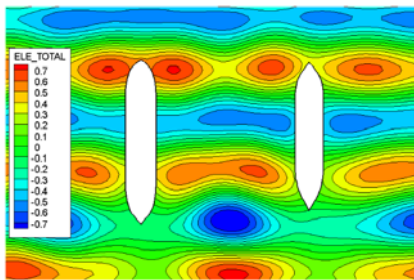
The two vessels interact with each other strongly via the gap flow when they are located closely. The hydrodynamic forces due to the gap flow result in coupled motion responses of the FPSO and shuttle tanker. As a result, roll motion is induced despite the head sea condition as the two vessels approach each other. In particular, heave and roll motions of the shuttle tanker tend to increase sharply as it approaches close to the FPSO after 300 s. The heave amplitude of the shuttle tanker reaches 60% of the incident wave amplitude. The roll amplitude of the shuttle tanker is maximized up to about 5° per unit incident wave amplitude. These abrupt increase of the shuttle tanker motion are attributed to the resonant wave in the gap. Fig. 5.5 shows wave fields and motion time series at roll amplification and reduction points. When the gap distance is around 160 m, gap wave of one and half wave length is shown in the transverse direction. At the second gap distance around 110 m, wave forces due to gap wave of one wavelength reduce the roll and heave motion of the shuttle tanker. When the gap distance is below 50m, gap resonant wave of half wavelength is clearly observed.



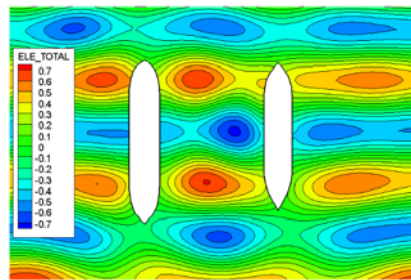
(a) 50 sec



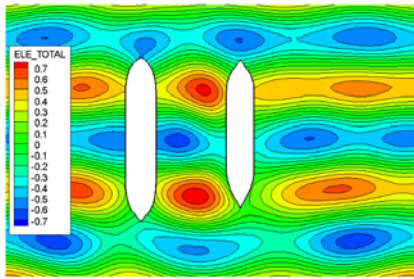
(b) 100 sec



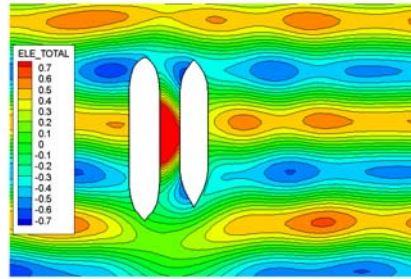
(c) 150 sec



(d) 200 sec

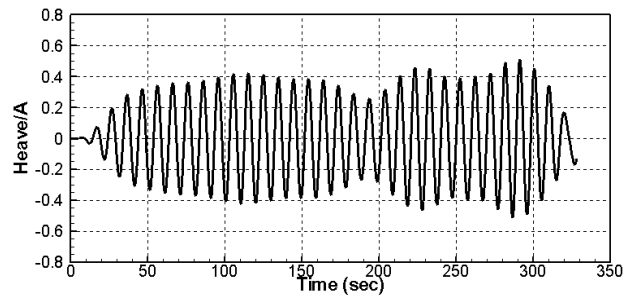


(e) 250 sec

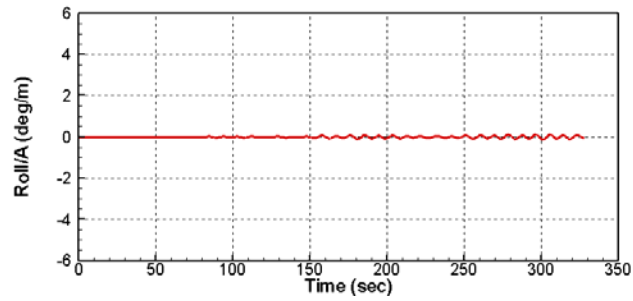


(f) 322 sec

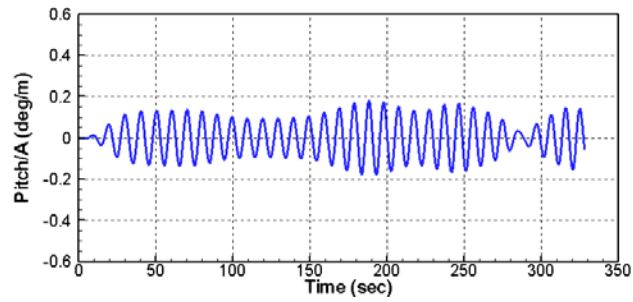
Fig. 5.2 Wave fields around the FPSO and shuttle tanker during the berthing operation in regular wave (Heading 180° , $\lambda=150$ m, $H=1.0$ m, $V=2.0$ kts)



(a) Heave

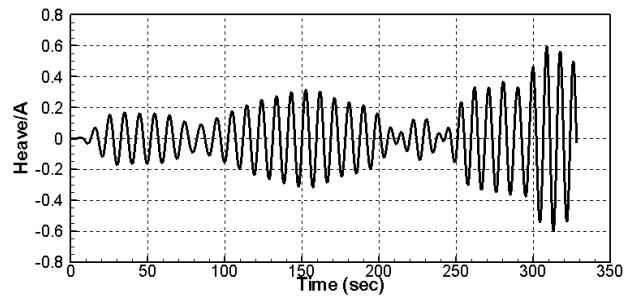


(b) Roll

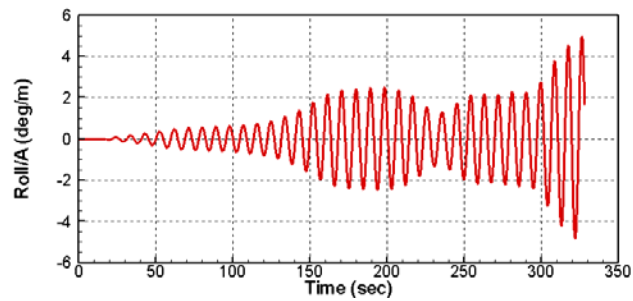


(c) Pitch

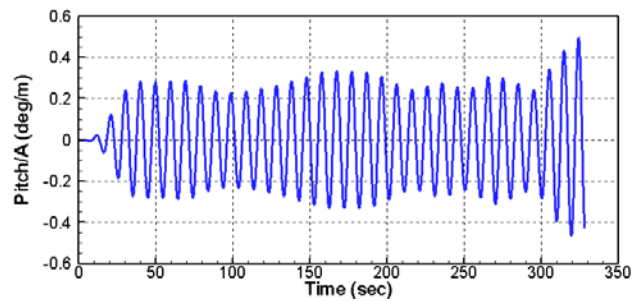
Fig. 5.3 Motion responses of the FPSO during the berthing operation in regular wave (Heading 180° , $\lambda=150$ m, $H=1.0$ m, $V=2.0$ kts)



(a) Heave



(b) Roll



(c) Pitch

Fig. 5.4 Motion responses of the shuttle tanker during the berthing operation in regular wave (Heading 180° , $\lambda=150$ m, $H=1.0$ m, $V=2.0$ kts)

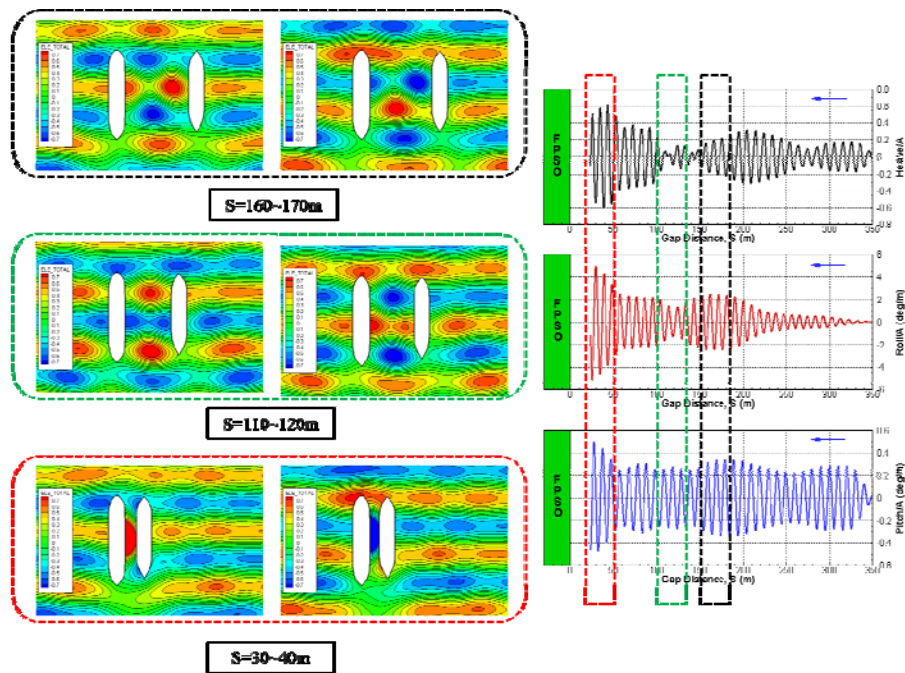


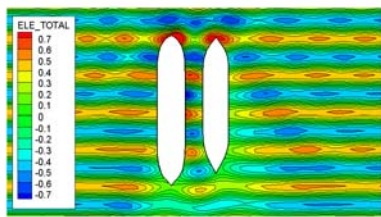
Fig. 5.5 Wave fields at roll amplification points during the berthing operation in regular wave (Heading 180° , $\lambda=150$ m, $H=1.0$ m, $V=2.0$ kts)

5.2.2 Effect of wave frequency

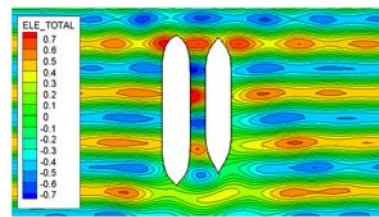
The wave-induced motion responses during the berthing operation are greatly affected by the wave frequency. Fig. 5.6 shows the wave fields during the berthing operation under various wave conditions. It is clearly observed that the wave patterns between the FPSO and shuttle tanker are significantly changed according to the wave length. When the wave length is 60 m, high reflection can be observed in front of the two vessels, and the wave elevation in the gap is not significant. As the wave length increases from 80 to 120 m, the wave field in the gap becomes higher. If the wave length ranges from 140

to 160 m, strong resonant waves are developed in the gap region. When the wave length is greater than 200 m, most waves turn around the vessels rather than going through the gap. This brings about low wave elevation between the FPSO and the shuttle tanker.

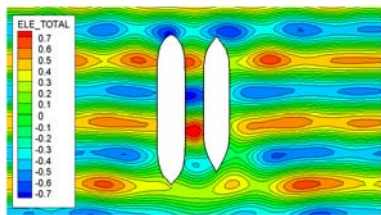
Fig. 5.7 shows a comparison of the heave time series of the shuttle tanker under various wave conditions. To show the spatial characteristics of the heave response according to the relative position, the x-axis represents the gap distance. In this problem, the gap distance is from the starboard side of the FPSO to the port side of the shuttle tanker. If the wave length is less than 100 m, the heave amplitude of the shuttle tanker is smaller than 20% of the incident wave amplitude. When the wave length ranges from 120 to 160 m, the maximum heave amplitude of the shuttle tanker is larger than 40% of the incident wave amplitude. In particular, the heave motion of the shuttle tanker is maximized up to 60% of the incident wave amplitude if the wave length is 140 m and gap distance is less than 50 m. Amplitude changes of heave motion are clearly observed with two or three amplification points even under regular wave conditions. The location of heave amplification changes according to the wave length. As the wave length increase, the amplification location is located farther.



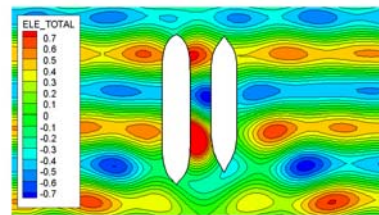
(a) $\lambda=60$ m, $T=6.2$ sec



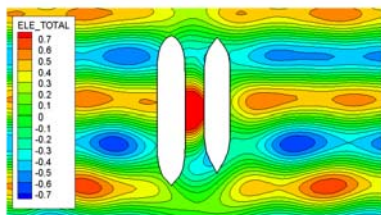
(b) $\lambda=80$ m, $T=7.2$ sec



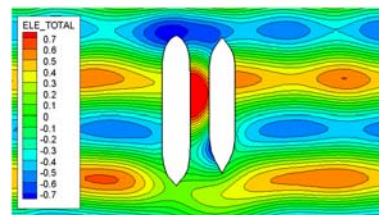
(c) $\lambda=100$ m, $T=8.0$ sec



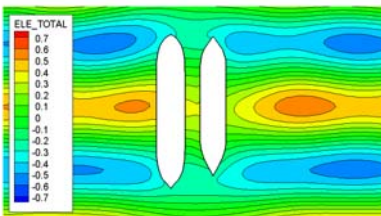
(d) $\lambda=120$ m, $T=8.8$ sec



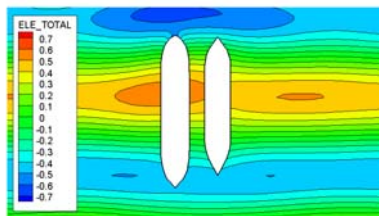
(e) $\lambda=140$ m, $T=9.5$ sec



(f) $\lambda=160$ m, $T=10.1$ sec

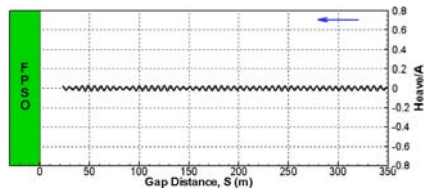


(g) $\lambda=200$ m, $T=11.3$ sec

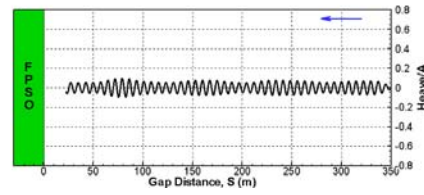


(h) $\lambda=250$ m, $T=12.7$ sec

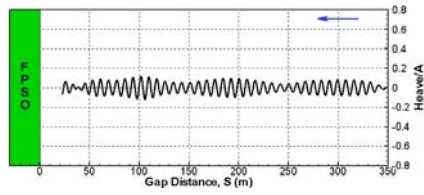
Fig. 5.6 Wave fields during the berthing operation under various regular wave conditions (Heading 180° , $H=1.0$ m, $V=2.0$ kts)



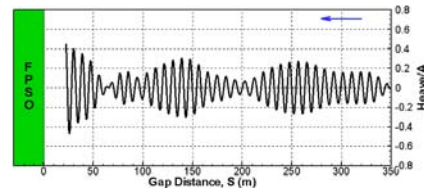
(a) $\lambda=60$ m, $T=6.2$ sec



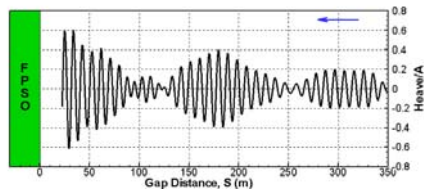
(b) $\lambda=80$ m, $T=7.2$ sec



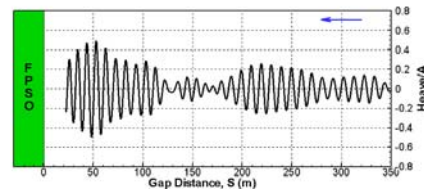
(c) $\lambda=100$ m, $T=8.0$ sec



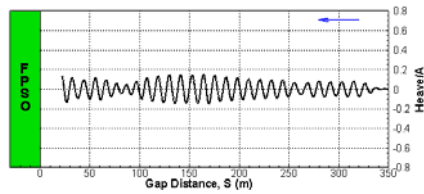
(d) $\lambda=120$ m, $T=8.8$ sec



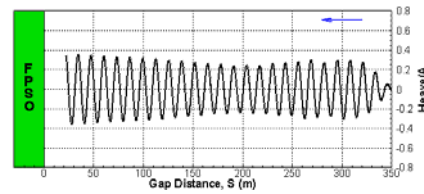
(e) $\lambda=140$ m, $T=9.5$ sec



(f) $\lambda=160$ m, $T=10.1$ sec

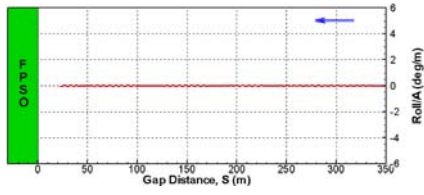


(g) $\lambda=200$ m, $T=11.3$ sec

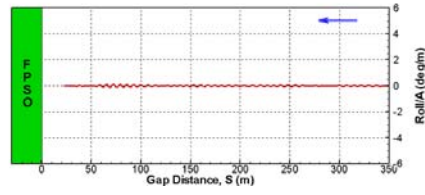


(h) $\lambda=250$ m, $T=12.7$ sec

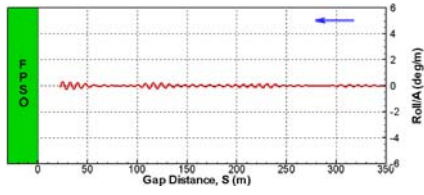
Fig. 5.7 Heave time series of the shuttle tanker during the berthing operation under various regular wave conditions (Heading 180° , $V=2.0$ kts)



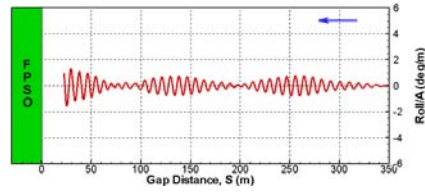
(a) $\lambda=60$ m, $T=6.2$ sec



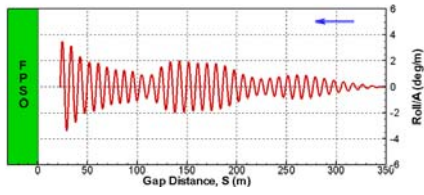
(b) $\lambda=80$ m, $T=7.2$ sec



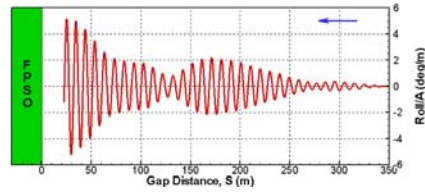
(c) $\lambda=100$ m, $T=8.0$ sec



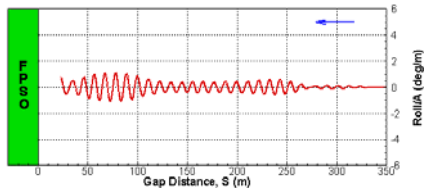
(d) $\lambda=120$ m, $T=8.8$ sec



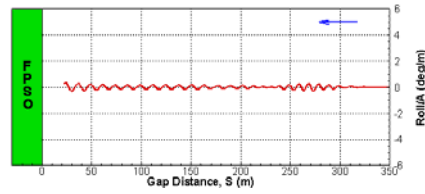
(e) $\lambda=140$ m, $T=9.5$ sec



(f) $\lambda=160$ m, $T=10.1$ sec

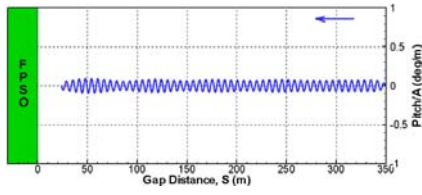


(g) $\lambda=200$ m, $T=11.3$ sec

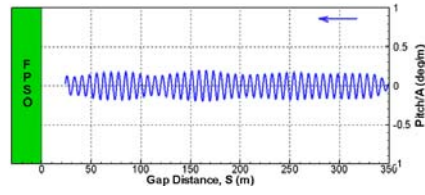


(h) $\lambda=250$ m, $T=12.7$ sec

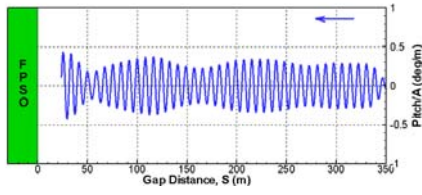
Fig. 5.8 Roll time series of the shuttle tanker during the berthing operation under various regular wave conditions (Heading 180° , $V=2.0$ kts)



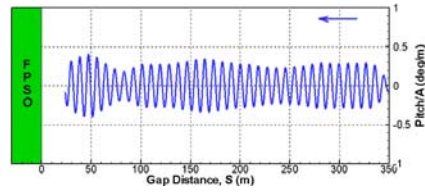
(a) $\lambda=60$ m, $T=6.2$ sec



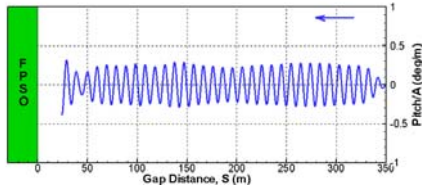
(b) $\lambda=80$ m, $T=7.2$ sec



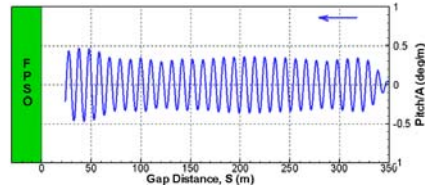
(c) $\lambda=100$ m, $T=8.0$ sec



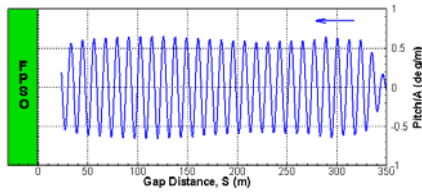
(d) $\lambda=120$ m, $T=8.8$ sec



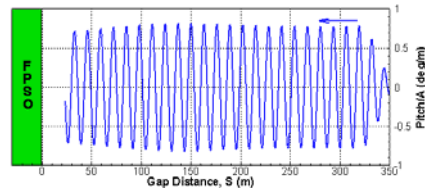
(e) $\lambda=140$ m, $T=9.5$ sec



(f) $\lambda=160$ m, $T=10.1$ sec



(g) $\lambda=200$ m, $T=11.3$ sec



(h) $\lambda=250$ m, $T=12.7$ sec

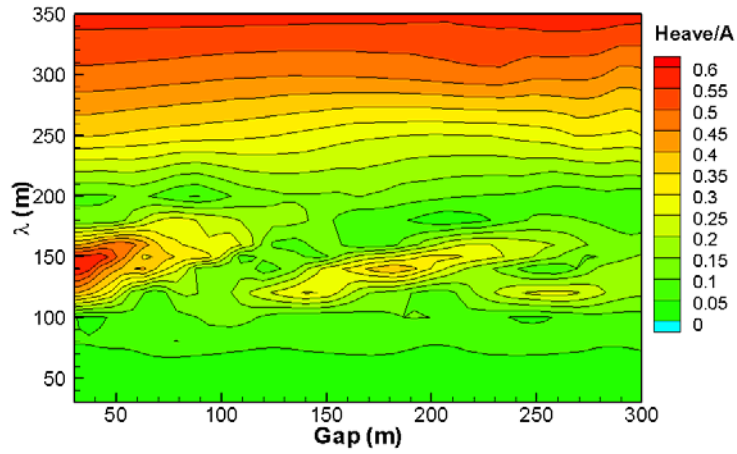
Fig. 5.9 Pitch time series of the shuttle tanker during the berthing operation under various regular wave conditions (Heading 180° , $V=2.0$ kts)

Fig. 5.8 shows the roll time series of the shuttle tanker under various wave length conditions. As the shuttle tanker approaches the FPSO, its roll motion tends to increase steadily. For a wave length below 100 m, the roll amplitude of the shuttle tanker is smaller than 1° per unit wave amplitude. When the wave length ranges between 140 and 180 m, the maximum roll amplitude of the shuttle tanker is greater than 2° per unit wave amplitude. In particular, if the wave length is 160 m, the roll motion of the shuttle tanker is maximized up to 4° per unit wave amplitude. As with the heave motion, amplitude changes are clearly observed in the roll time series.

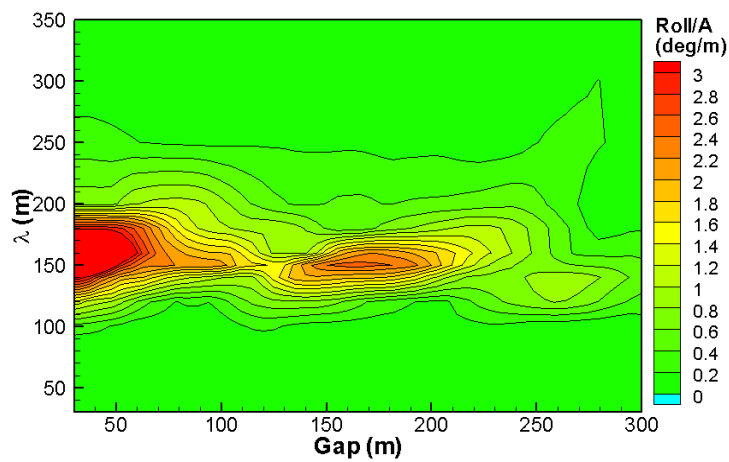
The pitch motion of the shuttle tanker shows relatively little effect due to the berthing operation. Fig. 5.9 shows the pitch time series of the shuttle tanker under various wave conditions. The pitch motion amplitudes are almost same except when the shuttle tanker is very close to the FPSO. As the wave length increases, the pitch motion of the shuttle tanker increases steadily.

To investigate the overall spatial characteristics of the motion response under various wavelength conditions, the motion amplitude contours of the shuttle tanker during the berthing operation are shown in Fig. 5.10. From the contour, it can be seen that the heave motion of the shuttle tanker increases with the wave length. Furthermore, local amplification points are observed when the wave length is about 150 m. These amplifications are caused by the pumping mode resonance in the gap. The roll amplitude contour shows localized amplification areas with respect to wave length and gap distance. Large roll motion of the shuttle tanker occurs only if the wave length ranges from 150 to 200m and gap distance is below 100 m. The pitch amplitude

contour confirms that the pitch motion of the shuttle tanker is relatively less affected by relative position change during the berthing operation.

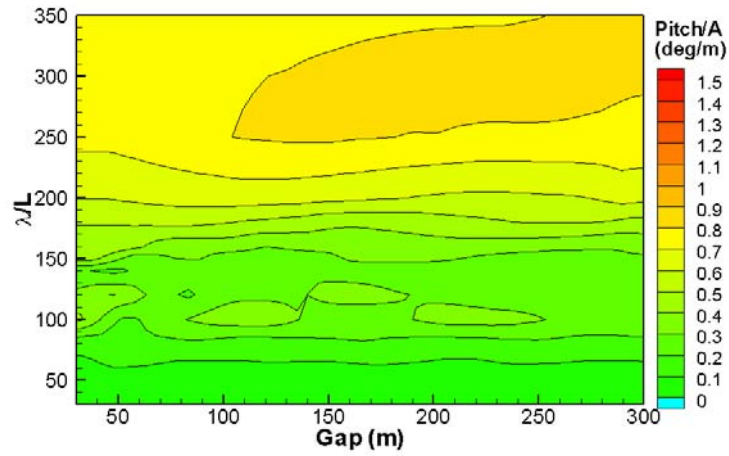


(a) Heave amplitude contour



(b) Roll amplitude contour

Fig. 5.10 Motion amplitude contours of the shuttle tanker during the berthing operation (Heading 180°, V=2.0 kts)



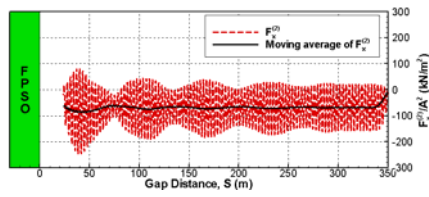
(c) Pitch amplitude contour

Fig. 5.10 Continued

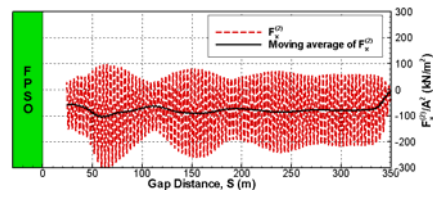
Figs. 5.11 and 5.12 shows second-order surge and sway wave forces acting on the shuttle tanker during berthing operation under various wave conditions, respectively. In order to identify the wave drift force, the moving averaged value of the second-order force is plotted together. The wave drift force is an important parameter in the berthing problem because it is related to the required thrust of the berthing-assistance system. Relatively, a second-order surge force shows steady time series during the berthing operation. This indicates that the wave drift force in the surge direction is not changed significantly during the berthing operation. On the other hand, the second-order sway force is greatly affected by the wave frequency. If the wave length is smaller than 100 m or larger than 200 m, the second-order wave force is quite small. On the contrary, when the wave length ranges from 120 to 160 m,

the second-order sway wave force increases sharply. This can be explained by the development of strong wave elevation in the gap between the FPSO and the shuttle tanker. Basically repulsive sway drift force acts on the FPSO and shuttle tanker in the outward direction.

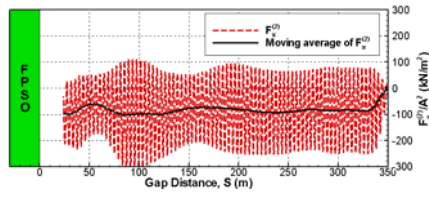
Fig. 5.13 shows the contour plot for surge and sway drift forces. In this figure, the drift force is evaluated by applying a moving average filter just like Figs 5.11 and 5.12. The surge drift force increases when the wave length is short. The highest surge drift force is observed for a wave length of 100 m. The behavior of the surge drift force during the berthing operation does not change significantly except for a dramatic change for a wave length less than and more than 150 m. Similar to the roll amplitude contour, the sway drift force is locally amplified only if the wave length is 100-200m and gap distance is below 70 m. Maximum sway drift force can be found for a wave length of ~150m.



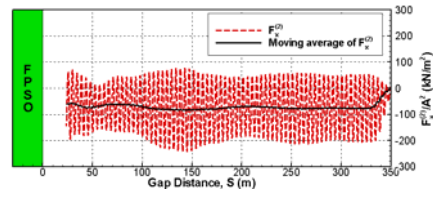
(a) $\lambda=60$ m, $T=6.2$ sec



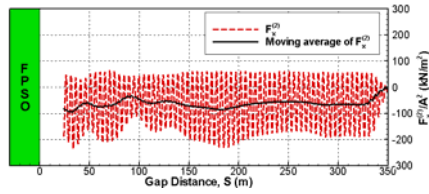
(b) $\lambda=80$ m, $T=7.2$ sec



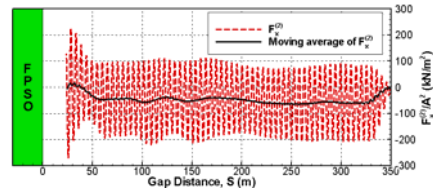
(c) $\lambda=100$ m, $T=8.0$ sec



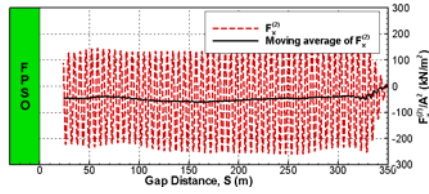
(d) $\lambda=120$ m, $T=8.8$ sec



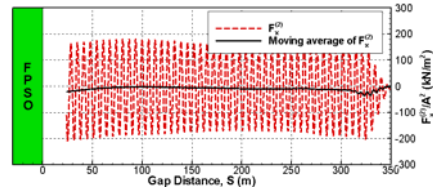
(e) $\lambda=140$ m, $T=9.5$ sec



(f) $\lambda=160$ m, $T=10.1$ sec

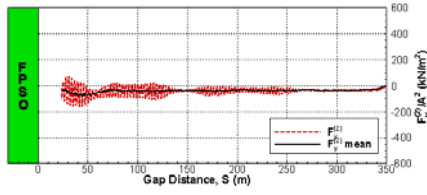


(g) $\lambda=200$ m, $T=11.3$ sec

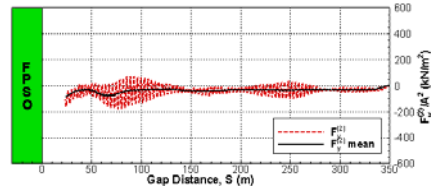


(h) $\lambda=250$ m, $T=12.7$ sec

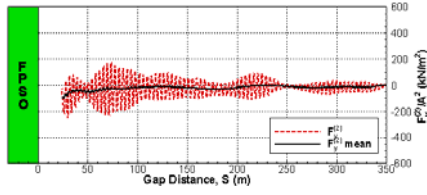
Fig. 5.11 Second-order surge wave forces acting on the shuttle tanker under various regular wave conditions (Heading 180° , $V=2.0$ kts)



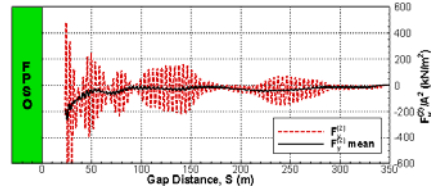
(a) $\lambda=60$ m, $T=6.2$ sec



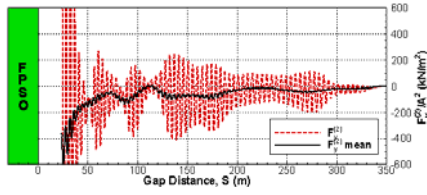
(b) $\lambda=80$ m, $T=7.2$ sec



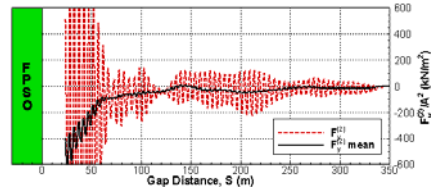
(c) $\lambda=100$ m, $T=8.0$ sec



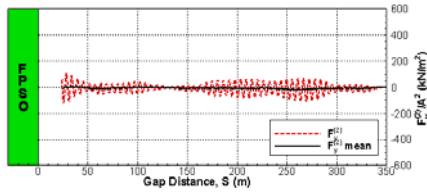
(d) $\lambda=120$ m, $T=8.8$ sec



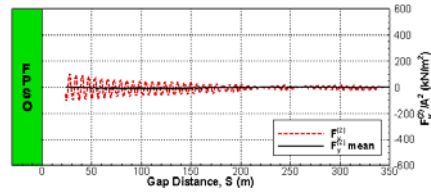
(e) $\lambda=140$ m, $T=9.5$ sec



(f) $\lambda=160$ m, $T=10.1$ sec

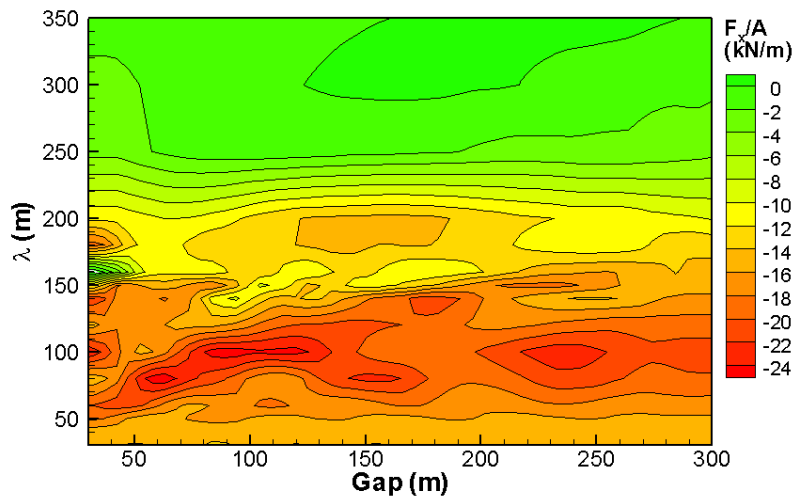


(g) $\lambda=200$ m, $T=11.3$ sec

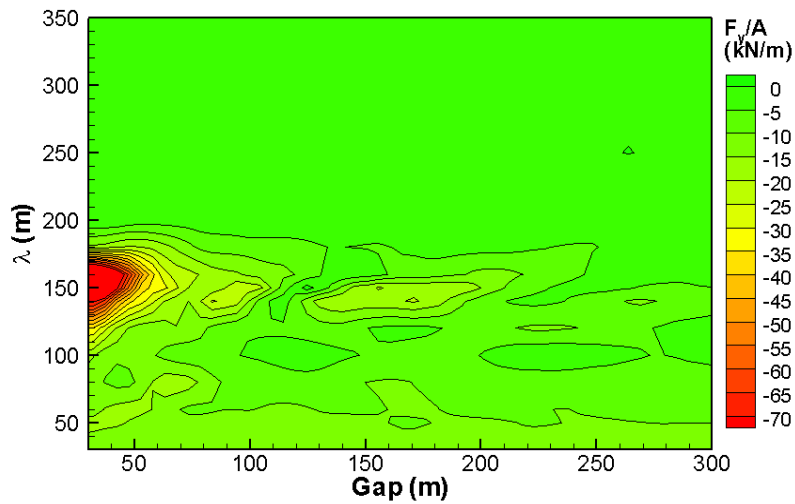


(h) $\lambda=250$ m, $T=12.7$ sec

Fig. 5.12 Second-order sway wave forces acting on the shuttle tanker under various regular wave conditions (Heading 180° , $V=2.0$ kts)



(a) Surge drift force contour



(b) Sway drift force contour

Fig. 5.13 Wave drift force contours of the shuttle tanker under various regular wave conditions (Heading 180° , $V=2.0$ kts)

5.2.3 Effect of berthing speed

The berthing speed, a key parameter in berthing operations, can be determined by considering the thrust of tugs and environmental conditions. Near the FPSO, high berthing speed is not allowed because of high collision possibility. In this study, we considered four different berthing speeds from 1 to 4 knots. Although the berthing speed may change depending on the relative location and wave conditions, it is assumed constant during berthing operation. Fig. 5.14 shows the heave time series of the shuttle tanker with four different berthing speeds for wave lengths of 150 m. Because the x-axis represents the gap distance, low berthing speed gives dense trajectories within a given gap distance. As the berthing speed increases, the trajectories become sparse. Basically, at low berthing speed, it can be expected that the quasi-steady characteristics of the heave motion reveals a function of the relative position (i.e., gap distance) during the berthing operation. Therefore, amplitude change is relatively complex when the berthing speed is 1 knot. There are many heave amplification and reduction points. On the other hand, the amplitude change pattern becomes simpler as the berthing speed increases. This is because the shuttle tanker passes by the amplification position with relatively high speed. The localized force characteristics in space cannot be revealed with high berthing speed. As a result, the maximum value of heave motion of the shuttle tank decreases with an increase in the berthing speed. Interestingly, the behavior of the heave responses for main amplification locations remains regardless of the berthing speed. For example, an increase in the heave

response can be found at gap distances of 40 and 200m. Similarly, a slight decrease in the heave response can be found at gap distances of 130 and 270m.

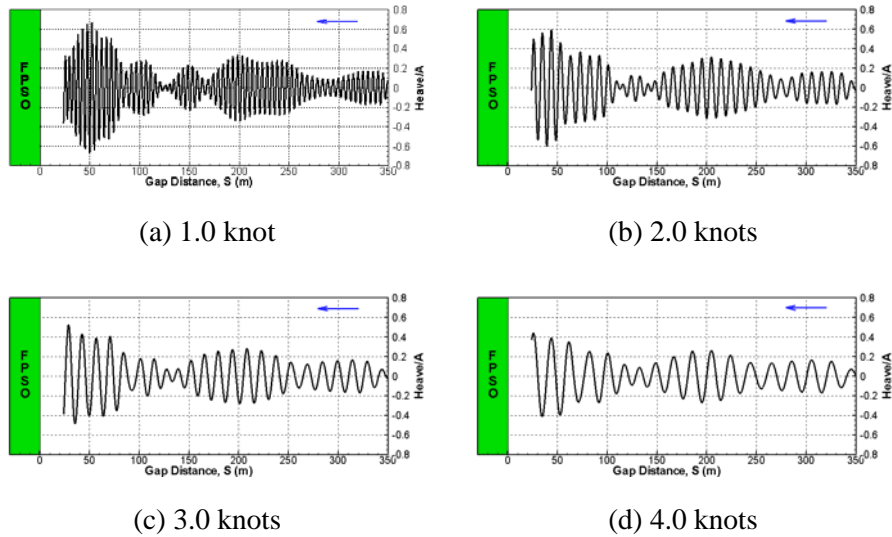
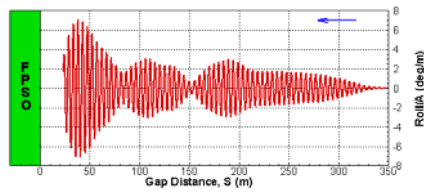


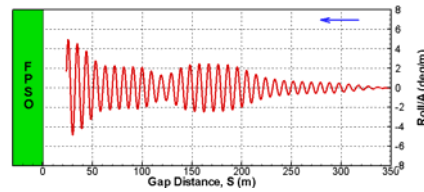
Fig. 5.14 Heave time series of the shuttle tanker during the berthing operation with four different berthing speeds (Heading 180° , $\lambda=150$ m)

Figs. 5.15 shows the time series of the roll motion of the shuttle tanker with four different berthing speeds. Similar to the heave motion, amplitude change is more clearly observed when the berthing speed is low. As the berthing speed increases, the pattern of the roll amplitude becomes simpler. In addition, the maximum roll amplitude decreases as the shuttle tanker approaches with higher speed. For all cases, most significant roll motion is observed at gap distances below 50 m. It is worthy to mention the roll response at higher speed is larger than that at low speed at some locations.

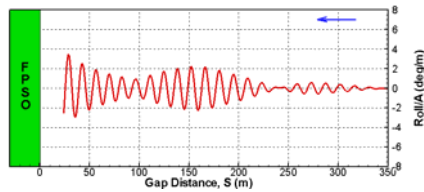
Because the potential damping for roll motion is relatively small, the memory effect lasts longer than heave and pitch motions. For this reason, memory effect can increase the roll motion locally at high berthing speed.



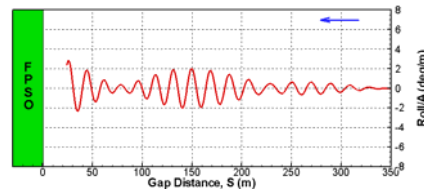
(a) 1.0 knot



(b) 2.0 knots



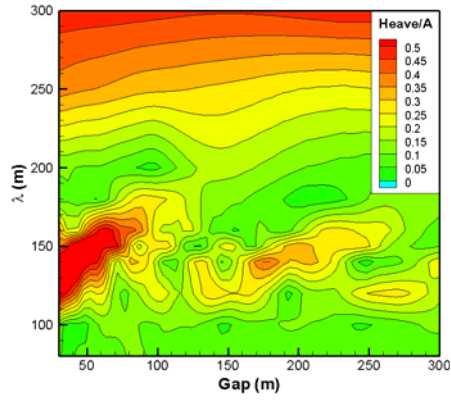
(c) 3.0 knots



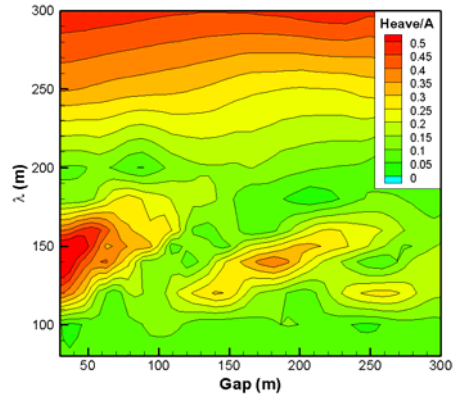
(d) 4.0 knots

Fig. 5.15 Roll time series of the shuttle tanker during the berthing operation with four different berthing speeds (Heading 180° , $\lambda=150$ m)

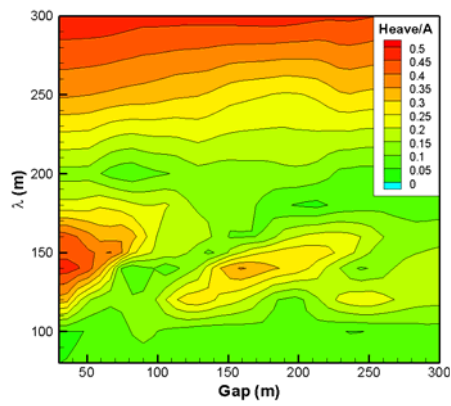
Figs. 5.16 and 5.17 show heave and roll amplitude contours at four berthing speeds, respectively. The overall trends of the motion amplitude contours are quite similar regardless of the berthing speeds. Meanwhile, it can be seen that the peak amplitude of the heave and roll motions decreases as the berthing speed increases. In addition, the pattern of the amplitude contours becomes simpler with an increase in the berthing speed.



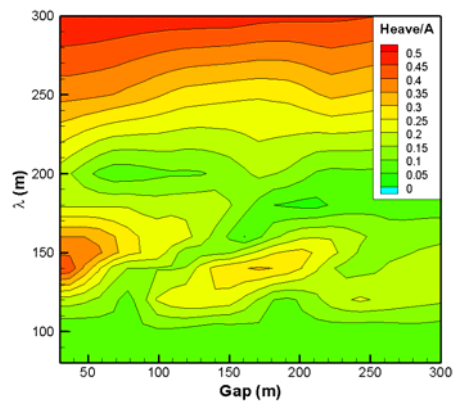
(a) 1.0 knot



(b) 2.0 knots

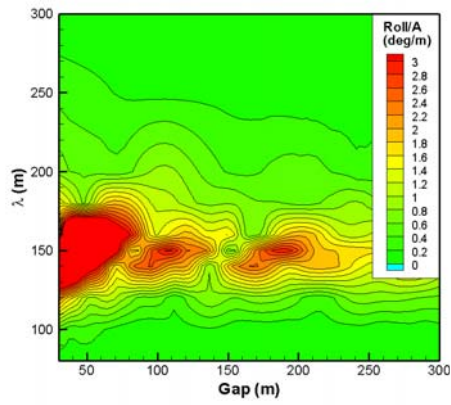


(c) 3.0 knots

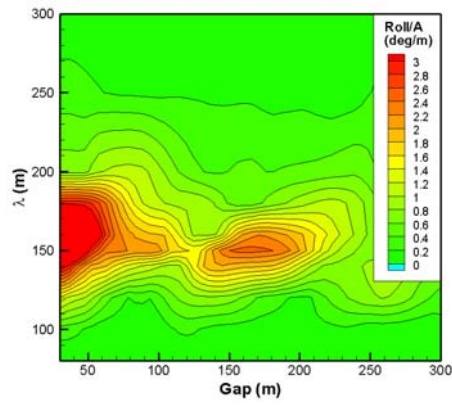


(d) 4.0 knots

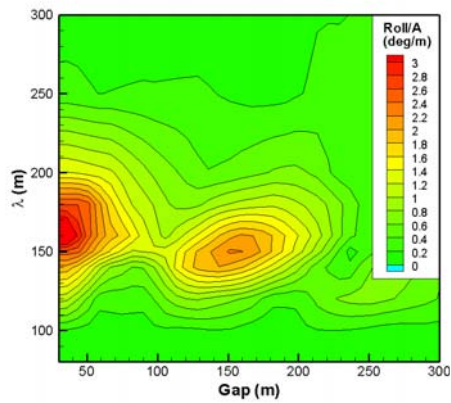
Fig. 5.16 Heave amplitude contours of the shuttle tanker during the berthing operation with four different berthing speeds (Heading 180°)



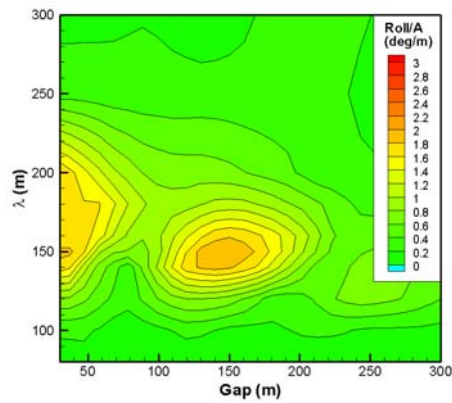
(a) 1.0 knot



(b) 2.0 knots



(c) 3.0 knots



(d) 4.0 knots

Fig. 5.17 Roll amplitude contours of the shuttle tanker during the berthing operation with four different berthing speeds (Heading 180°)

Fig. 5.18 shows the time series of the second-order sway forces acting on the shuttle tanker at four different berthing speeds. As the berthing speed increases, the repulsive wave drift force decreases. Basically, the wave drift

force is mainly a function of the square of the relative wave elevation. High berthing speed blocks or relaxes the development of the relative wave elevation. Fig. 5.19 shows sway drift force contours of the shuttle tanker during the berthing operation with four different berthing speeds. When the berthing speed is 1 knot, localized amplification areas are clearly observed with respect to wave length and gap distance. As the berthing speed increase, it can be seen that maximum value of sway drift force decrease and the amplification area becomes wider.

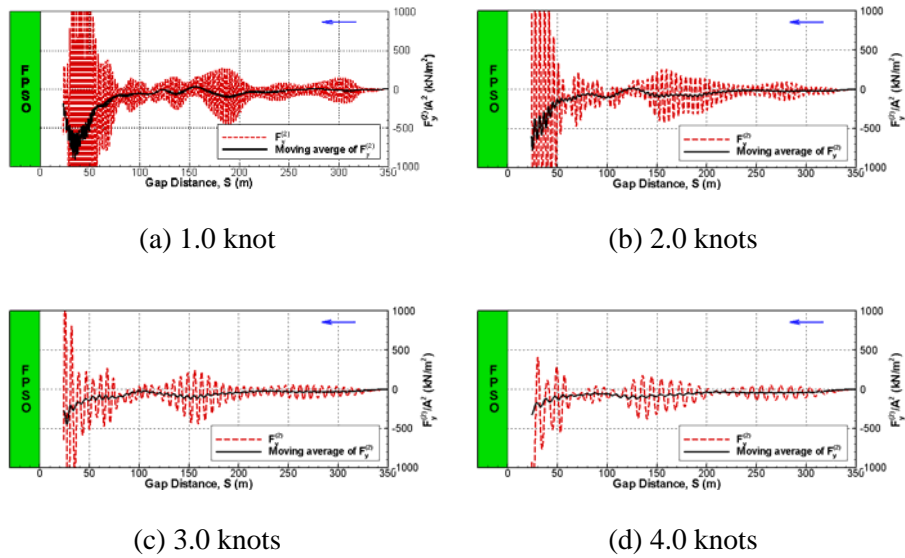
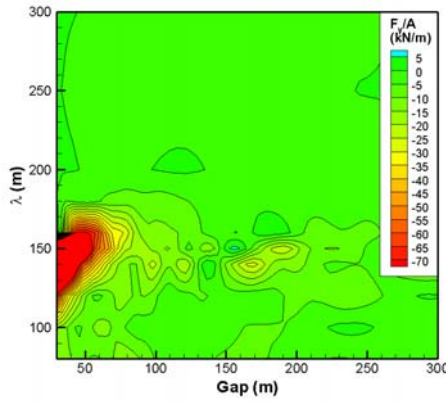
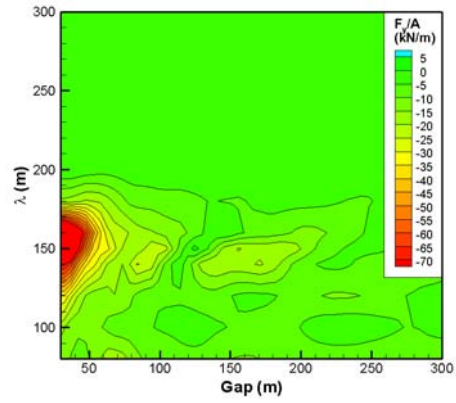


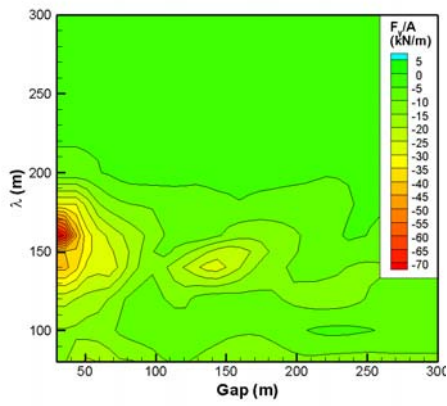
Fig. 5.18 Second-order sway force acting on the shuttle tanker during the berthing operation with four berthing speeds (Heading 180°, $\lambda=150$ m)



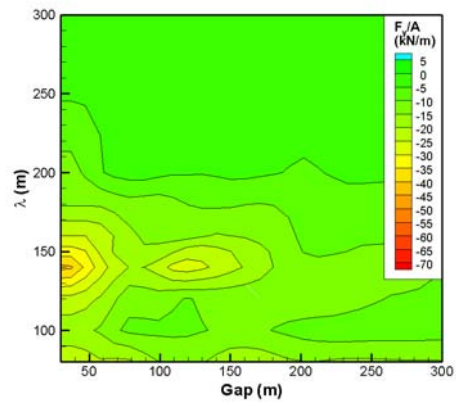
(a) 1.0 knot



(b) 2.0 knots



(c) 3.0 knots

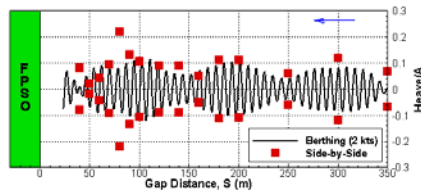


(d) 4.0 knots

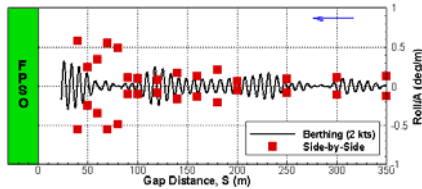
Fig. 5.19 Sway drift force contours of the shuttle tanker during the berthing operation with four berthing speeds (Heading 180°)

5.2.4 Comparison between dynamic and quasi-steady results

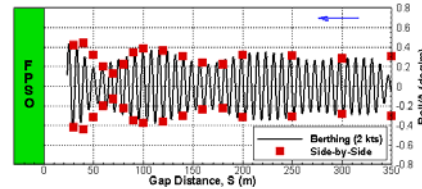
Fig. 5.20 shows the comparison of dynamic and quasi-steady motion responses of the shuttle tanker when the wave length is 100m. In this case, dynamic results indicate the motion time series from the present berthing simulation. Quasi-steady results means the calculations in side-by-side configuration. From the figure, heave and pitch motion show that dynamic results are almost same as the quasi-steady calculations. Meanwhile, large discrepancy can be found in roll motion around the gap distance of 70m. It can be understood that the dynamic effect due to berthing speed delays and reduces the roll resonant response.



(a) Heave

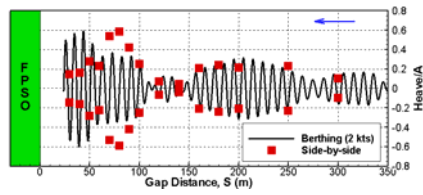


(b) Roll

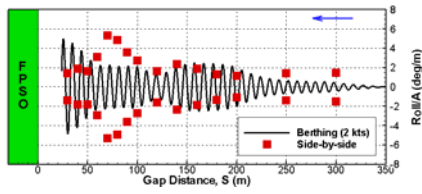


(c) Pitch

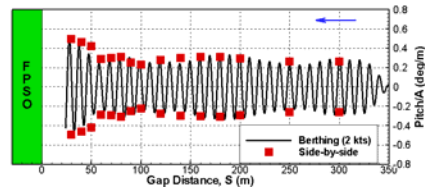
Fig. 5.20 Comparison of dynamic and quasi-steady motion response
(Heading 180°, $\lambda=100$ m)



(a) Heave



(b) Roll



(c) Pitch

Fig. 5.21 Comparison of dynamic and quasi-steady motion response
(Heading 180° , $\lambda=150$ m)

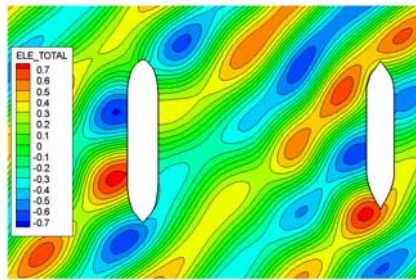
Fig. 5.21 shows another comparison of dynamic and quasi-steady motion response when the wavelength is 150 m. From the heave and roll motion, dynamic effect is clearly observed. The delay and reduction of resonant motion response can be found at both heave and roll of shuttle tanker. Pitch motion, however, shows that berthing response is almost same as the motion behavior in side-by-side configuration.

5.3 Berthing in regular wave (2): Quartering and beam sea

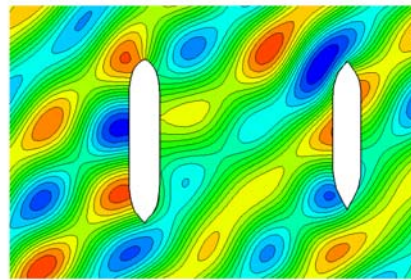
If the FPSO is moored by a certain mooring system, it can be subjected to incident waves with various headings. Wave-induced motion responses of the FPSO and shuttle tanker during berthing are greatly affected by wave heading. In particular, sheltering effect may increase or decrease the motion of the shuttle tanker. In order to investigate the effect of wave heading on the wave-induced motion response during berthing, numerical simulations of the berthing problem are conducted under quartering and beam sea conditions.

5.3.1 Wave-induced motion response in quartering sea

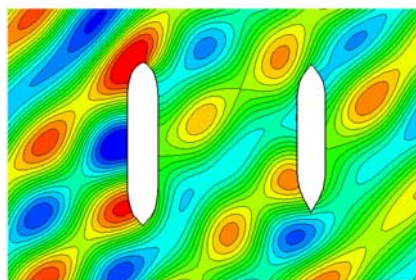
Fig 5.22 shows snapshots of the wave fields during the berthing operation under a wave heading of 225° . The wave length and height are 150 and 1 m, respectively. In this case, the port sides of the shuttle tanker and FPSO are directly exposed to the incident wave during the berthing operation. As a result, strong reflection can be found in the area around the port side of the FPSO. When the shuttle tanker approaches close to the FPSO, it goes to the lee side of the FPSO. In particular, after 150 s, the shuttle tanker enters the sheltering area by the FPSO and the wave elevation between the FPSO and the shuttle tanker becomes quite low. This is because the FPSO acts as breakwater (Hong *et al.*, 2005). This sheltering effect results in decrease of hydrodynamic force acting on the shuttle tanker.



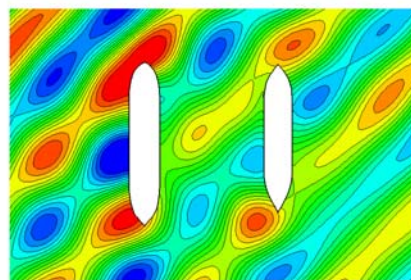
(a) 50 sec



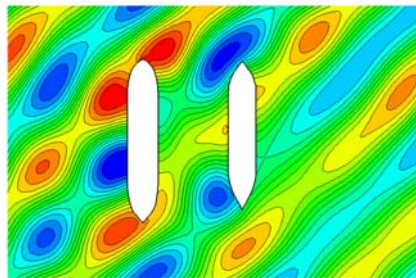
(b) 100 sec



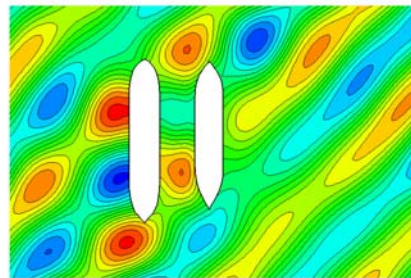
(c) 150 sec



(d) 200 sec

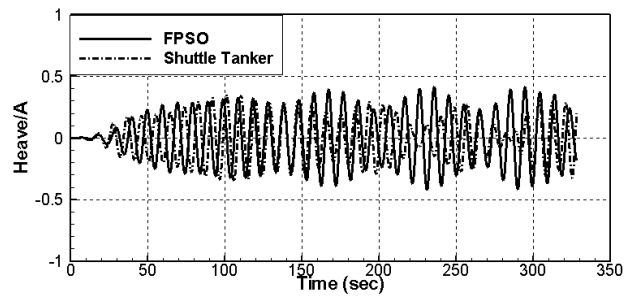


(e) 250 sec

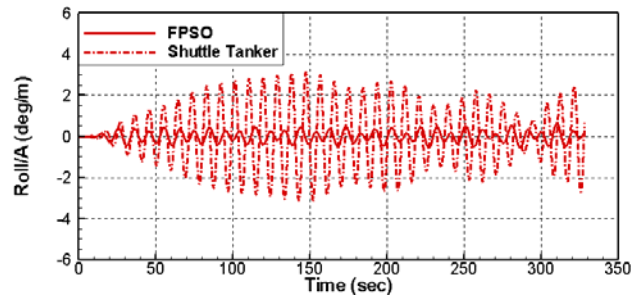


(f) 300 sec

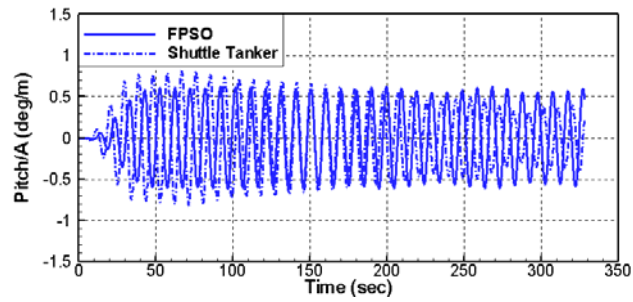
Fig. 5.22 Wave fields during berthing between the FPSO and shuttle tanker in quartering sea ($\beta=225^\circ$, $\lambda=150$ m, $H=1.0$ m, $V=2.0$ kts)



(a) Heave



(b) Roll



(c) Pitch

Fig. 5.23 Motion responses of the FPSO and shuttle tanker during the berthing operation in quartering sea ($\beta=225^\circ$, $\lambda=150$ m, $V=2.0$ kts)

Fig. 5.23 shows the wave-induced motion responses of the FPSO and shuttle tanker during the berthing operation when the wave heading is 225° . Amplitude modulation can be found in the heave time series of the FPSO. Heave amplitude of the FPSO reaches about 40% of the incident wave amplitude. As the shuttle tanker enters the sheltering zone, it is clearly observed that the roll and pitch response of the shuttle tanker tend to decrease steadily after 150 s. Roll maximum of the shuttle tanker is about 3° per unit incident wave amplitude.

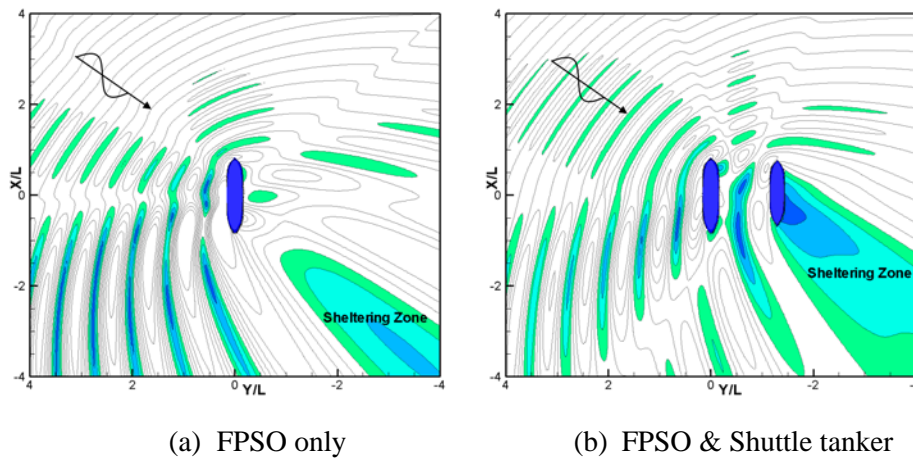


Fig. 5.24 Sheltering zones around the FPSO w/o and w/ shuttle tanker in quartering sea based on frequency-domain solutions ($\beta=225^\circ$, $\lambda=150$ m)

Fig. 5.24 shows sheltering zone around the FPSO in quartering sea based on the frequency-domain solutions (see Appendix C). For the case of FPSO only, the sheltering zone is located far from the vessel in the opposite

direction of wave heading. Meanwhile, when the FPSO is located in side-by-side configuration with the shuttle tanker, the sheltering zone is attached to the shuttle tanker with wider area. This wide sheltering zone brings about the decrease of hydrodynamic force acting on the shuttle tanker, shown in Fig. 5.21 (b) and (c).

Fig. 5.25 shows the heave and roll amplitude contours of the shuttle tanker during the berthing operation when the wave heading is 225° . Regardless of the gap distance, the heave motion increases with the wave length. The roll amplitude demonstrates the sheltering effect clearly. The maximum roll amplitude is larger than 3° per unit wave amplitude when the gap distance is greater than 200 m and wave length is 150-200 m. As the shuttle tanker approaches close to the FPSO, the roll amplitude decreases.

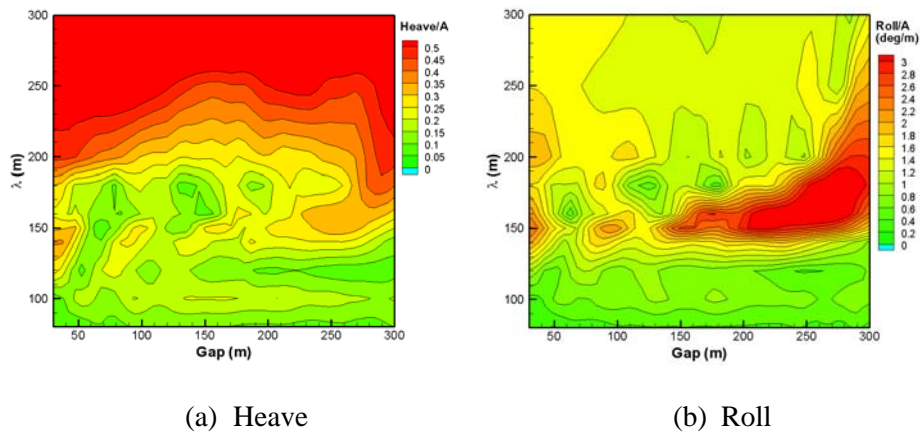


Fig. 5.25 Motion amplitude contours of the shuttle tanker during berthing in quartering sea ($\beta=225^\circ$, $V=2.0$ kts)

Fig. 5.26 shows snapshots of the wave fields during the berthing operation when the wave heading is 135° . In this simulation, the wave length and height are 150 m and 1 m, respectively. Berthing speed is 2 knots. During the berthing operation, the starboard sides of the vessels are directly exposed to the incident wave. Therefore, strong reflected waves can be found in the area around the starboard sides of the two vessels. As the two vessels approach each other, the FPSO is located in the sheltering zone by the shuttle tanker.

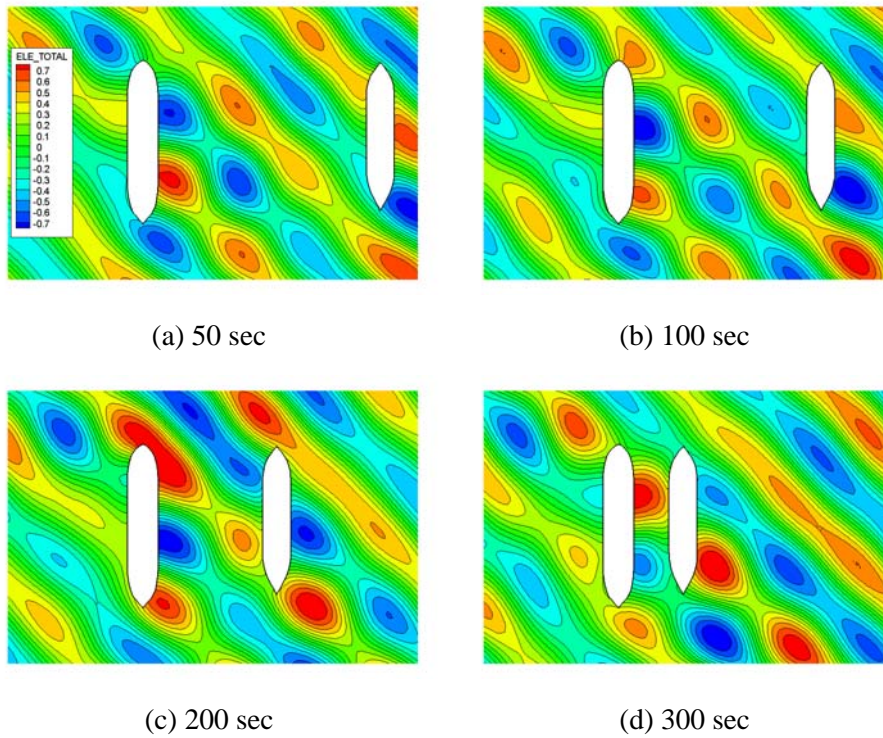
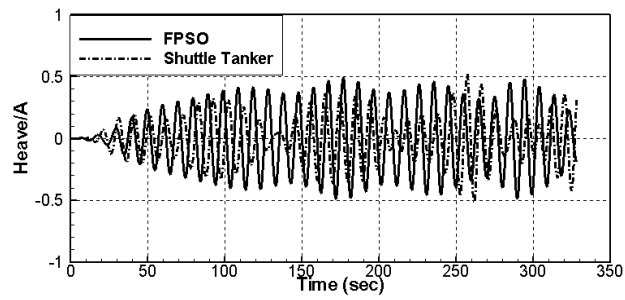


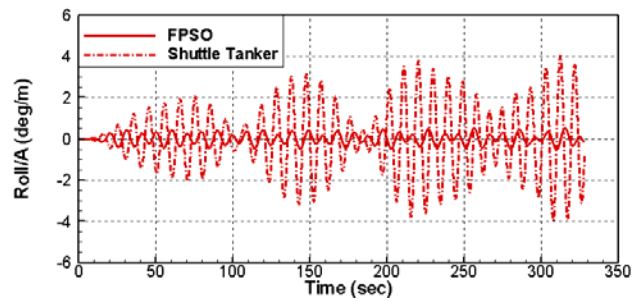
Fig. 5.26 Wave fields around FPSO and shuttle tanker during the berthing operation ($\beta=135^\circ$, $\lambda=150$ m, $H=1.0$ m, $V=2.0$ kts)

Fig. 5.27 shows a comparison of the wave-induced motion response of the FPSO and shuttle tanker during the berthing operation in quartering sea. Strong amplitude modulation can be found in the motion time series of the shuttle tanker rather than those of the FPSO. This is because the shuttle tanker is directly exposed to the incident waves, and its displacement is relatively small. The heave amplitudes of the FPSO and shuttle tanker reach about 50 % of the incident wave amplitude. The roll amplitude of the shuttle tanker is maximized up to about 4° per unit incident wave amplitude.

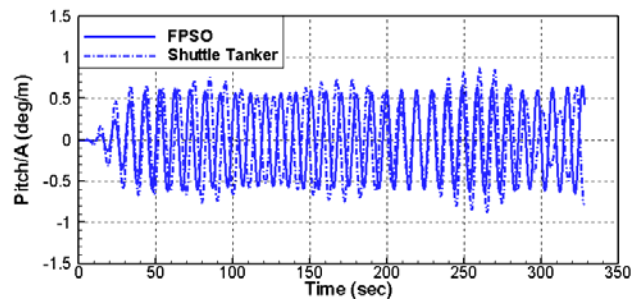
Fig. 5.28 shows the motion time series and wave fields at three heave amplification points. Interestingly, the roll motion is locally minimized at all heave amplification points. This means that strong roll moment acts to reduce the roll motion of the shuttle tanker. The pitch motion increases with the heave motion. At the first amplification point, the wave field shows one wave crest and two troughs in the transverse direction between the FPSO and the shuttle tanker. At the second amplification point, the wave field shows one crest and one trough trapped in the gap between the FPSO and the shuttle tanker. At the third amplification point, the wave field shows only one crest or trough trapped in the gap between the FPSO and the shuttle tanker. These trapped waves produce a large excitation force that results in heave amplification.



(a) Heave

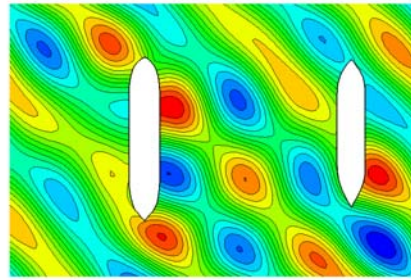
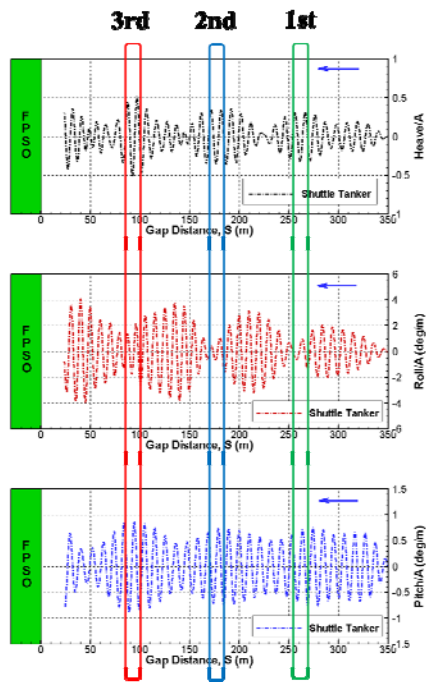


(b) Roll

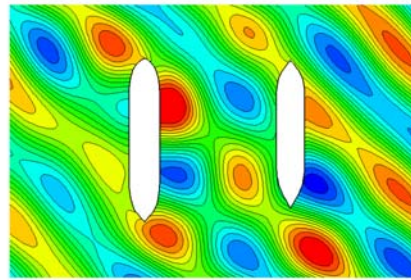


(c) Pitch

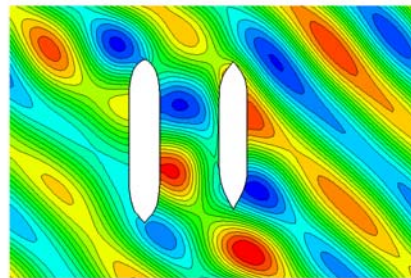
Fig. 5.27 Motion time series of the FPSO and shuttle tanker during the berthing operation ($\beta=135^\circ$, $\lambda=150$ m, $H=1.0$ m, $V=2.0$ kts)



(a) 1st amplification ($S/\lambda=2.1$)



(b) 2nd amplification ($S/\lambda=1.5$)



(c) 3rd amplification ($S/\lambda=0.9$)

Fig. 5.28 Motion time series(left) and wave field(right) at heave amplification points during the berthing operation ($\beta=135^\circ$, $\lambda=150$ m, $H=1.0$ m, $V=2.0$ kts)

Fig. 5.29 shows the heave and roll amplitude contours of the shuttle tanker during the berthing operation in quartering sea. Regardless of the gap distance, the heave motion increases with the wave length. At a wave length of about 150 m, amplitude modulation is observed along the gap distance. When the wave length ranges from 120 to 170 m, high roll motion is expected during the berthing operation. In addition, high amplitude modulation is also induced under the same conditions.

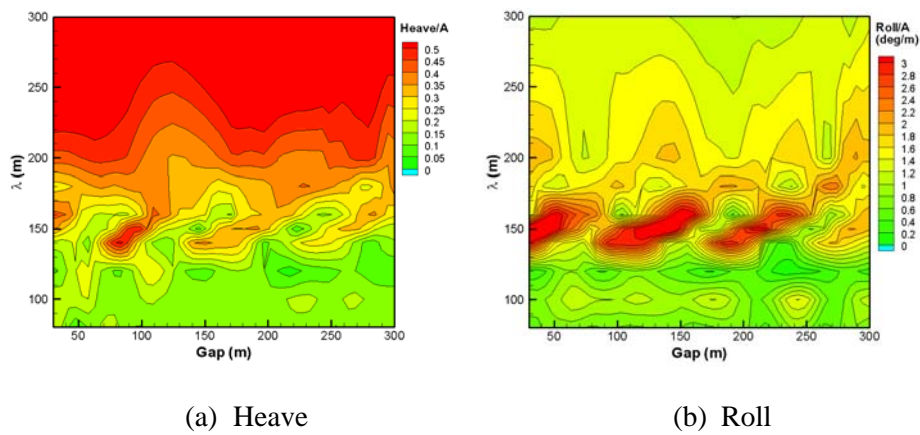
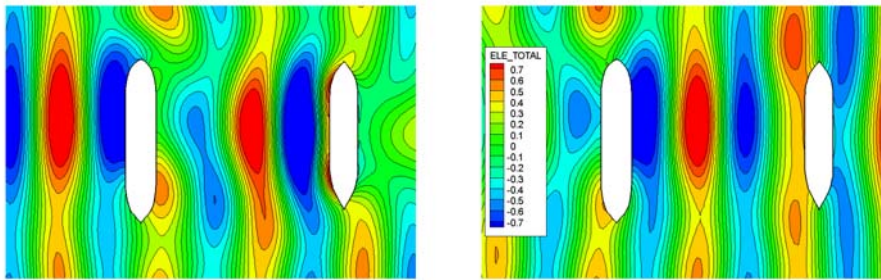


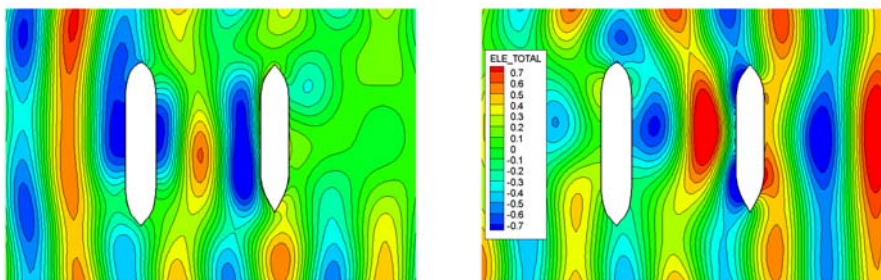
Fig. 5.29 Motion amplitude contours of the shuttle tanker during berthing in quartering sea ($\beta=135^\circ$, $V=2.0$ kts)

5.3.2 Wave-induced motion response in beam sea

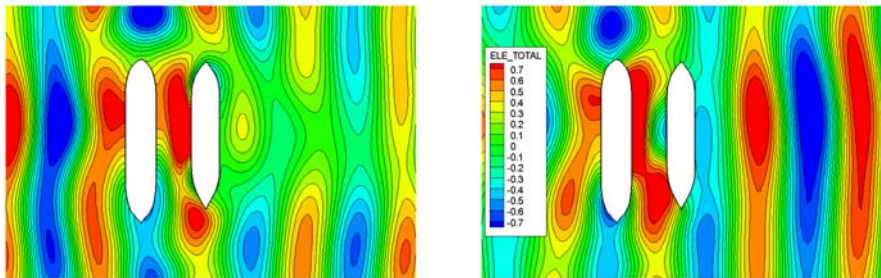
Fig. 5.30 shows the snapshots of wave fields during the berthing operation under the two beam sea conditions. In this case, wave length is 150 m. When the wave heading is 270° , strong reflected waves are developed at the port side areas of the two vessels. By contrast, with the wave heading of 90° , strong reflection can be found at the starboard sides of the vessels.



(a) 100 sec

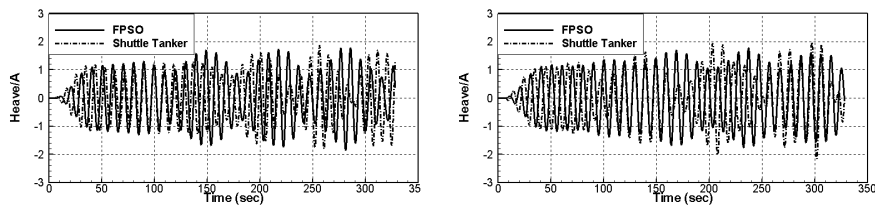


(b) 200 sec

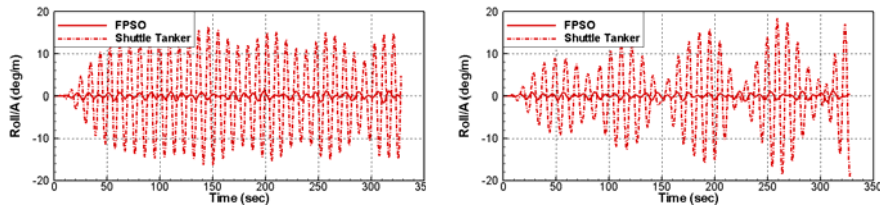


(c) 300 sec

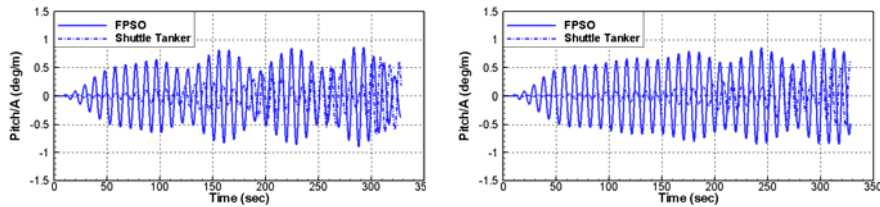
Fig. 5.30 Wave fields during the berthing operation in beam sea ($\beta=270^\circ$ (left) & 90° (right), $\lambda=150$ m, $H=1.0$ m, $V=2.0$ kts)



(a) Heave



(b) Roll



(c) Pitch

Fig. 5.31 Motion time series of the FPSO and shuttle tanker during the berthing operation ($\beta=270^\circ$ (left) & 90° (right), $\lambda=150$ m, $V=2.0$ kts)

Fig. 5.31 shows the comparison of motion time series of the FPSO and shuttle tanker during berthing in beam sea. For both headings, the heave amplitudes are bigger than incident wave amplitude. As the shuttle tanker approaches FPSO closely, its heave response increases with amplitude modulations. That means that the presence of adjacent floating bodies increases the hydrodynamic heave excitation forces. Maximum heave amplitude during

berthing is almost twice of the incident wave amplitude. Roll time series shows that roll responses of shuttle tanker with wave heading of 270° and 90° are quite different. For the case of 270° , the roll motion of the shuttle tank decrease steadily due to the sheltering effect. When the wave heading is 90° , the roll motion of the shuttle tanker increases with strong amplitude modulation. In this case, the shuttle tanker, which is directly exposed to the incident wave, goes through the strongly reflected region by the FPSO during berthing.

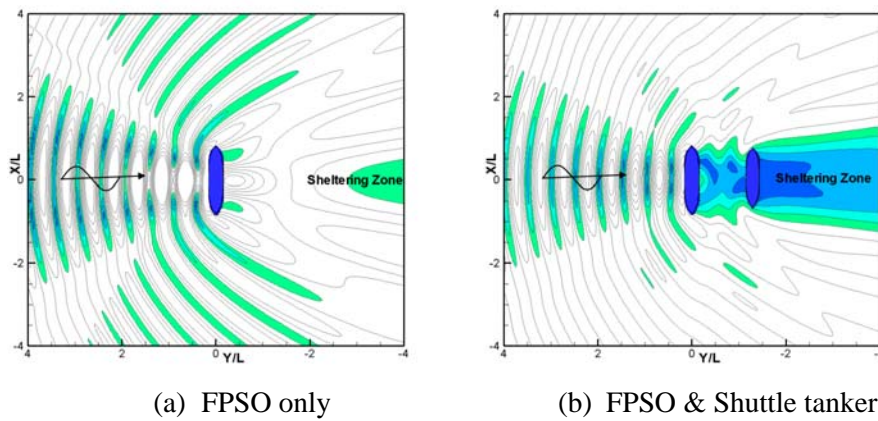


Fig. 5.32 Sheltering zone around the FPSO w/o and w/ shuttle tanker in beam sea based on frequency-domain solutions ($\beta=270^\circ$, $\lambda=150\text{m}$)

Fig. 5.32 shows the sheltering zone around the FPSO based on the frequency-domain solutions. If the FPSO only is located in the open sea, the sheltering zone is not significant. However, If the FPSO is located in the side-by-side configuration with the shuttle tanker, the sheltering zone become quite large. This sheltering zone make sheltering effect on the roll

motion of shuttle tanker.

Fig. 5.33 shows heave and roll amplitude contours of the shuttle tanker in beam sea. For both headings, overall motion response is quite big. The strong amplitude modulation characteristics can be observed in the heave and roll amplitude contours when the wave heading is 90° . Sheltering effect is also found in the roll amplitude contour in wave heading of 270° .

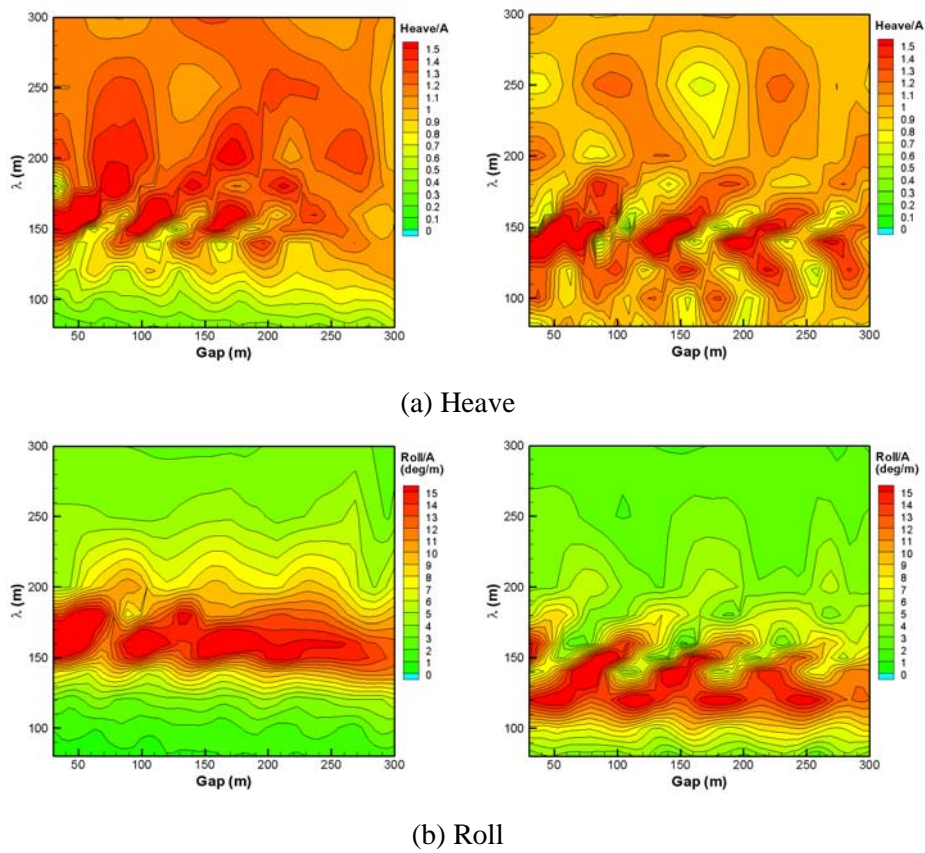


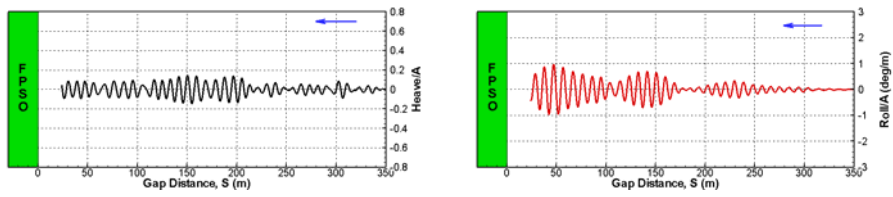
Fig. 5.33 Motion amplitude contours of the shuttle tanker during the berthing operation in beam sea ($\beta=270^\circ$ (left) & 90° (right), $V=2.0$ kts)

5.4 Berthing in irregular wave

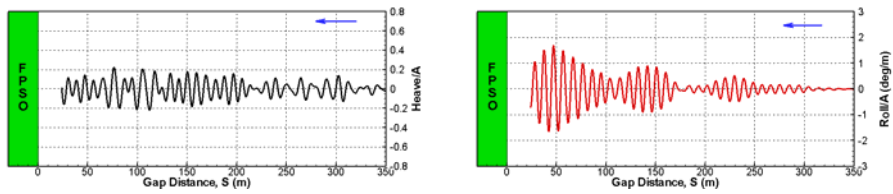
5.4.1 Effect of peak period

Motion responses of the shuttle tanker during the berthing operation in irregular sea are shown in Fig. 5.34. Here, the significant wave height is fixed at 1.0m, whereas the peak period is varied from 8.0 s to 14.0 s. Since the seed number for random phase generation is fixed, the phase angles for each frequency component are the same. The heave motion of the shuttle tanker shows different amplitude trends with different peak period. As the peak period becomes longer, the heave motions of the shuttle taker become larger and the motion period also becomes longer. The maximum heave motion is 40% of incident wave amplitude, which is observed around the gap distance of 100m.

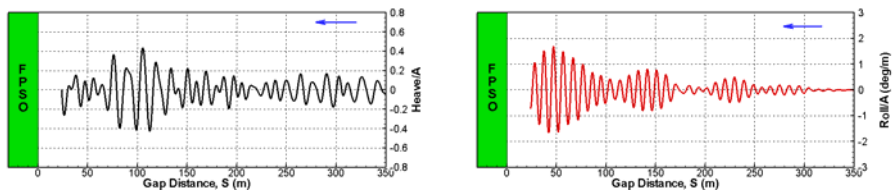
The roll motion of the shuttle tanker shows similar amplitude trends regardless of the peak period. The roll motion periods remains unchanged even when the wave period is changed. This indicates that the roll response of the shuttle tanker is more strongly affected by the gap distance rather than by the wave period. The maximum roll response (i.e., first roll peak) occurs when the gap distance is about 50m. At this time, roll amplitude is about 1.6° per unit wave amplitude. The second roll peak happens around 150m gap distance. There is roll reduction points is found at 110 m and 180 m.



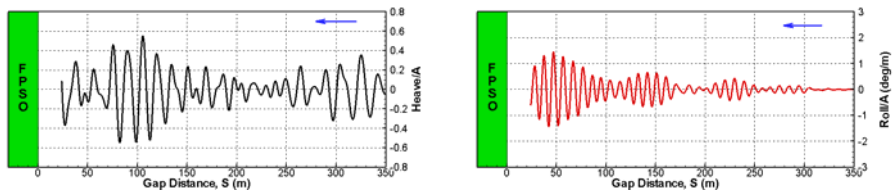
(a) $T_p=8.0$ s



(b) $T_p=10.0$ s

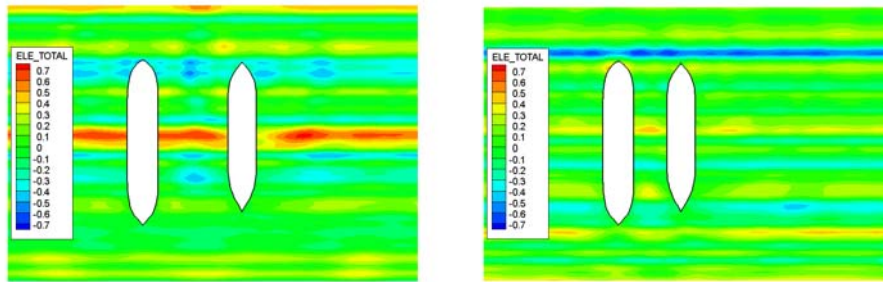


(c) $T_p=12.0$ s

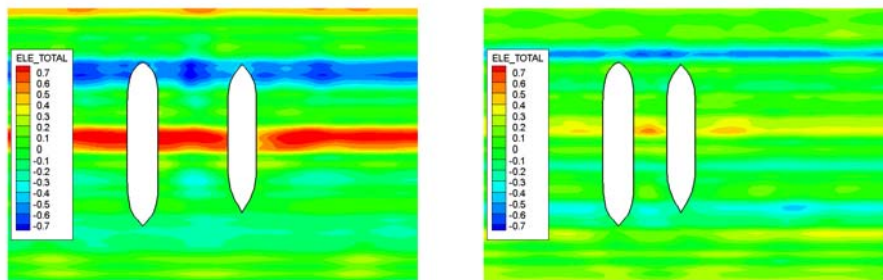


(d) $T_p=14.0$ s

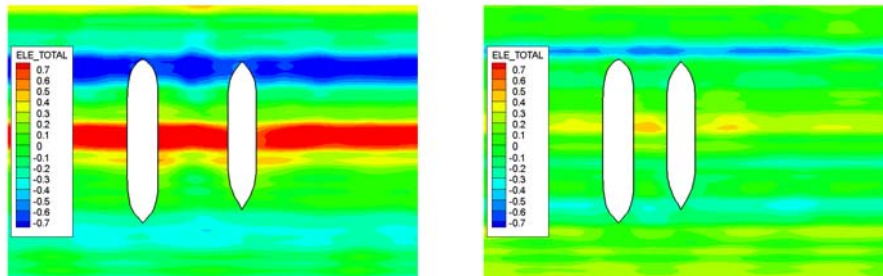
Fig. 5.34 Motion responses of the shuttle tanker during the berthing operation in irregular sea (Heading 180° , $V=2.0$ knots)



(a) $T_p=8.0$ s

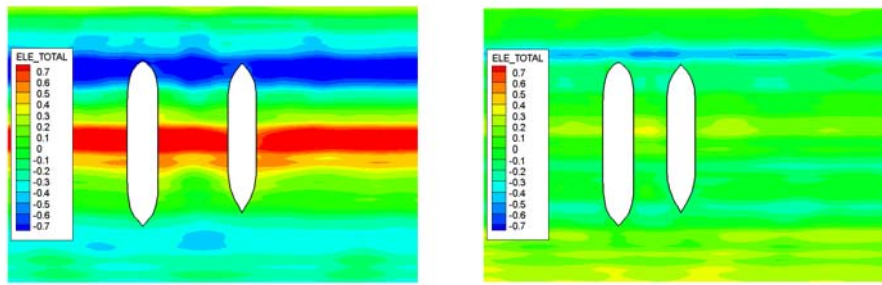


(b) $T_p=10.0$ s



(c) $T_p=12.0$ s

Fig. 5.35 Wave field around FPSO and shuttle tanker during the berthing operation in irregular sea (Gap=104 m(left), Gap=50 m(right))



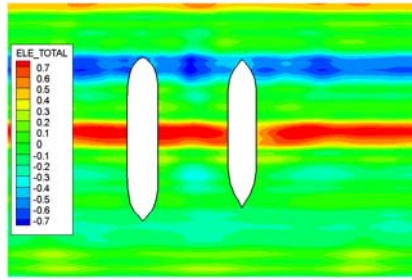
(d) $T_p=14.0$ s

Fig. 5.35 continued

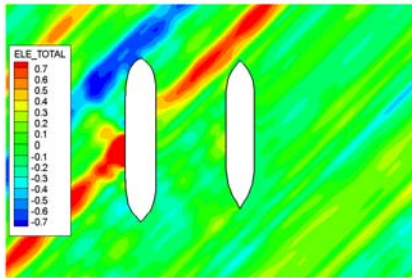
Fig. 5.35 shows the wave fields around the FPSO and the shuttle tanker during the berthing operation in irregular sea with four different peak periods. It is clearly observed that the wave length increases with an increase in the peak period. At the gap distance of around 104m, the two vessels encounter high waves, which results in a large heave motion, shown in Fig. 5.34.

5.4.2 Effect of wave heading

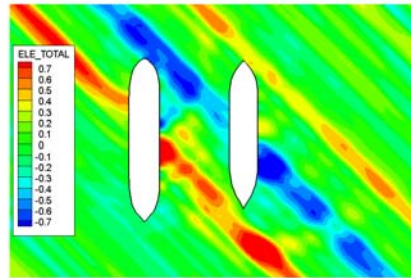
Fig. 5.36 shows snapshots of wave fields around the FPSO and shuttle tanker during the berthing operation in irregular sea with different wave headings. At this time, the gap distance is about 104 m. Since the random phases for irregular sea are the same for all wave headings, the wave patterns are quite similar regardless of headings. When the wave heading is 180 degree, the diffracted wave is not significant. Meanwhile, in the case of beam sea conditions, the diffracted wave around the two vessels is clearly observed.



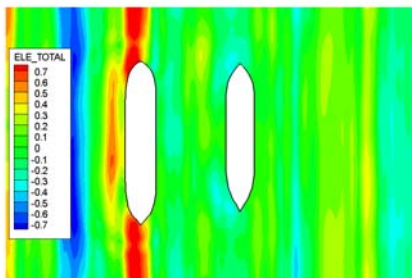
(a) Heading 180°



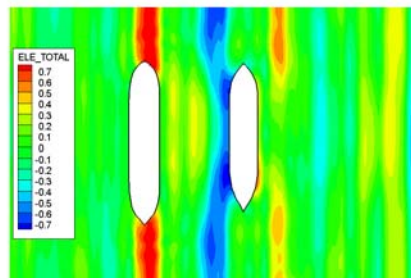
(b) Heading 225°



(c) Heading 135°

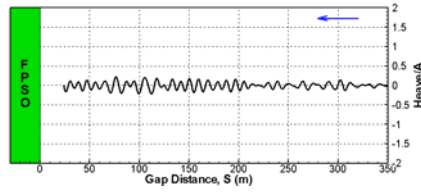


(d) Heading 270°

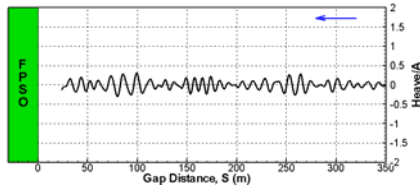


(e) Heading 90°

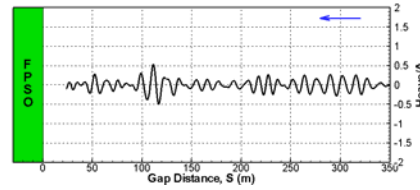
Fig. 5.36 Wave fields around FPSO and shuttle tanker during the berthing operation in irregular sea with different headings ($H_s=1.0$ m, $T_p=10.0$ s)



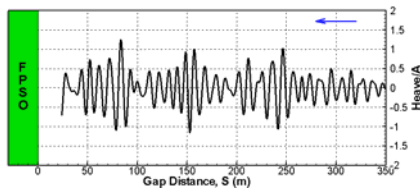
(a) Heading 180°



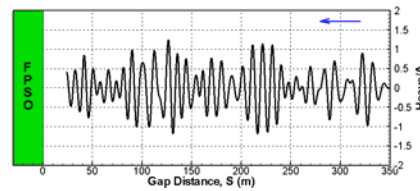
(b) Heading 225°



(c) Heading 135°



(d) Heading 270°

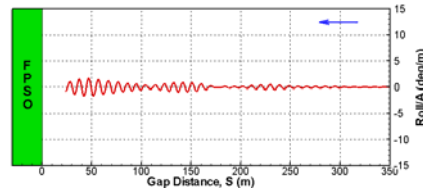


(e) Heading 90°

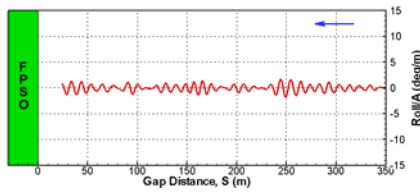
Fig. 5.37 Heave time series of the shuttle tanker during the berthing operation in irregular sea with different headings ($H_s=1.0$ m, $T_p=10.0$ s)

Fig. 5.37 and Fig. 5.38 show heave and roll time series during the berthing process in irregular sea with different wave headings, respectively. It is confirmed that wave height is a critical parameter for the wave-induced motion response. Under the beam sea conditions, the shuttle tanker experiences large heave and roll motions. When the heading is 90 degree, the heave amplitude reaches about 1.2 times of incident wave amplitude. At the

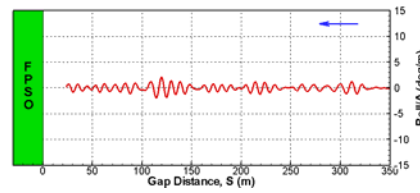
same time, roll amplitude is larger than 10° per unit wave amplitude. Amplitude motion is also found at the motion response under the beam sea conditions. In the case of head and bow quartering sea, heave and roll amplitude is less than 0.5 and 2° per unit wave amplitude, respectively.



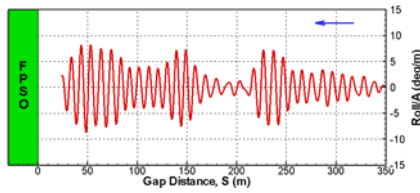
(a) Heading 180°



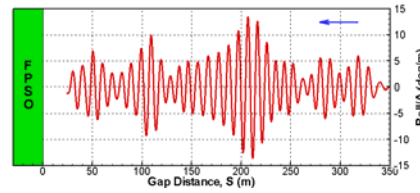
(b) Heading 225°



(c) Heading 135°



(d) Heading 270°



(e) Heading 90°

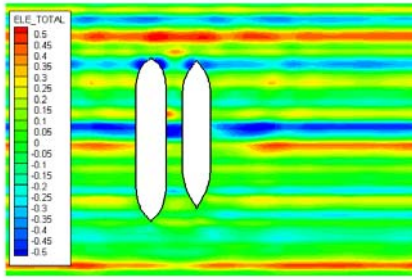
Fig. 5.38 Roll time series of the shuttle tanker during the berthing operation in irregular sea with different headings ($H_s=1.0$ m, $T_p=10.0$ s)

5.4.3 Effect of random seed

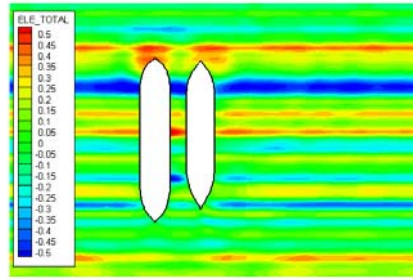
Irregular simulation results is depend on the random phase angles, which is normally function of the seed for random number generation. Fig. 5.39 shows six different wave fields for the berthing operation under the same wave conditions with different random seeds. It can be seen that the wave fields are quite different according to the given random seed. The cases of 'seed 4' and 'seed 6' shows high wave elevation.

Fig. 5.40 shows the heave time series of the shuttle tanker for the different random seeds. The amplitude change of the heave motion differ considerably despite the peak period and significant wave height being constant. The locations of the heave peaks change according to the incident wave. Maximum heave amplitude is less than 20% of incident wave amplitude for all random seed cases.

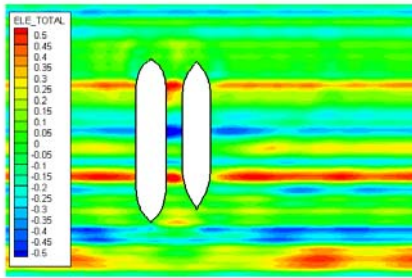
Fig. 5.41 shows the time series of the roll motions of the shuttle tanker for various random seeds. Roll motion also shows rather different trends for the considered random seeds. However, maximum roll amplitude is about 2° per unit wave amplitude for all cases.



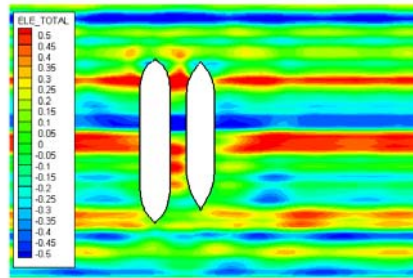
(a) Seed 1



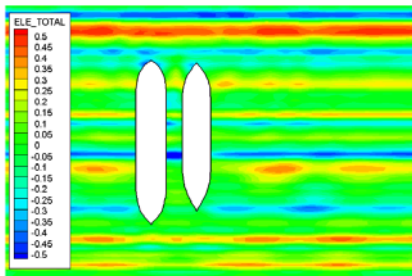
(b) Seed 2



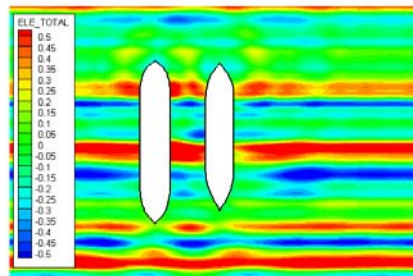
(c) Seed 3



(d) Seed 4

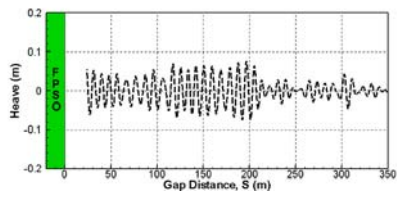


(e) Seed 5

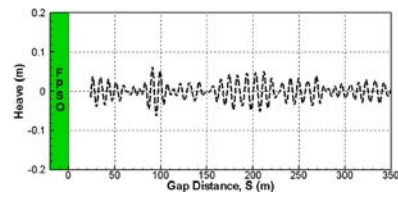


(f) Seed 6

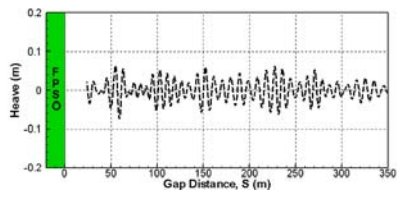
Fig. 5.39 Wave fields around FPSO and shuttle tanker during the berthing operation with different random seed (Heading 180° , $H_s=1.0\text{m}$, $T_p=8.0\text{ s}$)



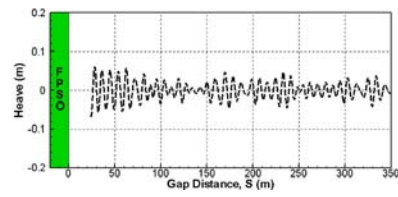
(a) Seed 1



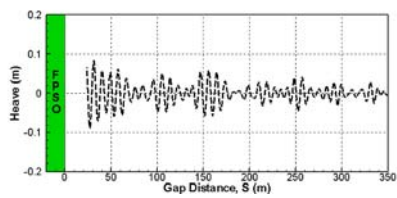
(b) Seed 2



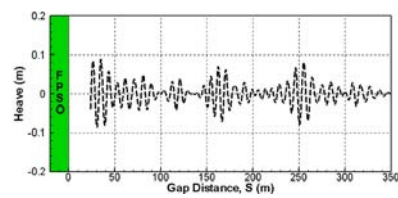
(c) Seed 3



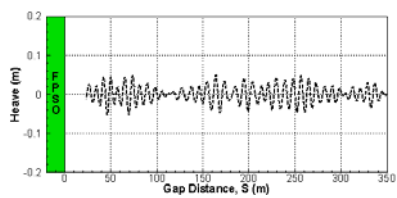
(d) Seed 4



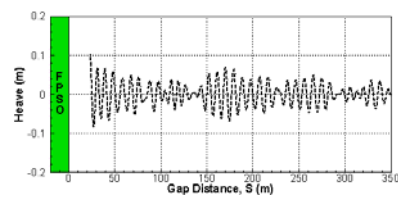
(e) Seed 5



(f) Seed 6

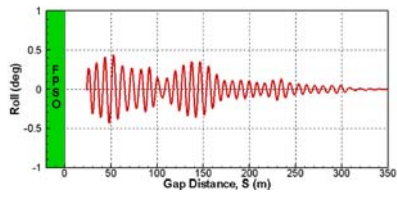


(g) Seed 7

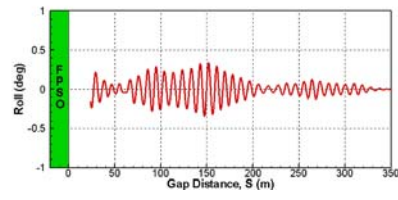


(h) Seed 8

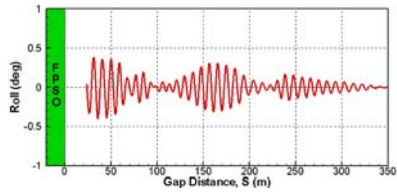
Fig. 5.40 Heave time series of the shuttle tanker during the berthing operation in irregular sea with different random seeds ($H_s=1.0\text{m}$, $T_p=8.0\text{m}$)



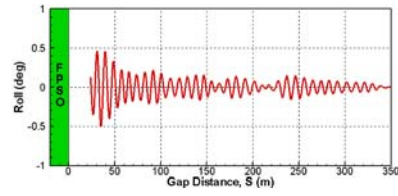
(a) Seed 1



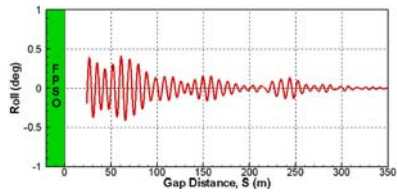
(b) Seed 2



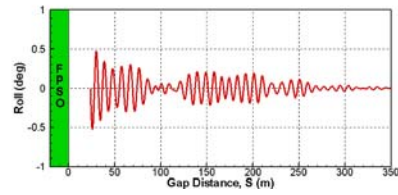
(c) Seed 3



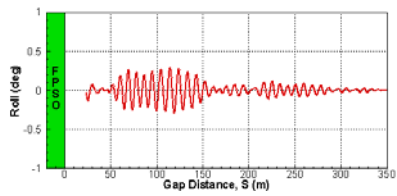
(d) Seed 4



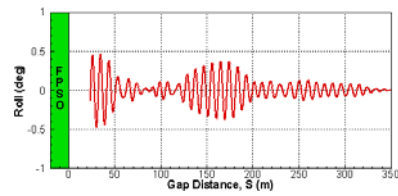
(e) Seed 5



(f) Seed 6



(g) Seed 7



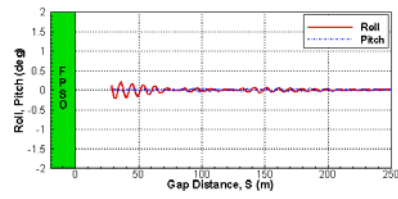
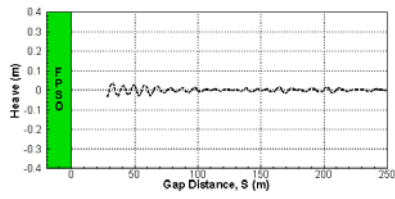
(h) Seed 8

Fig. 5.41 Roll time series of the shuttle tanker during the berthing operation in irregular sea with different random seeds ($H_s=1.0\text{m}$, $T_p=8.0\text{m}$)

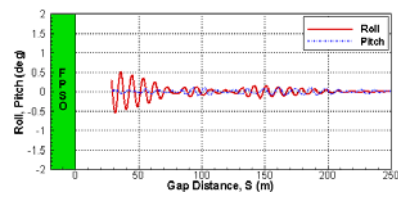
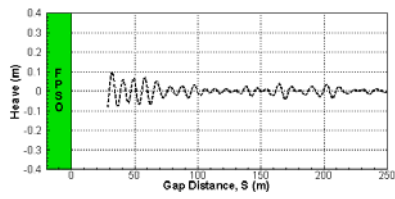
5.4.3 Effect of wave height

Fig. 5.42 shows the motion response of the shuttle tanker during the berthing operation at different significant wave heights. When the significant wave height is 0.2 m, the heave response is less than 0.1m and the angular motion is less than 0.5 deg. With an increase in the significant wave height, the motion responses of the shuttle tanker obviously increase. When the significant wave height is 1.0m, the maximum roll of the shuttle tanker becomes 1.0 degree.

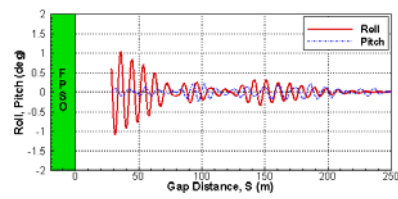
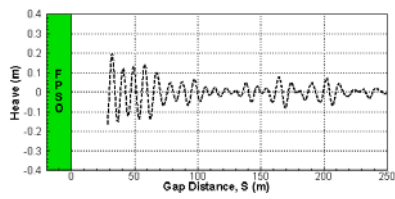
Fig. 5.43 shows the maximum motion responses of the shuttle tanker during the berthing operation at various wave periods and wave height conditions. The considered wave height ranges from 0.2 m to 1.5m, and the considered peak period ranges from 6.0 s to 14.0 s. The heave response increases with increasing peak period. The maximum heave of the shuttle tanker is about 0.4m and occurs when the peak period is 14.0 s and significant wave height is 1.5m. The maximum roll of about 1.6 degree occurs when the peak period is 10.0 s.



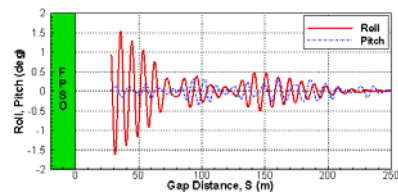
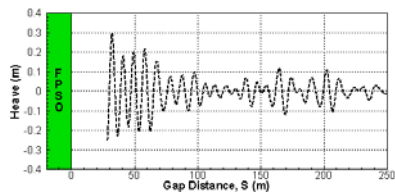
(a) $T_p=8.0$ s, $H_s=0.2$ m



(b) $T_p=10.0$ s, $H_s=0.5$ m

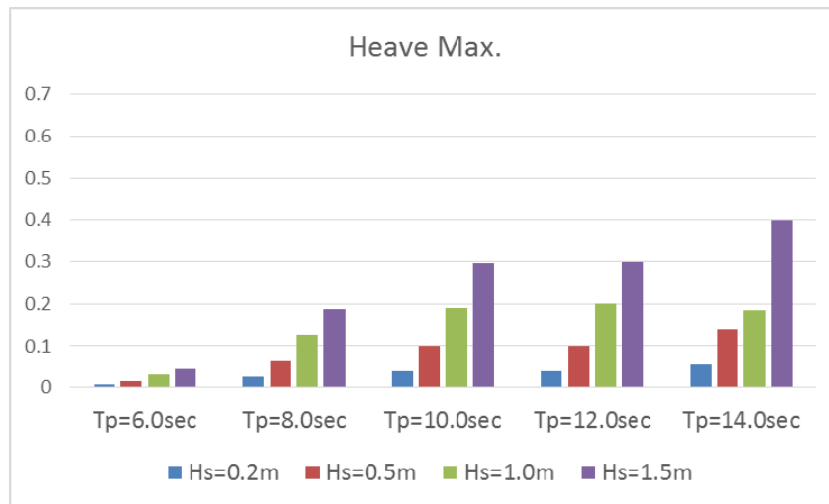


(c) $T_p=12.0$ s, $H_s=1.0$ m

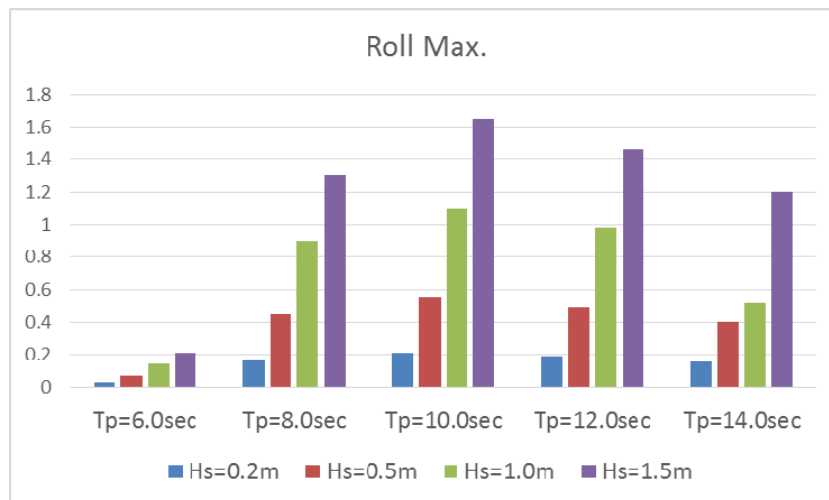


(d) $T_p=14.0$ s, $H_s=1.5$ m

Fig. 5.42 Motion responses of the shuttle tanker during the berthing operation in irregular sea (Heading 180 deg., $V=2.0$ knots)



(a) Heave.



(b) Roll

Fig. 5.43 Maximum motion responses of the shuttle tanker during the berthing operation in irregular sea with different wave heights

Chapter 6. Conclusions

In this study, the berthing problems between two floating bodies are numerically investigated with a focus on hydrodynamic forces acting on the vessels and wave-induced motion responses. A numerical method has been developed based on finite element method and an efficient re-mesh algorithm. Following is a summary of the study, the findings, and the above discussions:

- 1) The theoretical formulation of the berthing problem is presented based on the potential flow and with respect to earth-fixed coordinate system. The exact and linear boundary value problems are derived by applying perturbation series expansion. The formulation for the hydrodynamic force including the acceleration potential is also presented.
- 2) A numerical method for solving the berthing problem based on the finite element method in the time domain has been developed. An efficient re-mesh algorithm is proposed for the solution. The concept of local and global mesh is employed in the algorithm, and the re-mesh process is replaced by a simple connection operation. The proposed numerical method is validated by comparing its solutions with frequency-domain results.
- 3) Berthing response in head sea: The two vessels involved in the berthing operation interact strongly with each other through the gap

flow. Strong transverse wave forces are generated by the gap resonant wave when the two vessels closely approach each other. The time series of the wave force during the berthing operation shows amplitude change, which is due to the continuously changing relative positions of the two vessels. As the berthing speed increase, the motion of the berthing vessel become simpler and smaller. Fairly good agreement is observed between the results of the proposed numerical method and those of experiments.

- 4) Berthing response in quartering and beam seas: It is shown that the sheltering effect significantly reduces the hydrodynamic force and wave-induced motion responses when the wave angle is opposite to the berthing direction. Conversely, if the berthing vessel is directly exposed to the incident wave, it would experience a large roll motion and strong repulsive sway drift force. On the other hand, strong amplitude modulation of force and motion time series can be observed for berthing in beam and quartering sea. The FFT results demonstrates that these amplitude modulation are mainly caused by the two different components of encounter frequencies, which are resulted from the interaction between moving vessel and disturbed wave fields.
- 5) Berthing response in irregular sea: It is confirmed that wave height and wave heading are critical parameters for the berthing operation. The peak period significantly affects the roll motion of the vessel, and it is particularly observed that the berthing response in irregular

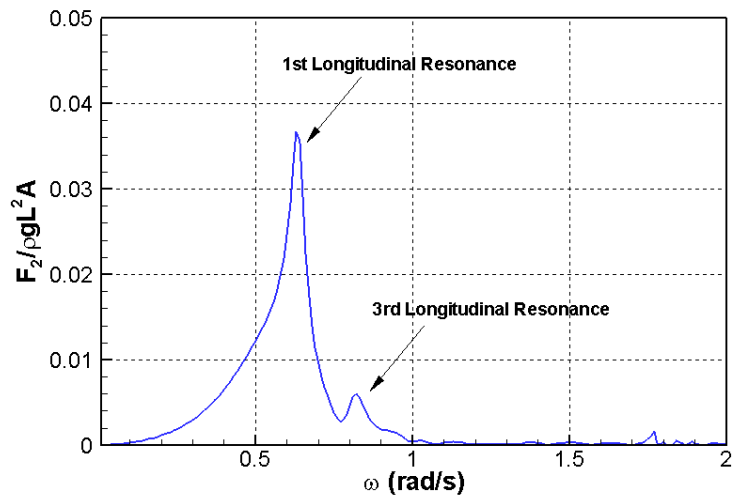
sea is quite different from statistical data for different random seeds. This can be attributed to the fact that berthing is a transient event that occurs over a finite period.

Appendix A. Gap resonance between two barges

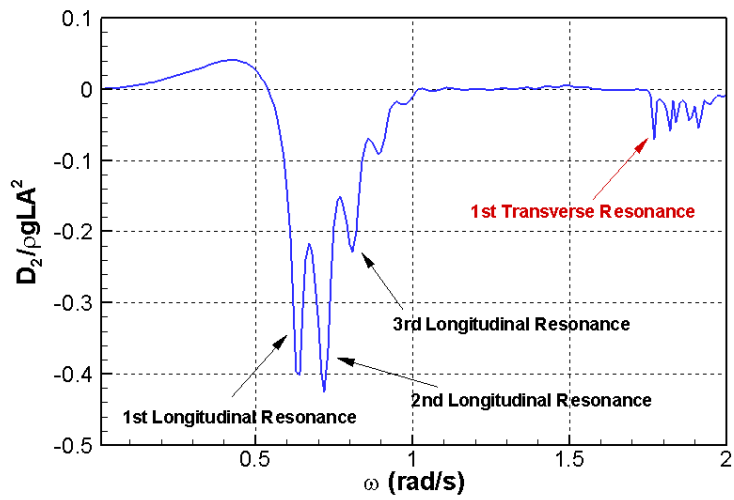
It is well known that gap resonance occurs between multiple floating bodies in side-by-side configuration. During a berthing operation, the berthing barge may pass several gap resonant locations, and this makes it necessary to predict the resonance frequency and locations along the berthing path. In this appendix, the gap resonant conditions and force response between two barges are numerically investigated using a frequency-domain diffraction code based on the higher-order boundary element method (Choi et al., 2001).

Fig. A.1 shows the sway wave forces acting on the two rectangular barges for a gap of 20 m. Each of the barges is 150 m (L) \times 40 m (B) \times 10 m (D). It can be observed that the several peak responses in both the sway excitation and drift forces are caused by the gap resonance. While the sway wave excitation force clearly exhibits first and third longitudinal resonances, the sway mean drift forces have a total of four resonance peaks including that of the lateral resonance. The absence of the second longitudinal resonance from the sway excitation force is due to the fact that the one-wavelength resonance results in the total force summation along the hull are not significant.

Fig. A.2 shows the wave fields under three longitudinal resonance conditions. The first and second resonances correspond to the half- and one-wavelength resonances, respectively. A high wave elevation can be observed in the region of the gap between the barges. Due to the open boundary, both ends of the gap in the longitudinal direction become node points.

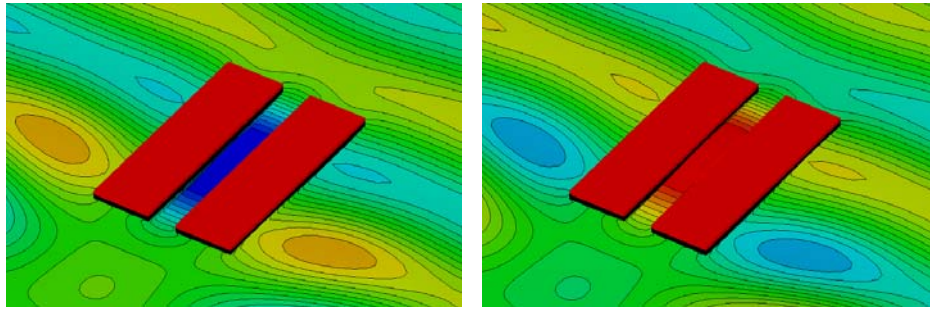


(a) Sway wave excitation forces

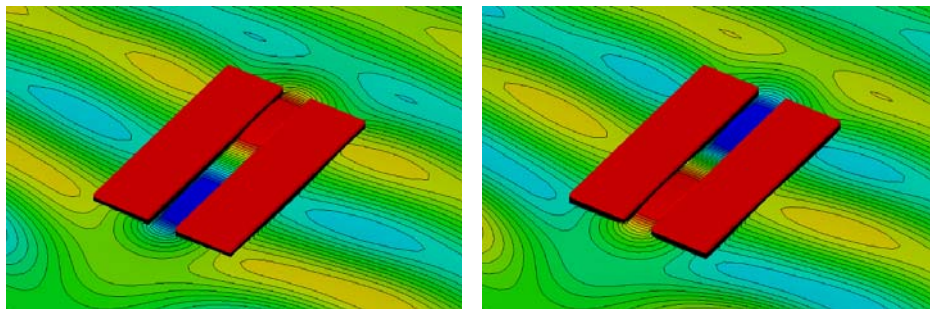


(b) Sway wave mean drift forces

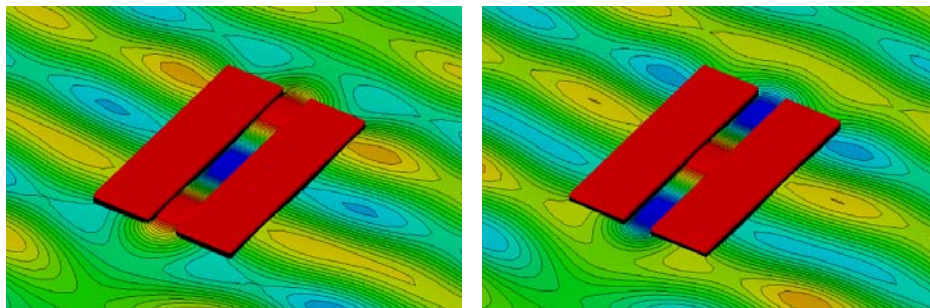
Fig. A.1 Sway wave forces acting on the two rectangular barges in head sea
(S=20 m)



(a) 1st longitudinal resonance ($\omega = 0.64$ rad/s)



(b) 2nd longitudinal resonance ($\omega = 0.72$ rad/s)



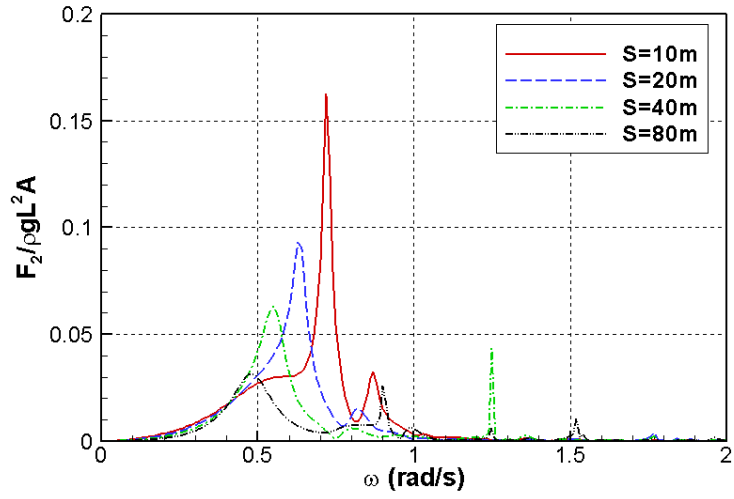
(c) 3rd longitudinal resonance ($\omega = 0.81$ rad/s)

Fig. A.2 Wave fields around barges in head sea under longitudinal resonant conditions (S=20 m)

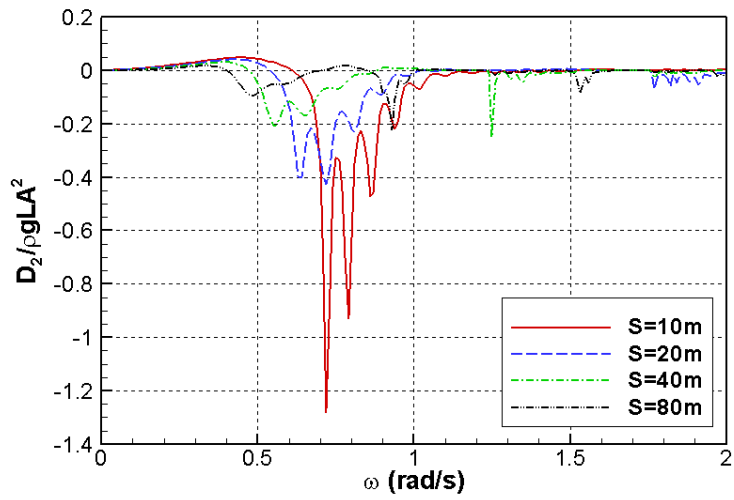
Fig. A.3 shows the effect of the gap distance on the gap resonance with respect to the sway wave forces. In the figure, 'S' denotes the gap between the two barges. As the gap increases, the first resonant point shifts to the low-frequency range, and the peak values of the sway forces also decrease. The second and third peaks of the sway drift force also indicate the shift of the peak frequency and reduction of the peak values with increasing gap. Figs. A.4 and A.5 show the wave fields at the first and second resonant frequencies for various gaps. It can be seen that the resonant wave amplitudes in the gap dramatically decrease with increasing gap.

Fig. A.6 shows the sway drift force contours with respect to the gap and wave frequency. It can be clearly observed that a strong repulsive force acts on the barge at the first resonant frequency. As the gap increases, the peak frequency slightly decreases. The second and third resonances are also shown in the figure.

Fig. A.7 shows the first resonant frequency based on the present frequency-domain results. For the comparison, the predictions of Molin's analytical formula are also plotted. Good agreement can be observed between the two results.

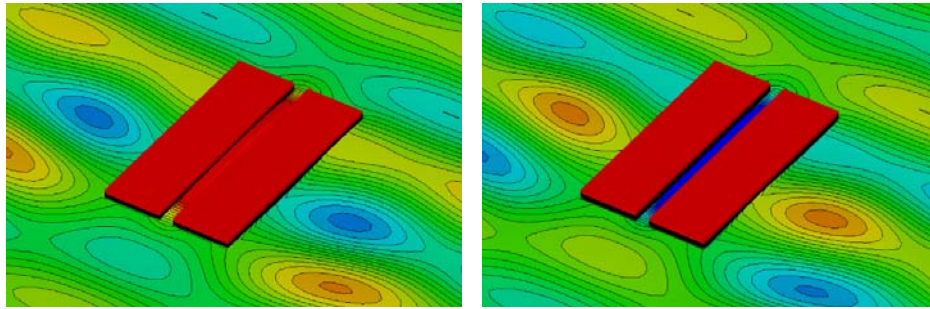


(a) Sway wave excitation forces

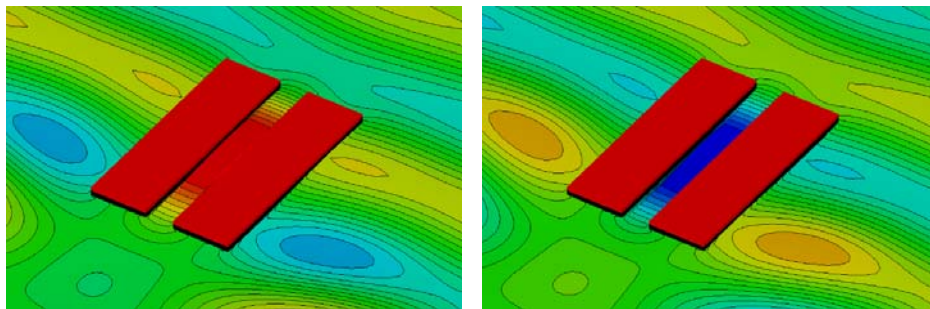


(b) Sway wave mean drift forces

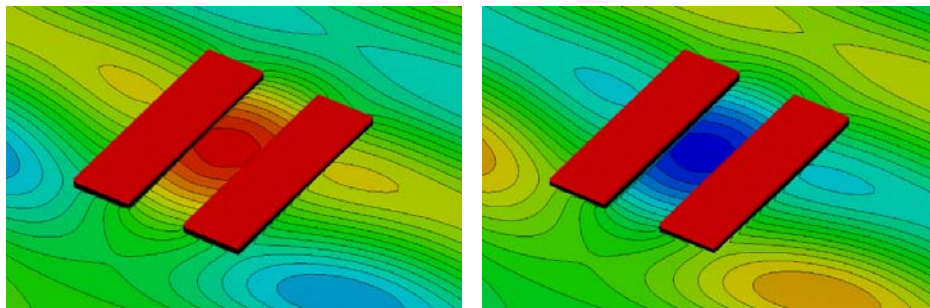
Fig. A.3 Effect of gap distance on sway wave forces acting on the barges



(a) $S=10$ m, $\omega = 0.72$ rad/s

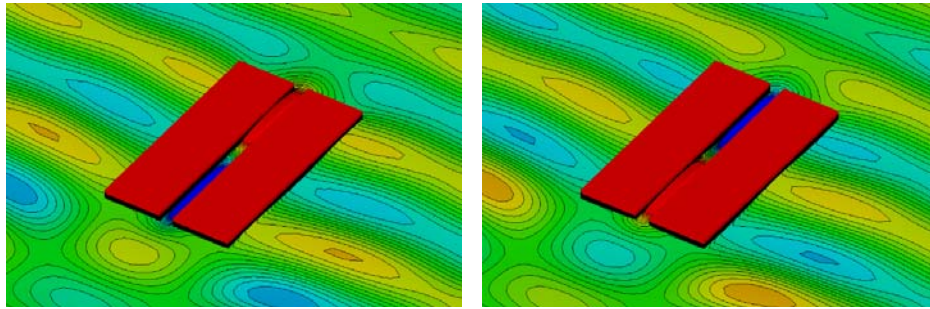


(b) $S=20$ m, $\omega = 0.64$ rad/s

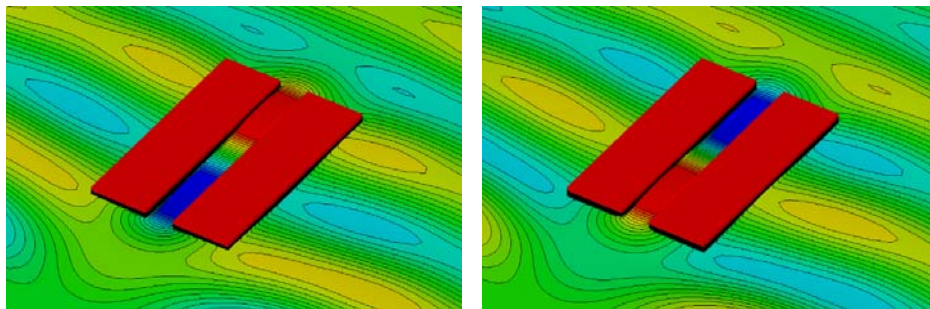


(c) $S=30$ m, $\omega = 0.55$ rad/s

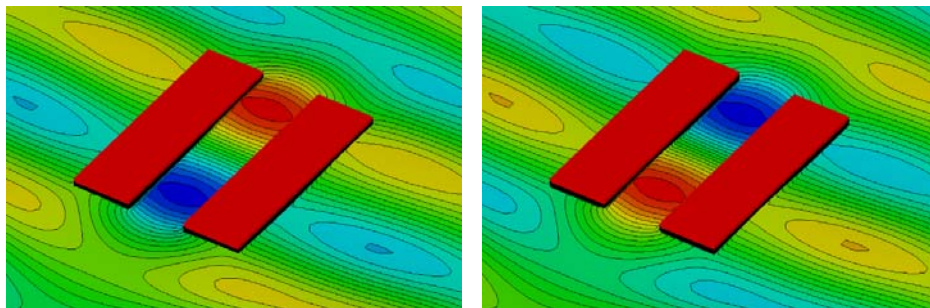
Fig. A.4 Effect of gap distance on the wave fields under the first longitudinal gap resonant conditions



(a) $S=10$ m, $\omega = 0.79$ rad/s



(b) $S=20$ m, $\omega = 0.72$ rad/s



(c) $S=30$ m, $\omega = 0.65$ rad/s

Fig. A.5 Effect of gap distance on the wave fields under the second longitudinal gap resonant conditions

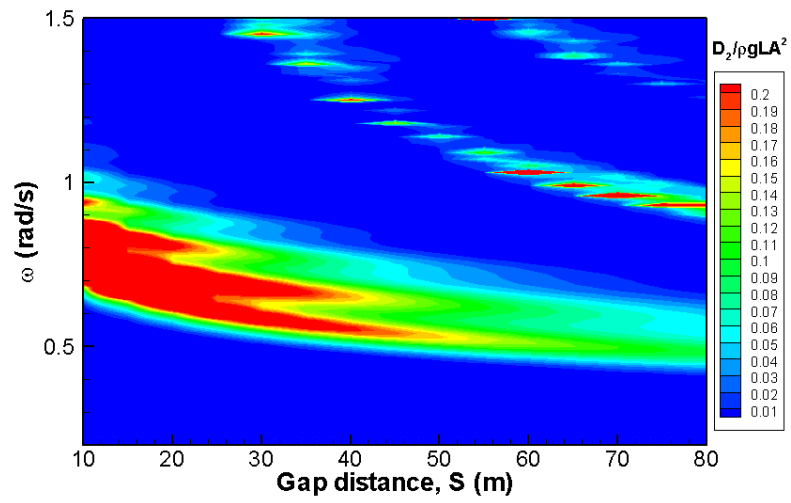


Fig. A.6 Sway mean drift force contours

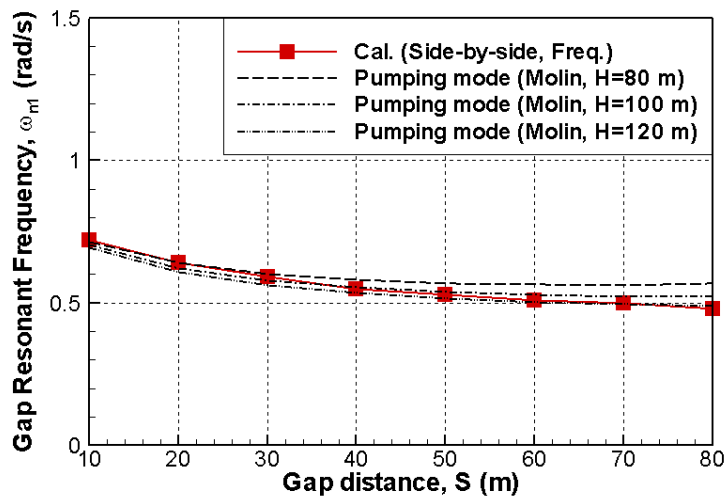
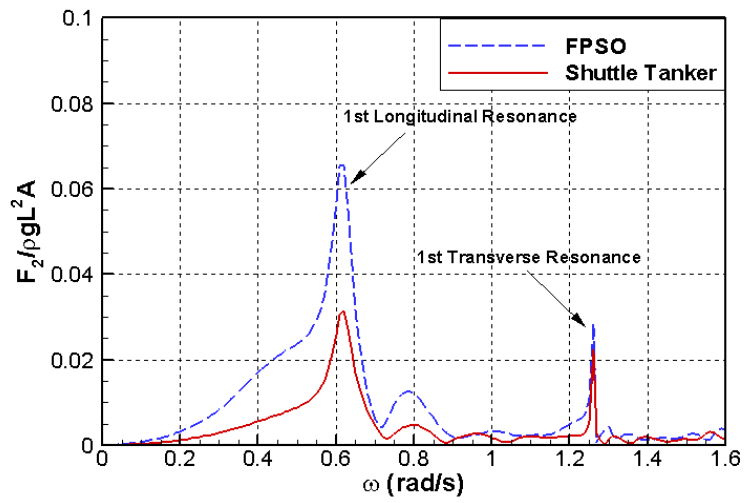


Fig. A.7 Gap resonance frequency based on frequency-domain solutions

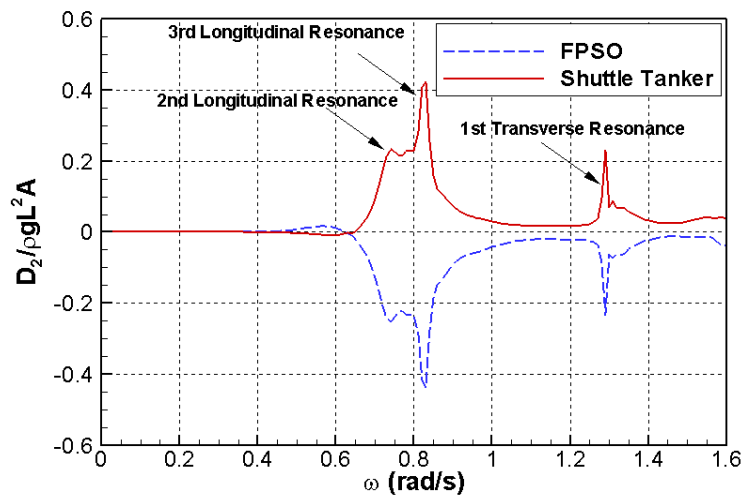
Appendix B. Gap resonance between FPSO and shuttle tanker

Fig. B.1 shows the sway wave forces acting on an FPSO unit and a shuttle tanker in side-by-side configuration with a gap of 20 m. The first longitudinal and transverse resonance frequencies can be determined from the sway wave excitation force. The sway drift force in Fig. B.1(b) clearly shows the second and third longitudinal resonances. Owing to the relative sizes of the barges, the sway excitation force acting on the FPSO unit is larger than that acting on the shuttle tanker. The two barges were, however, subjected to the same magnitude of sway mean drift force acting outward from the gap.

Fig. B.2 shows the wave fields under three longitudinal resonance conditions. The first and second resonances correspond to the half- and one-wavelength resonances, respectively. A high wave elevation can be observed in the region of the gap between the barges. The third longitudinal resonance corresponds to the one- and half-wavelength resonance in the gap.

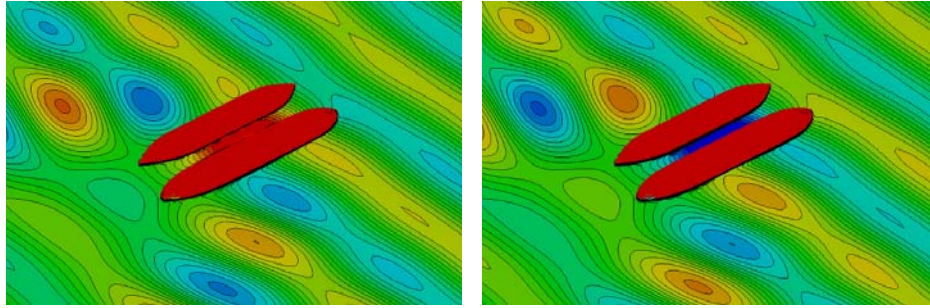


(a) Sway wave excitation forces

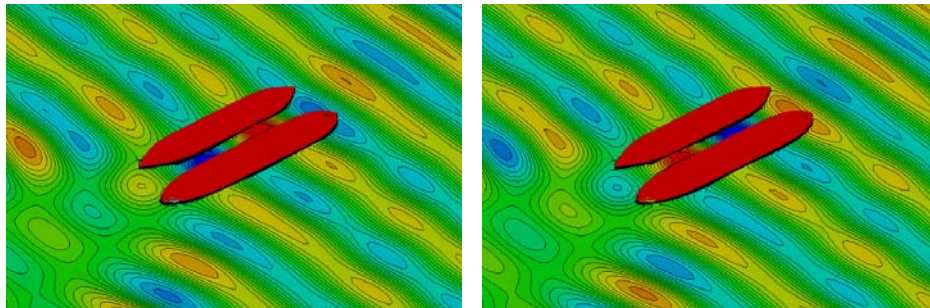


(b) Sway wave mean drift forces

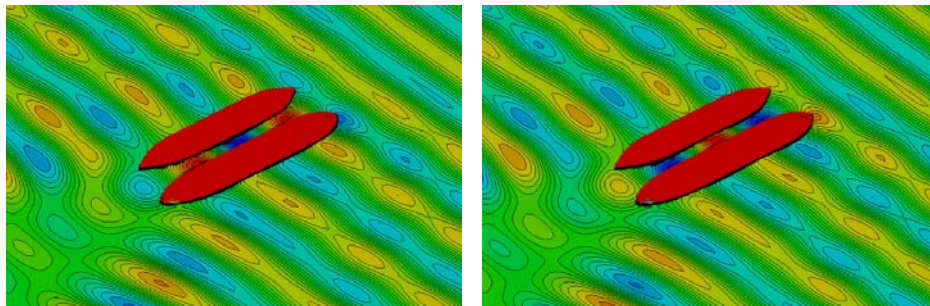
Fig. B.1 Sway wave forces acting on the FPSO and shuttle tanker in head sea
($S=20$ m, L =length of the FPSO)



(a) 1st longitudinal resonance ($\omega = 0.62$ rad/s)



(b) 2nd longitudinal resonance ($\omega = 0.74$ rad/s)



(c) 3rd longitudinal resonance ($\omega = 0.79$ rad/s)

Fig. A.2 Wave fields around the FPSO and shuttle tanker in head sea under longitudinal resonant conditions (S=20 m)

Appendix C. Sheltering zone in regular waves

The hydrodynamic interaction between multiple floating bodies in a quartering or beam sea can be interpreted as the sheltering effect. The presence of the adjacent bodies affects the hydrodynamic force acting on any one of the bodies. A floating body on the weather side of a particular body acts as a breakwater, while one on the lee side acts as a quay (Hong et al., 2005). When a berthing barge approaches through an area behind the lee side of a stationary structure, the barge is subjected to reduced hydrodynamic force owing to the sheltering effect of the stationary structure. Fig. C.1 shows the sheltering and reflection zone around the single barge for various wave headings. In the figure, “sheltering zone” is the area in which the wave amplitude is less than 80% of the incident wave amplitude. “Reflection zone” is the area in which the wave amplitude is larger than 1.2 times the incident wave amplitude. Basically, the sheltering zone is located in the opposite direction of the incident wave heading. Under head sea conditions, the sheltering zone is located behind the barge. When the wave heading is 90° , the sheltering zone is located on the portside of the barge.

Fig. C.2 shows the effect of the wave frequency on the size of the shielding zone. As can be observed, the sheltering zone is largest for wave frequencies ranging between 0.45 and 0.55 rad/s. When the wave frequency exceeds 0.55 rad/s, it can be seen that the sheltering zone moves far away from the barge. However, when the wave frequency falls below 0.45 rad/s, the sheltering zone becomes smaller and moves to the portside of the barge.

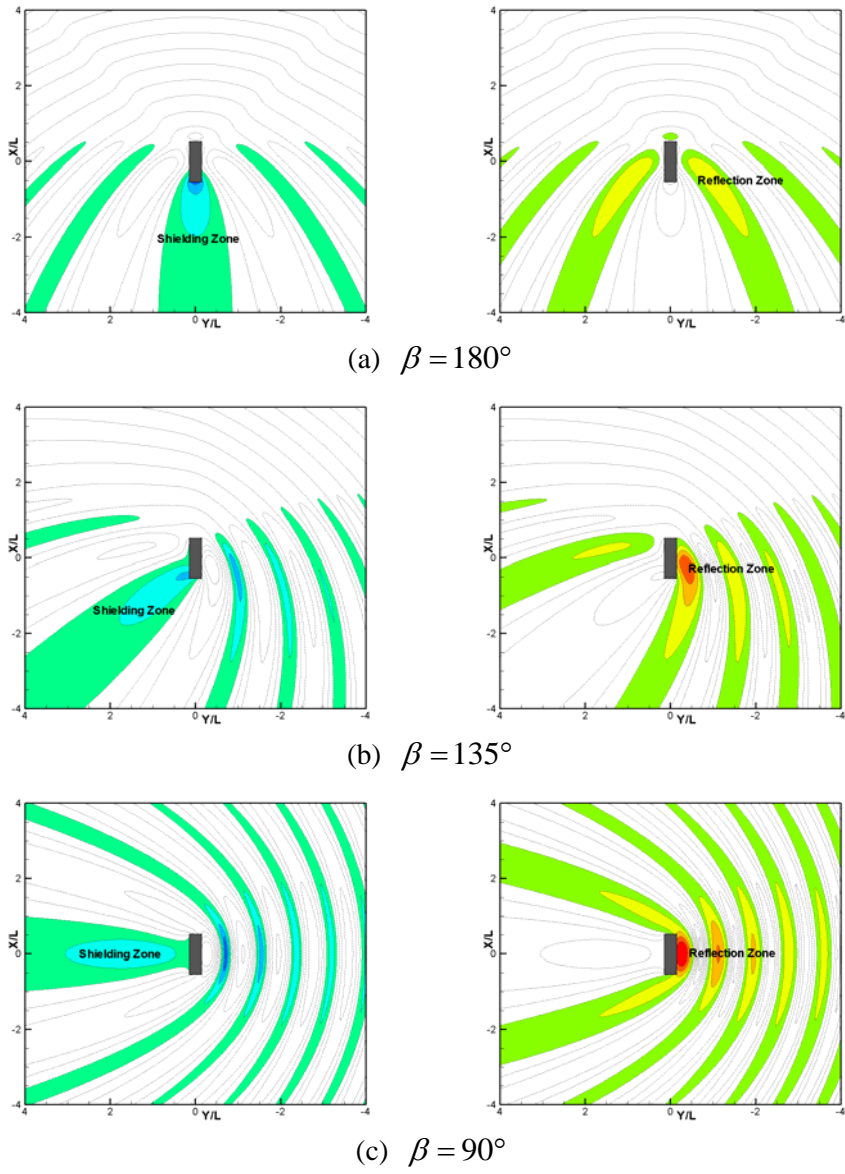
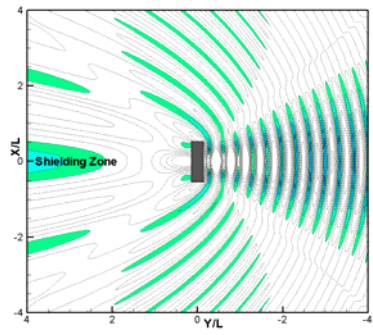
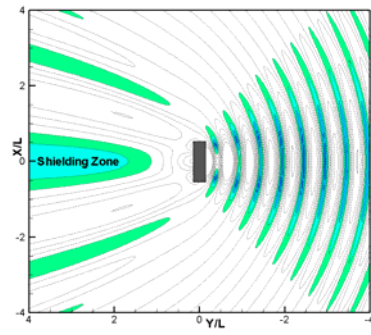


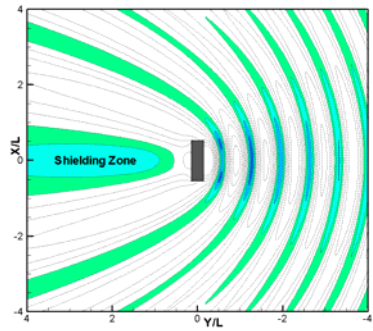
Fig. C.1 Sheltering and reflection zone around single barge under various wave headings ($\omega = 0.50 \text{ rad/s}$, $\lambda/L=1.65$)



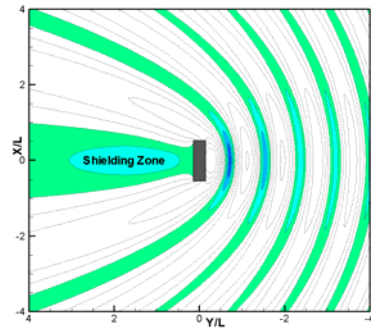
(a) $\omega = 0.78$ rad/s, $\lambda/L=0.68$



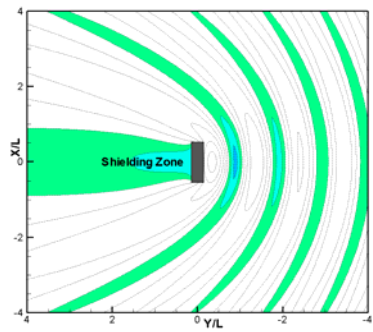
(b) $\omega = 0.64$ rad/s, $\lambda/L=1.00$



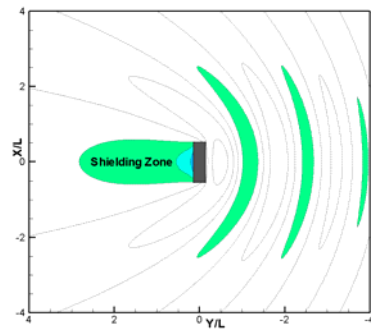
(c) $\omega = 0.55$ rad/s, $\lambda/L=1.36$



(d) $\omega = 0.50$ rad/s, $\lambda/L=1.65$



(e) $\omega = 0.45$ rad/s, $\lambda/L=2.03$



(f) $\omega = 0.39$ rad/s, $\lambda/L=2.69$

Fig. C.2 Sheltering zone around single barge under various wave frequencies
($\beta = 90^\circ$)

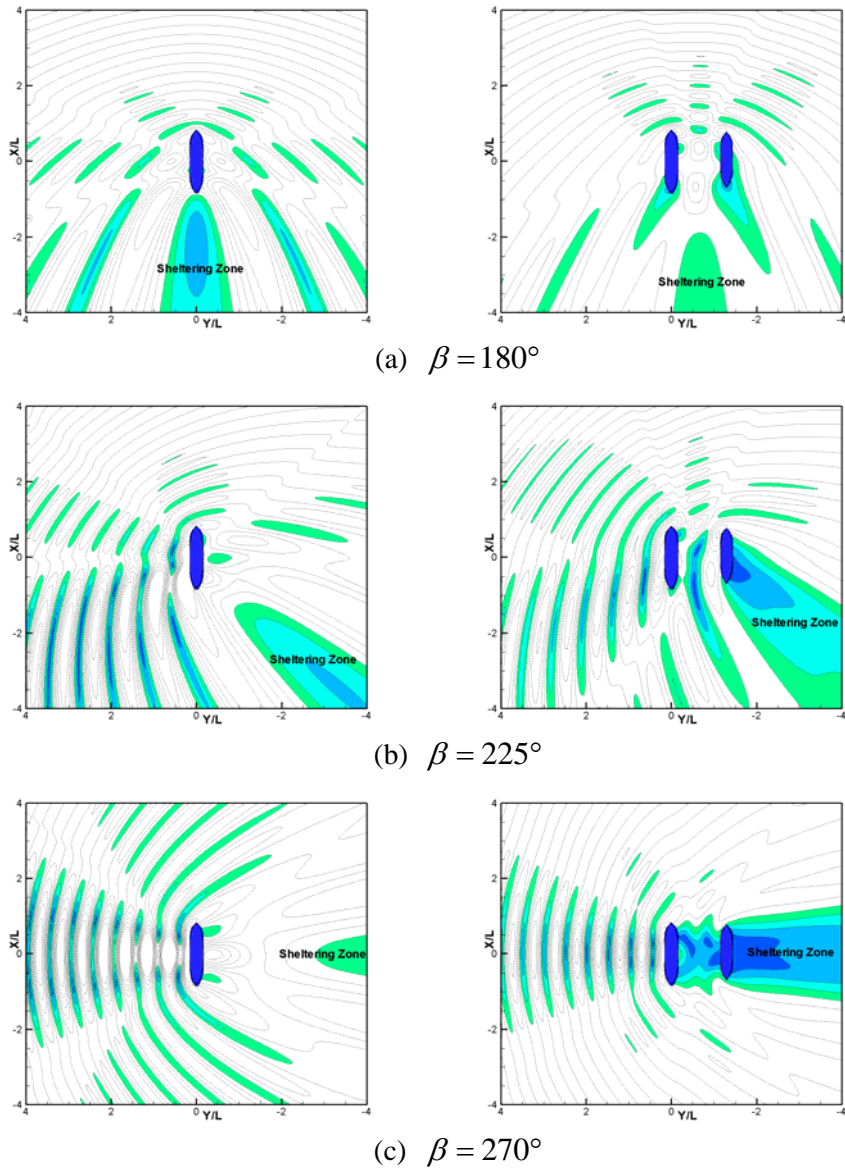


Fig. C.3 Sheltering zone around FPSO only (left) and FPSO with shuttle (right) under various wave frequencies ($\omega = 0.64 \text{ rad/s}$, $\lambda = 150 \text{ m}$)

Bibliography

- [1] Bai, K.J., Yeung, R.W., 1974, “Numerical Solutions to Free-Surface Flow Problems”, The 10th Symposium on Naval Hydrodynamics, Office of Naval Research, MIT, Cambridge, Mass., USA
- [2] Bai, K.J., 1975, “Diffraction of Oblique Waves by an Infinite Cylinder”, Journal of Fluid Mechanics, 68, 513-535
- [3] Bai, K.J., 1977, “The Added Mass of Two-Dimensional Cylinders Heaving in Water of Finite Depth”, Journal of Fluid Mechanics, 81, 85-105
- [4] Bai, K.J., 1981, “A localized Finite-Element Method for Three Dimensional Ship Motion Problems”, The 3rd International Conference on Numerical Ship Hydrodynamics, Paris, France
- [5] Bai, K.J., Kim, J.W., Kim, Y.H., 1989, “Numerical Computations for a Nonlinear Free Surface Flow Problem”, Proc. 5th Int. Conf. on Numerical Ship Hydrodynamics, Hiroshima, Japan, 403-418
- [6] Buchner, B., Dijk, A., Wilde, J., 2001, “Numerical Multiple-Body Simulations of Side-by-Side Mooring to an FPSO”, Proceedings of the 11th International Offshore and Polar Engineering Conference (ISOPE-2001), Stavanger, Norway, 343-353
- [7] Buchner, B., Dierx, P., Waals, O., 2005, “The Behaviour of Tugs in Waves Assisting LNG Carriers during Berthing along Offshore LNG Terminals”, Proceedings of the 24th International Conference on Offshore Mechanics and Arctic Engineering, Halkidiki, Greece, OMAE2005-67219
- [8] Cho, S.K., Sung, H.G., Hong, S.Y., Hong, S.W., Kim, Y.S., Ha, M.K., Choi,

- Y.D., Yu, B.S., Jang, R.D., Choi, H.S., 2011, "Experimental Study on the Effect of Sloshing on Side-by-Side moored FSRU and LNGC", Proceedings of the 21th International Offshore and Polar Engineering Conference (ISOPE-2011), Maui, Hawaii, USA, 144-151
- [9] Doorn, J.T.M. and Hove, D., 2002, "F(P)SO Offloading Concepts, their Nautical Feasibility and Safety Assessment", Offshore Technology Conference (OTC-2002), Houston, Texas, USA, OTC 14296
- [10] Fournier, J.R., Naciri, M., Chen, X.B., 2006, "Hydrodynamics of two side-by-side vessels Experiments and numerical simulations", Proceedings of the 16th International Offshore and Polar Engineering Conference (ISOPE 2006), San Francisco, California, 158-165
- [11] Hansen, H.F., Carstensen, S., Christensen, E.D., Kirkegaard, J., 2009, "Multi Vessel Interaction in Shallow Water", Proceedings of 28th International Conference on Offshore Mechanics and Arctic Engineering, Honolulu, Hawaii, USA (OMAE2009-79161)
- [12] Hong, S.Y., Kim, J.H., Cho, S.K., Choi, Y.R., Kim, Y.S., 2005, "Numerical and experimental study on hydrodynamic interaction of side-by-side moored multiple vessels", Ocean Engineering, 32, 783-801
- [13] Hong, S.Y., Kim, J.H., Kim, H.J., Choi, Y.R., 2002, "Experimental Study on Behavior of Tandem and Side-by-side Moored Vessels", Proceedings of the 12th International Offshore and Polar Engineering Conference (ISOPE-2002), Kitakyushu, Japan, 841-847
- [14] Hong, S.Y., Nam, B.W., 2011, "Analysis of 2nd-order Wave Force on Floating Bodies Using FEM in Time Domain", International Journal of

Offshore and Polar Engineering, 21, 22-28

- [15] Huaming, W., Xie, Y., He, Z.Z.W., 2011, "Numerical Study on Viscous Hydrodynamic Forces Acting on a Berthing Tanker Model", Proceedings of the 21th International Offshore and Polar Engineering Conference (ISOPE-2011), Maui, Hawaii, USA, 596-600
- [16] Huang, E.T., Chen H.C., 2003, "Ship Berthing at a Floating Pier", Proceedings of the 13th International Offshore and Polar Engineering Conference (ISOPE-2003), Honolulu, Hawaii, USA, 683-690
- [17] Huijsmans, R.H.M., Pinkster, J.A., Wilde, J.J., 2001, "Diffraction and Radiation of Waves Around Side-by-Side Moored Vessels", Proceedings of the 11th International Offshore and Polar Engineering Conference (ISOPE-2001), Stavanger, Norway, 406-412
- [18] Inoue, Y., Ali, M.T., 2003, "A Numerical Investigation on the Behaviour of Multiple Floating Bodies of Arbitrary Arrangements in Regular Waves", Proceedings of the 13th International Offshore and Polar Engineering Conference (ISOPE-2003), Honolulu, Hawaii, USA, 558-565
- [19] Kashiwagi, M., Endo, K., Yamaguchi, H., 2005, "Wave drift forces and moments on two ships arranged side by side in waves", Ocean Engineering, 32, 529-555
- [20] Kim, J.W., Kyoung, J.H., Ertekin, R.C., Bai, K.J., 2003, "Wave Diffraction of Steep Waves by Bottom-mounted Vertical Cylinder", Proceedings of 22th International Conference on Offshore Mechanics and Arctic Engineering (OMAE 2003), Cancun, Mexico
- [21] Kim, M.S., Ha, M.K., Kim, B.W., 2003, "Relative Motions between

- LNG-FPSO and Side-by-Side positioned LNG Carrier in Waves”, Proceedings of the 13th International Offshore and Polar Engineering Conference (ISOPE-2003), Honolulu, Hawaii, USA, 210-217
- [22] Kong, G.Y., Lee, Y.S., Lee, S.M, 2004, “A Study on the Modeling of Transitional Lateral Force Acting on the Berthing Ship by CFD”, KSME International Journal, 18, 7, 1196-1202
- [23] Koo, B.J., Kim, M.H., 2005, “Hydrodynamic interactions and relative motions of two floating platforms with mooring lines in side-by-side offloading operation”, Applied Ocean Research, 27, 292-310
- [24] Kyoung, J.H., Kim, J.W., Bai, K.J., 2003, “Nonlinear Free Surface Flows around Three Dimensional Transom Stern”, The 8th International Conference on Numerical Ship Hydrodynamics, Busan, Korea, 1, 22-25
- [25] Lataire, E., Vantorre, M., Delefortrie, G., Candries, M., 2012, “Mathematical modelling of forces acting on ships during lightering operations”, Ocean Engineering, 55, 101-115
- [26] Lataire, E., Vantorre, M., Vandenbroucke, J., Eloot, K., 2011, “Ship to Ship Interaction Forces during Lightering Operations”, 2nd International Conference on Ship Manoeuvring in Shallow and Confined Water : Ship to Ship Interaction, 212-221
- [27] Naciri, M., Waals, O., Wilde, J., 2007, “Time Domain Simulations of Side-by-Side Moored Vessels Lessons Learnt from a Benchmark Test”, Proceedings of 26th International Conference on Offshore Mechanics and Arctic Engineering, San Diego, California, USA (OMAE2007-29756)
- [28] Nam, B.W., Sung, H.G., Hong, S.Y., 2009, “Time Domain Analysis of

- Ship Motion in Waves Using Finite Element Method”, *Journal of Ocean Engineering and Technology*, 23, 16-23
- [29] Park, J.J., Seo, J.H., Kim, M., Kim, B.W., Suh, Y.S., 2013, “Coupled Sloshing and Motion Analysis of FLNG in Side-by-Side Arrangement”, *Proceedings of the 23rd International Offshore and Polar Engineering Conference (ISOPE-2013)*, Anchorage, Alaska, USA, 350-356
- [30] Sakakibara, S., Wakabayashi, M., Shimada, K., Yamaguchi, H., 2005, “Simulation Program for Berthing and Mooring of Two Vessels in Consideration of Exact Hydrodynamic Interactions”, *Proceedings of 24th International Conference on Offshore Mechanics and Arctic Engineering*, Halkidiki, Greece, OMAE2005-67457
- [31] SaSa, K., Hibino, T., Kim, K., 2010, “Safety Evaluation Method of Ship Berthing at Pontoon under Strong Current from Viewpoint of Ship Motions”, *Proceedings of the 20th International Offshore and Polar Engineering Conference (ISOPE 2010)*, Beijing, China, 956-963
- [32] Skejic, R. and Berg, T.E., 2010, “Combined Seakeeping and Maneuvering Analysis of a Two-Ship Lightering Operations”, *Proceedings of 29th International Conference on Offshore Mechanics and Arctic Engineering*, Shanghai, China, OMAE2010-20616
- [33] Teigen, P., Niedzwecki, J.M., 2006, “A Computational Study of Wave Effects Related to Side-by-Side LNG Offloading”, *Proceedings of the 16th International Offshore and Polar Engineering Conference (ISOPE 2006)*, San Francisco, California, 238-247
- [34] Teresa, A.G., 2008, “Experimental study on the hydrodynamic forces

- induced by a twin-propeller ferry during berthing”, *Ocean Engineering*, 32, 323-332
- [35] Turnbull, M.S., Borthwick, A.G.L., Taylor, R.E., 2003, “Wave-structure interaction using coupled structured-unstructured finite element meshes”, *Applied Ocean Research*, 25, 63-77
- [36] Wilde, J.J., Dijk, A.W., Berg, J., Dekker, J., 2009, “Direct Time Domain Downtime Assessment for LNG Operations using Computer Cluster”, *Proceedings of the 19th International Offshore and Polar Engineering Conference (ISOPE 2009)*, Osaka, Japan, 127-135
- [37] Yang, S., Ma, Q.W., 2007, “Numerical simulation of fully nonlinear interaction between steep waves and 2D floating bodies using the QALE-FEM method”, *Journal of Computational Physics*, 221, 666-692
- [38] Ye, W., Luo, Y., Pollack, J., 2005, “LNG Floating Regasification Unit (FRU) Side-by-side Mooring Analysis”, *Proceedings of 24th International Conference on Offshore Mechanics and Arctic Engineering (OMAE 2005)*, Halkidiki, Greece, 1-10
- [39] Yoo, W.J., 2000, “An Experimental Research on the Maneuvering Derivatives of a Twin-Screw Ferry for Berthing and Unberthing”, Ph.D thesis, Seoul National University

초 록

본 논문에서는 해상에서 이루어지는 두 부유체 간 접안 문제를 다루기 위한 새로운 수치해석기법을 개발하고, 이를 적용하여 접안과정에서 발생하는 파랑 중 운동 및 파랑력 특성에 관한 수치해석 연구를 진행하였다.

해상 접안 문제에서는 하나의 구조물에 시간에 따라 서서히 접근해가는 부유체가 존재하기 때문에, 계산이 되는 유체영역이 시간에 따라 계속적으로 변화하는 특징을 가지고 있다. 부유체 거동 측면에서는 과도 대변위 수평면 운동을 포함한 천이 문제에 해당한다. 이는 기존의 주파수영역에 근간한 부유체 해석 방법이나 물체고정좌표계에서 유체영역 경계가 변하지 않는 기존의 유동해석 방법이 적용될 수 없음을 의미한다. 따라서 본 연구에서는 유한요소법과 새로운 재격자 알고리즘이 결합된 접안문제에 대한 효율적인 수치해석 방법을 제안하였다. 유한요소법은 시간영역에서 매시간 새로운 계산영역에서 라플라스 방정식을 효율적으로 풀기 위하여 도입되었으며, 선형 자유표면 경계조건은 4차의 Adams-Bashforth-Moulton 방법으로 시적분하여 자유표면에서의 속도 포텐셜과 파고정보를 구하였다. 매시간 두 부유체의 상대위치에 따라 재격자 과정이 진행되는데, 이때 재격자를 효율적으로 진행하기 위하여 국소 격자계와 직교 유동 격자계를 도입하여 두 격자계의 틈새만을 매시간 연결하는 알고리즘을 도입하여 빠르고 강건하게 재격자 과정을 진행하도록 하였다.

개발된 수치해석 방법을 이용하여 파랑 중 두 바지선의 접안과정에서의 동유체력 특성에 대해 연구하였다. 이 때 접안속도는 일정하다고 가정하였으며, 직선의 접안경로를 고려하였다. 동일한 두 바지선에 대해 다양한 파주기 조건과 파향에서의 접안 시뮬레이션을 수행하고, 그 때 발생하는 파랑력 특성에 대해 논의하였다. 특히 선수파 조건에서는 특정 주파수에서 발생하는 틸새 공진에 대해 자세히 고찰하였다. 선수사파와 횡파조건에서는 입사파 방향에 위치한 구조물에 의한 차폐효과에 대해 논하였으며, 접안과정에서 발생하는 강한 진폭변조 특성에 대해 살펴보았다. 현 수치해석 기법의 결과는 모형시험 시계열과 직접 비교를 통하여 검증이 수행되었다. 추가적인 연구로 운송 바지선의 크기가 변화하였을 때, 접안과정 중 동유체력 특성에 대해 살펴보았다.

두 번째 적용 문제로 파랑 중 FPSO와 Shuttle tanker의 접안문제에 대해 살펴보았다. 이 경우에는 접안과정에서의 두 부유체의 파랑 운동 특성에 대해 집중적으로 검토하였다. 먼저 선수 규칙파 조건에서의 파랑 중 운동 특성을 살펴보았으며, 두 부유체 사이의 틸새 공진에 의한 횡동요 가진 특성을 관찰하였다. 다음으로 선수사파 및 횡파 조건에서의 파랑 중 운동 특성에 대해 비교 분석하였다. 이 경우 두 부유체의 상호간섭효과에 의해 차폐효과 및 진폭변조 특성이 파랑 운동에 잘 드러났다. 마지막으로 불규칙파 중 접안 시 거동특성에 대해 검토하였다. 이 경우 파주기, 파고에 따른 불규칙 파 접안 시뮬레이션이 이루어졌으며, 최대 운동응답을 기준으로 그 경향을 검토하였다.

주요어: 접안, 부유체, 동유체력, 과량 운동, 유한요소법
학 번: 2006-30808